Fuel-vortex interactions for enhanced mixing in supersonic flow — **Source link** ↗

R. Fuller, P.-K. Wu, A. Nejad, Joseph A. Schetz

Institutions: Virginia Tech

Related papers:

- Experimental investigation of a supersonic swept ramp injector using laser-induced iodine fluorescence

- Mixing of Transverse Jets and Wall Jets in Supersonic Flow

- Vortex generation and mixing in three-dimensional supersonic combustors

- A numerical study on mixing of supersonic flow field with parallel injection through ramp nozzle

- Vortex enhancement of jet penetration in supersonic flow.

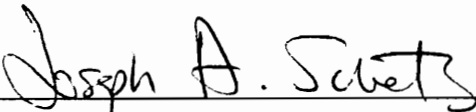# FUEL-VORTEX INTERACTIONS FOR ENHANCED MIXING IN SUPERSONIC FLOW
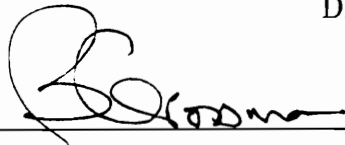
by

Raymond Preston Fuller

Dissertation Submitted to the Faculty of the

Virginia Polytechnic Institute and State University

in partial fulfillment of the requirements for the degree of

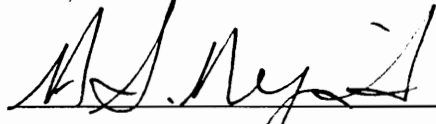DOCTOR OF PHILOSOPHY

IN

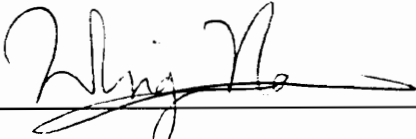AEROSPACE ENGINEERING

APPROVED:

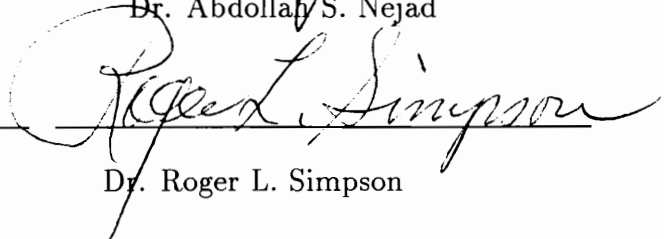Dr. Joseph A. Schetz, Chairman

Dr. Bernard Grossman

Dr. Abdollah S. Nejad

Dr. Wing F. Ng

Dr. Roger L. Simpson

August, 1996

Blacksburg, Virginia

Key Words: Mixing, Supersonic, Injection, Vortex, Aerodynamic, Ramp

FUEL-VORTEX INTERACTIONS FOR ENHANCED MIXING IN SUPERSONIC FLOW

by

Raymond P. Fuller

Joseph A. Schetz, Chairman

Aerospace and Ocean Engineering

(ABSTRACT)

An experimental investigation was conducted to compare the supersonic mixing performance between a novel aerodynamic ramp injector and a physical ramp injector. The aerodynamic ramp injector consisted of nine, flush-wall jets arranged to produce multiplicative fuel-vortex interactions for mixing enhancement in a supersonic main flow. The physical ramp injector was a previously optimized and tested swept-ramp design. Test conditions included a Mach 2.0 freestream of air with a Reynolds number of 3.63×10^7 per meter and helium injection with jet-to-freestream momentum flux ratios of 1.0 and 2.0. Planar-laser Rayleigh scattering and conventional probing techniques including species composition sampling were employed to interrogate the flow field at several downstream locations. Results show that with increasing jet momentum, the aero-ramp exhibited a significant increase in penetration while the physical ramp showed no discernible change. The near-field mixing of the aero-ramp was superior to that of the physical ramp. At the higher jet momentum, the far-field mixing of the aero-ramp was comparable to the physical ramp. In all cases, the total pressure losses suffered with the aero-ramp were less than those incurred with the physical ramp. For both injectors, the total pressure losses decreased with increasing jet momentum. Finally, an analytical relationship predicting the Rayleigh scattering intensity as a function of helium concentration, pressure, and temperature was derived and experimentally validated. It is concluded that these results merit further studies and parametric optimization of the aero-ramp or similar configurations. It is also concluded that further studies may be conducted to establish the absolute quantitative nature of the Rayleigh scattering technique.

Acknowledgments

I would first like to thank my advisor, Dr. Joseph Schetz, for his knowledgeable instruction, careful guidance, and encouraging support throughout my studies at Virginia Tech and Wright Laboratory. I would also like to thank my committee member Dr. Abdollah Nejad for his financial support, facility provisions, consultation, and encouragement throughout my studies at Wright Laboratory. With no less appreciation, I would like to thank my supervisor Dr. Tzong Chen for providing me a research position with Taitech, Inc. through which my financial support was channeled. Finally, I would like to thank Dr. Bernard Grossman, Dr. Wing Ng, and Dr. Roger Simpson for serving as members on my graduate advisory committee.

Throughout my studies, many others have helped me along the way. Dr. Pei-Kuan Wu of Taitech, Inc. provided considerable input, guidance, and assistance in this research and I owe him many thanks. Without the efforts of our instrumentation expert, Mr. Dave Schommer, this work could not have been performed. A very special thanks goes out to Drs. Mark Gruber and Diana Glawe of Wright Laboratory who laid the foundation for the imaging technique and provided me with much help and technical assistance. I want to thank Mr. Gary Haines of Taitech for handling much of the mechanical design work. I would also like to thank Mr. Jeffrey Donbar of Wright Laboratory who provided technical monitoring, assistance, and advice. I would like to thank Mr. Kevin Kirkendall of Taitech who frequently provided me with help and advice. I would like to express special gratitude to Dr. Ken Chadwick of Calspan who played an instrumental role in my initial studies at Virginia Tech. I would also like to thank Mr. Charles Smith of Innovative Scientific Solutions, Inc. for the many things he taught me in his days with Taitech. Finally, I would like to thank the technicians, Mr. Greg Dudding, Mr. Kent Morris, Mr. Frank Shelor, Mr. Gary Stafford, and Mr. Bruce Stanger, who helped me greatly with my work at Virginia Tech.

Finally, I owe my deepest and most sincere gratitude to my dear wife, who endured many personal sacrifices in support of these studies. It was her constant love and support which encouraged me through the long and arduous process of completing this work. Therefore, I dedicate this dissertation to my wife, Thia Ly Fuller.

Table of Contents

Nomenclature

a	= gas analyzer calibration constant
A	= cross-sectional area
$\bar{A}$	= relative plume area
A_u	= area of perfectly unmixed (segregated) plume
A_s	= area of uniformly stoichiometric fuel plume
α	= mass fraction
α_{max}	= maximum helium mass fraction
α_s	= H_2-air stoichiometric mass fraction, 0.0292
β	= general coefficient of proportionality
b	= gas analyzer calibration constant
c	= sound speed
C^*	= critical flow function
c_d	= injector discharge coefficient
d	= hot-film diameter
d_{eff}	= effective jet diameter
d_{eq}	= equivalent jet diameter
d_j	= jet diameter
d_p	= scattering particle diameter
δ_x	= boundary layer displacement thickness
δ_ω	= shear layer vorticity thickness
Δ_Ω	= solid angle
E	= radiant flux at a surface
E_s	= Rayleigh scattering irradiance
ϵ	= efficiency of collection optics
$\mathbf{F}$	= matrix of pixel values
γ	= ratio of specific heats
h	= plume penetration height

η_m	= mixing efficiency
I	= pixel intensity
$\bar{I}$	= mean pixel intensity
I_f	= hot-film current
I_s	= light scattering intensity
k	= thermal conductivity or Boltzmann constant
Kn	= Knudsen number
l	= active length of hot-film sensor
λ	= jet-to-freestream mass flux ratio, $(\rho u)_j/(\rho u)_\infty$
λ_i	= incident light wavelength
$\dot{m}$	= mass flow rate
M	= Mach number
$\mathcal{M}$	= molecular weight
μ	= viscosity
n	= decay rate of α_{max}
$\mathcal{N}$	= number of moles
$\hat{N}$	= Avagadro's number
N_p	= particle number density
Nu	= Nusselt number
η_m	= mixing efficiency
P	= static pressure
P_c	= cone-static pressure
P_{eb}	= effective back pressure
P_t	= total pressure
$P_{t,2}$	= Pitot pressure
Π	= total pressure loss parameter
$\bar{q}$	= jet-to-freestream momentum flux ratio, $(\rho u^2)_j/(\rho u^2)_\infty$
q_f	= hot-film heat transfer rate
R	= Specific gas constant
R_f	= hot-film resistance
$\hat{R}$	= universal gas constant

Re	=	Reynolds number
r_p	=	scattering particle radius
R_s	=	anemometer bridge series resistance
ρ	=	static density
ρ_p	=	particle density
Sc	=	Schmidt number
St	=	Stokes number
σ	=	standard deviation
σ_p	=	scattering cross-section
T	=	static temperature
T_t	=	total temperature
τ_f	=	fluid dynamic time scale
τ_p	=	particle time scale
u	=	flow speed
U_s	=	spatial unmixedness
V	=	volume or hot-film voltage
$\mathbf{W}$	=	convolution kernel
x	=	streamwise coordinate
x_{fm}	=	fully-mixed distance
X_{He}	=	helium mole fraction
y	=	spanwise coordinate
z	=	vertical coordinate

Subscripts

∞	=	freestream property
air	=	air property
He	=	helium property
j	=	jet exit property

List of Tables

List of Figures

1
Introduction

The role of supersonic injection and mixing enhancement is vital to the development of a successful hypersonic air-breathing propulsion system. A successful system will be one capable of providing the thrust required to accelerate an aero-space plane or missile from supersonic to hypersonic speeds within the earth's atmosphere. For flight Mach numbers above 5, the adverse effects associated with decelerating the flow to subsonic speeds for combustion prohibit the use of conventional ramjets.[1] Consequently, the use of supersonic combustion ramjets (scramjets) has been proposed as a necessary alternative. Scramjet combustor velocities can be on the order of several thousand meters per second, resulting in severely restricted fuel residence times. It is a primary concern in hypersonic vehicle development to limit the engine length and therefore the combustor length to a reasonable size. This requires an effective injection scheme producing enhanced mixing and rapid combustion. A typical scramjet design configuration may include a pilot flame combustor system with hydrogen as the injected fuel. While hydrogen can provide the necessary heat release to produce sufficient thrust levels, its low molecular weight inhibits penetration and rapid dispersion. Injection and mixing augmentation schemes have been developed to effectively inject and disperse the fuel for efficient mixing and combustion. However, there usually exists a trade-off between rapid mixing and total pressure recovery. Hence, the goal here is to develop an injection and mixing augmentation scheme capable of providing rapid mixing, stable combustion and minimized pressure losses.

The subject of transverse injection of a foreign gas into a supersonic main flow has been studied extensively in the past. A comprehensive review of the mixing of transverse jets and wall jets in supersonic flow including a substantial list of references to earlier work has been presented by Schetz et al.[2] The flowfield of of an underexpanded transverse jet in a supersonic stream is depicted in Figure

1.1. A study of the penetration of gaseous jets injected into a supersonic stream was conducted by Schetz et al.[3] From this study, a model for the penetration trajectory of an underexpanded jet was developed. Furthermore, the *effective back pressure* analogy between the cross-flow case and that of underexpanded injection into a quiescent medium was presented. In subsequent studies conducted by Schetz et al.,[4,5] the adequacy of this analogy was verified by correlating the height of the first Mach disk and the penetration trajectory with the ratio of jet pressure to effective back pressure. For normal injection, the effective back pressure was determined to be 0.8 times the static pressure behind a normal shock in the freestream. Schetz[6] later performed an analysis based on an equivalent solid-body concept to describe the interaction shock shape for transverse injection in supersonic flow. The analysis was substantiated by comparison with experiment over a wide range of conditions. Most recently, Barber et al.,[7] have investigated normal injection through a wedge-shaped orifice into a supersonic flow. This orifice had a sharp leading edge with a rounded semicircular base. This geometry was found to provide much better penetration with slightly better mixing characteristics when compared to injection from a circular orifice.

Many variations of simple transverse injection have also been studied. Mays et al.[8] studied the effects of low-angle injection into a supersonic flow. It was shown that as the injection angle decreases the near-field mixing also decreases. However, this decrease in mixing is accompanied by a desirable reduction in pressure losses. In the far field, injection angle was found to have little effect on the overall mixing. Fuller et al.[9] extended this work to include injector yaw as well as low transverse angles. It was observed that while injector yaw did not increase the rate of decay of maximum concentration, it did cause an increase in the overall injectant plume cross section, thus increasing the size of the mixing region. In both studies, it was shown that a matched pressure injection produced greater fuel concentration decay rates when compared to an underexpanded case.

It has been previously postulated and shown that mixing enhancement may be achieved through the addition of three-dimensional vorticity. Based on experiments performed in the subsonic and transonic regimes, Swithenbank et al.[10] proposed that substantial increases in mixing rates might

be obtained by introducing a swirling motion to the fuel. It was postulated that the increase in fuel-air mixing rates resulted from the creation of radial and axial pressure gradients in the swirling flow. Povinelli et al.[11] investigated the penetration and spreading of helium injected into the vortex pattern generated by a delta wing in a Mach 2 airstream. Results were compared to a flat-plate injector with the same projected frontal area and angle of attack. It was concluded that the vortex motion generated by the delta wing injector led to substantial increases in the penetration and spreading rates in supersonic flow. In a subsequent study, Hersh et al.[12] obtained similar results for fuel injected into a counter-rotating vortex structure also generated by delta wings. While these studies demonstrated the effects on penetration and spreading, no experimental data confirming accelerated mixing rates due to swirl in a supersonic stream had been produced. In fact, studies conducted by Povinelli et al.[13] and Schetz et al.[14] concluded that for co-axial jets in supersonic flow, jets with swirl produced no discernible effect on the mixing when compared to non-swirling jets. However, it is suspected that the tangential velocities employed in those studies were too small to create radial and axial pressure gradients sufficient for mixing enhancement. The experimental investigation of Tillman et al.[15] concluded that the axial vortex mechanism previously shown to be responsible for rapid mixing in low-speed, subsonic flows is indeed effective in the supersonic jet environment. Naughton et al.[16] conducted an experimental study of the effect of streamwise vorticity on supersonic turbulent mixing. A Mach 3 streamwise vortex was generated using a strut-mounted swirl injector exhausting into a Mach 3.5 freestream. Results were compared with a baseline, swirl-free jet. It was found that with the addition of streamwise vorticity, increases in mixing rates of up to 34% are possible.

Much interest has recently been given to mechanisms leading to enhanced mixing through the interaction of shock waves with fuel-vortex structures. Marble et al.[17] first proposed the mechanism of shock-induced vorticity generation for supersonic combustion. It was argued that the interaction of a shock wave with a jet of light gas surrounded by an ambient heavy gas would generate vorticity around the perimeter of the jet. This vorticity is caused by the *baroclinic torque* which is essentially

a misalignment of the pressure and density gradients at a point in the flow. That is, vorticity will be created in the flow at any point where a pressure gradient interacts with a non-parallel density gradient. This process is governed by the vorticity equation shown here.

$$\rho \frac{D}{Dt}\left(\frac{\vec{\omega}}{\rho}\right) = \frac{1}{\rho^2}\vec{\nabla}\rho \times \vec{\nabla}p \qquad [1.1]$$

An excellent review of this process was given by Waitz et al.,[18] and a detailed model has been presented by Yang et al.[19] Marble et al.[20] later showed that this phenomena can indeed lead to a considerable enhancement of the mixing process. Marble also concluded that some mechanism for destabilizing the vortex must be incorporated into the injector design to ensure complete mixing of the light gas with air. This agrees with the proposal of Naughton et al.,[16] that a streamwise vortex can enhance supersonic mixing if the vortical flow is passed through a shock wave of sufficient strength to cause vortex breakdown. Metwally et al.[21] showed that a strong shock/vortex interaction leading to vortex breakdown is characterized by unsteady upstream shock propagation, apparent flow recirculation, and the appearance of a recompression shock downstream. It was reasoned that such behavior should lead to increased turbulence levels downstream and therefore enhanced fuel-air mixing.[16]

Numerous investigations[22-27] have looked at wall ramp injectors (similar to that shown in Figure 3.6) as a viable means of providing enhanced fuel-air mixing. Ramp designs attempt to make full use of the various mixing enhancement mechanisms previously discussed. The ramp should provide vortex shedding off the edges and a local separation at the base. The fuel is injected through the base and into the counter-rotating vortex pattern. This situation creates a very dynamic mixing distribution. Furthermore, the ramp shock will reflect off the opposite wall and impinge on the plume/vortex structure resulting in possible vortex breakdown and further enhancement of the mixing. The reflected shock should also create a baroclinic torque where it intersects with the plume resulting in additional vorticity. Finally, the recirculation zone occurring due to flow separation at the base of the ramp should provide flameholding similar to a rearward-facing step. The major drawback

to this design is its dependency on maintaining pristine geometry in the extremely harsh environment of a high-enthalpy, scramjet combustor. Its physically intrusive nature will necessarily create *hot spots* with temperatures exceeding the thermal limits of most practical materials. Furthermore, the added drag and loss of thrust potential resulting from its intrusive presence may be unacceptable in certain engine design configurations.

The results of the previously described studies form the database of knowledge which was applied in the development of the novel injector design given the term *aerodynamic ramp* or simply *aero-ramp*. The aero-ramp shown in Figure 1.2, based on a concept developed by Prof. J. Schetz, was first formally presented by Cox et al.[28] after a preliminary investigation involving both experiments and CFD. This injector design consisted of a three-by-three array of closely spaced, flush-wall jets with various transverse and yaw angles. The jets were geometrically arranged so as to generate multiplicative fuel-vortex interactions which should lead to enhanced mixing. These fuel-vortex interactions were to include skew induced vortex generation, shock induced vortex generation, and vortex breakdown, all of which have been shown to be effective mixing enhancement mechanisms. Furthermore the flush-wall design coupled with low angle injection avoids the excessive pressure losses, drag, and hot-spots associated with conventional vortex generators.

The primary objective of the present investigation was to assess the performance of the aerodynamic ramp by comparing it to a proven mixer of similar scale. Identical experiments were performed on both the aero-ramp and a physical swept ramp using the same facilities. Diagnostics included shadowgraph photography, planar-laser Rayleigh imaging, gas sampling, and conventional probing. This dissertation documents the results of those experiments and presents a thorough analysis of the data. The flow fields generated by each injector are analyzed in detail. An array of performance indices are computed to quantify the mixing characteristics of each injector. Several new figures of merit, including a method for the quantification of total pressure losses, are presented.

A secondary objective of this investigation was to establish the quantitative nature of a planar-laser Rayleigh imaging technique. This is done by first deriving a relationship to predict the Rayleigh

scattering intensity for a known injectant concentration, pressure and temperature. Next, this relationship is reduced to a function of the injectant concentration and a single state variable – density. Finally, the Rayleigh scattering data is combined with the gas sampling and probing data to validate this relationship.
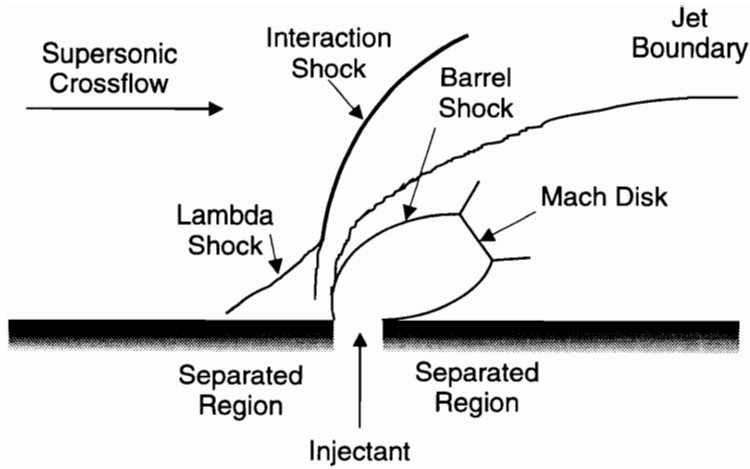
Figure 1.1 Underexpanded transverse jet in a supersonic stream.
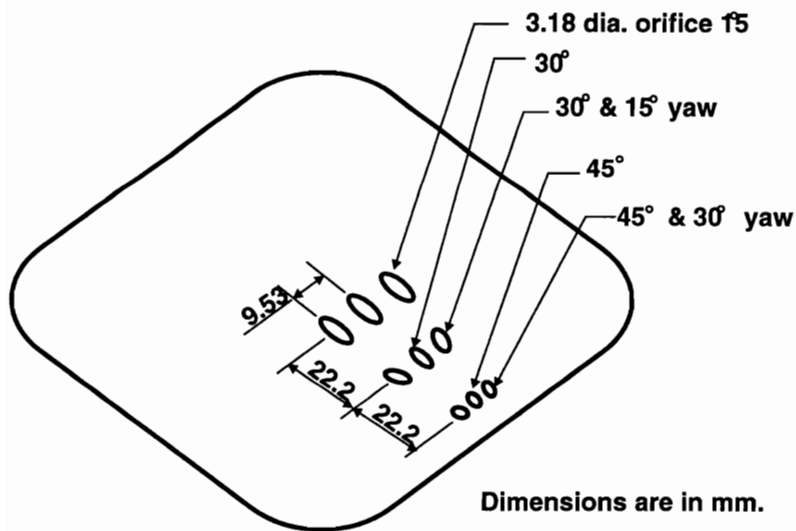
Figure 1.2 Aerodynamic ramp model.

Tests were conducted with a Mach 2.0 main flow of air. Freestream conditions were set for a total pressure of 310 kPa and total temperature of 300 K, producing a freestream Reynolds number of 3.63×10^7 per meter which lead to a turbulent boundary layer at the injection station. Table 2.1 summarizes the freestream flow conditions.

Table 2.1 Summary of freestream flow conditions.

$\mathbf{M}_\infty$	1.98	—
$\mathbf{P}_{t,\infty}$	310	kPa
$\mathbf{T}_{t,\infty}$	300	K
$\mathbf{P}_\infty$	39.6	kPa
$\mathbf{T}_\infty$	167	K
c_∞	259	m/sec
$\mathbf{U}_\infty$	513	m/sec
ρ_∞	0.826	kg/m^3
γ_∞	1.4	—
$\dot{m}_\infty$	8.2	kg/sec

Pure helium was used as the injectant to simulate hydrogen fuel. The complexity of the injection schemes made the prediction of the *effective back pressure*, P_{eb}, prohibitively difficult. Therefore, rather than choosing underexpansion ratios, P_j/P_{eb}, to characterize the flow conditions, the jet-to-freestream momentum flux ratio was utilized. The jet-to-freestream momentum flux ratio, $\bar{q}$, is defined by

$$\bar{q} = \frac{(\rho u^2)_j}{(\rho u^2)_\infty} = \frac{(\gamma p M^2)_j}{(\gamma p M^2)_\infty}. \qquad [2.1]$$

Many important phenomena associated with injection and mixing in a turbulent flow are found to correlate well with $\bar{q}$. For these experiments, the injectant total pressure was adjusted so that $\bar{q}$ was set at either 1.0 or 2.0. While the aero-ramp was designed for a jet-to-freestream momentum

flux ratio of $\bar{q} = 2.0$ or higher, most of the testing was conducted at $\bar{q} = 1.0$ to conserve on helium costs. Neglecting injector discharge coefficients for the moment, these settings corresponded to an injection total pressure of 273 kPa for $\bar{q} = 1.0$ and 546 kPa for $\bar{q} = 2.0$. In all cases, the injectant total temperature was an ambient condition and averaged approximately 294 K. Table 2.2 shows a summary of the jet exit conditions, and Table 2.3 shows a summary of dimensionless test parameters.

Table 2.2 Summary of jet exit conditions.

	$\bar{q} = 1.0$	$\bar{q} = 2.0$	
M_j	1.0	1.0	—
$P_{t,j}$	273	546	kPa
$T_{t,j}$	294	294	K
P_j	144	288	kPa
T_j	245	245	K
c_j	922	922	m/sec
u_j	922	922	m/sec
ρ_j	0.283	0.566	kg/m^3
γ_j	1.67	1.67	—
$\dot{m}_j$	0.019	0.038	kg/sec

Table 2.3 Summary of dimensionless parameters.

	$\bar{q} = 1.0$	$\bar{q} = 2.0$
P_j/P_∞	3.64	7.27
ρ_j/ρ_∞	0.34	0.69
T_j/T_∞	1.47	1.47
u_j/u_∞	1.80	1.80
λ	0.61	1.24

A right-handed, Cartesian coordinate system was chosen with the origin placed at the leading edge of the injector on the wall surface along the test section centerline. The positive x-axis was in the freestream direction, the positive z-axis was in the vertical direction perpendicular to the wall surface, and the y-axis spanned the test section. For the physical ramp injector, measurements were taken at axial distances of 8, 12, 21, 52, and 70 cm. For the aero-ramp injector, measurements were taken at axial distances of 7, 10, 20, 50, and 67 cm. A schematic of the test section coordinate system with the physical ramp installed is shown in Figure 2.1. At each axial location, a point grid across

the flow was established for the gas sampling and probing measurements. The measurement grid had a spatial resolution of 0.25 cm and ranges of $-2.8 \leq y \leq 2.8$ cm and $0.0 \leq z \leq 7.6$ cm yielding a total of 713 measurements in a 23×30 array. The Rayleigh scattering measurements obtained with a CCD camera had a spatial resolution of approximately 0.009 cm and ranges of $-2.6 \leq y \leq 2.6$ cm and $0.0 \leq z \leq 3.5$ cm yielding a total of 221,952 measurements in a 578×384 array.

1 - 8 cm
2 - 12 cm
3 - 21 cm
4 - 52 cm
5 - 70 cm
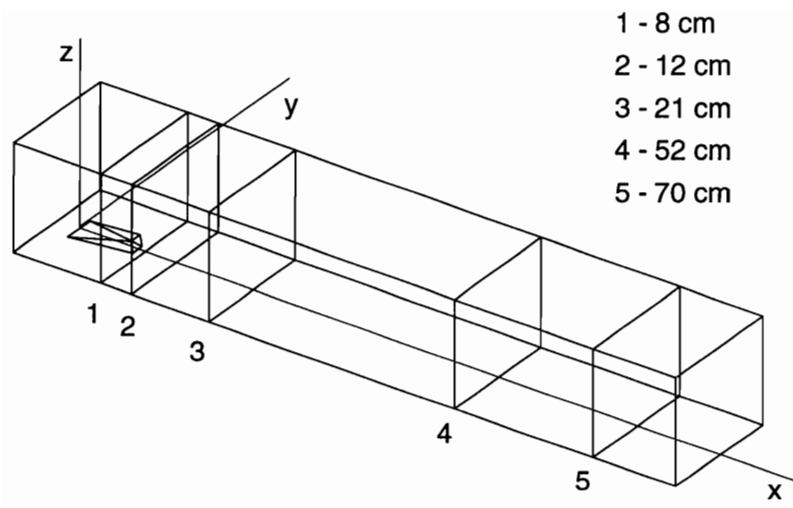
Figure 2.1 Test section coordinate system with physical ramp.

Test Facilities and Models

3.1 The Wind Tunnel

All experiments were conducted in the Supersonic Combustion Facility of the Wright Laboratory Aero Propulsion and Power Directorate located at Wright-Patterson Air Force Base, Ohio shown in Figures 3.1 and 3.2. The facility is an open-loop supersonic wind tunnel capable of containing high-speed combustion. Air was supplied to the facility through various turbine and reciprocating compressors capable of providing mass flow rates up to 15 kg/sec at 5.2 MPa. A gas-fired heat exchanger was available for heating the inlet flow to 920 K. A massive exhaust system was used to lower and maintain the back pressure for smooth starting and safe operation. The wind tunnel consists of five major components, including the inlet section, the settling chamber, the nozzle section, the test section, and the diffuser. The following descriptions were taken from Gruber and Nejad[29], chief engineers and designers of the facility.

3.1.1 Inlet Section

The inlet section transports the air from the main supply manifold. Four pieces make up this section, including the upper manifold, the lower manifold, the block valve, and the expansion section. Six stainless steel flexible hoses connect the upper and lower manifolds and allow for thermal growth in the upstream direction. The lower manifold, block valve, and expansion section mount onto support carts that roll on a pair of rails, which are anchored to the bed plate of the test cell. These carts allow for roll-away maintenance and additional thermal growth management. The 15.2-cm Masoneilan block valve prevents flow from entering the test section during system idle. Closing this valve and opening the vent valve allows a specific set of run conditions to be maintained while

the test section hardware modifications are made. A seed injection port found just downstream of the block valve provides a convenient location for the addition of seed media for laser diagnostics such as Rayleigh/Mie scattering. This port can be fitted with numerous injection components to ensure a wide variety of potential seed types. Also, since injection occurs upstream of the settling chamber, the entire freestream flow may be seeded uniformly. Finally, the expansion section houses a rearward-facing perforated cone to provide a means of evenly distributing the flow as it exits the block valve and enters the 61-cm settling chamber.

3.1.2   Settling Chamber

The settling chamber conditions the air using an array of three mesh screens, one coarse and two fine, and a 7.6-cm long section of honeycomb to break up large-scale turbulence and straighten the flow before acceleration by the supersonic nozzle. This chamber can withstand pressures up to 2.9 MPa at temperatures of 920 K. Additionally, the settling chamber size produces air velocities of approximately 14 m/sec over the range of desired operating conditions for the combustion tunnel. Pressure and temperature sensors installed in the chamber provide feedback to the control system and documentation for the duration of the tunnel run. The entire chamber mounts to a support stand (fixed at the downstream end, rolling at the upstream end) which supports its weight and the force experienced due to the subatmospheric pressure of the exhauster system. This stand also anchors to the bed plate of the test cell.

Due to the change in geometry from the axisymmetric settling chamber to the planar nozzle section, a transition region between the two is required to prevent vortex shedding from the sharp corners that would exist without one. This transition take place using four precision machined pieces, each made from one-quarter of a 15.2-cm diameter stainless steel rod. When assembled, these pieces form a section 7.6 cm deep with outer edge dimensions of roughly 30 cm square and inner edge dimensions of roughly 15 cm square. The assembly then fastens inside the flange that separates the nozzle from the settling chamber to provide the desired contours.

3.1.3 Nozzle and Test Sections

A planar two-dimensional nozzle was designed, using a method of characteristics code developed by Carrol, et al.[30], to produce the desired expansion to a Mach number of 2.0 at the entrance to the test section. The code computed the contour of a continuous slope, converging-diverging nozzle yielding a uniform exit flow aligned with the nozzle axis. Boundary layer growth was not accounted for in the inviscid nozzle code. Corrections for viscous effects were accomplished using the boundary layer displacement thickness calculations resulting from Burkes equation[31], which relates the local turbulent boundary layer displacement thickness to the local Mach and Reynolds number as follows:

$$\frac{\delta_x^*}{x} = 0.0463 \frac{M_x^{1.311}}{Re_x^{0.276}} \qquad [3.1]$$

This correction procedure assumes that the displacement thickness is zero at the nozzle throat and is a linear function of the streamwise coordinate, x. Such a procedure introduces negligible errors into the correction.[32] Applying the entire viscous correction to the upper and lower contoured walls of the nozzle preserves the parallel nature of the sidewalls and makes the final nozzle exit dimensions 13.2 cm high by 15.2 cm wide. Upstream of the nozzle throat is a contraction that provides a smooth transition between the exit of the nozzle flange discussed above and the throat. The sidewalls of the nozzle section are instrumented with a row of pressure taps on the transverse centerline that permits documentation of the centerline wall pressure distribution from the entrance of the nozzle through the throat and to the exit.

The constant area test section, shown in Fig. 3.3, provides a large degree of optical access so that a wide variety of nonintrusive diagnostics may be used to examine the flow. A pair of fused silica windows mounted in the side walls and a single fused silica window mounted in the top wall provide the necessary access. The side windows allow direct viewing of the entire vertical dimension of the test section and approximately 44.5 cm of the streamwise dimension. The top window provides the same optical access length in the streamwise dimension with 7.6 cm across the spanwise dimension. Because each window has two possible locations, i.e., one upstream and one downstream, a total

viewing length of 79 cm results in the streamwise dimension. A fourth fused silica window, mounted in the diffuser section of the facility, yields direct optical access to the plane perpendicular to the flow direction and allows for visualizing the entire span of the tunnel from the entire downstream direction.

An array of test inserts mounted in the bottom wall of the test section allows for a variety of injection configurations to be incorporated into the same hardware without the need for significant modifications. Both the physical ramp and aero-ramp injectors were designed to fit within the insert geometry. In later sections, these injector inserts will be described in full detail.

A special piping system was constructed to supply the injectors with the desired gas. Tube trailers containing large volumes of high-pressure (15 MPa) air or helium were available outside the test cell. A high-pressure regulator fed a 5-cm supply line with gas from the trailer. This line led to a manifold in the test cell, where a 2.5-cm line provided gas to the injector. A dome regulator placed in this line controlled the injectant pressure. A small amount of gas from the supply line loaded the regulator dome allowing very repeatable pressure conditions to be set at the jet exit. A pair of solenoid valves placed between the dome supply line and the regulator dome itself conserved the injectant gas and allowed rapid loading and unloading. A full-port, shut-off valve was placed upstream of the low pressure regulator, and a master solenoid was installed just upstream of the injector exit to allow fast on-off capability once appropriate supply conditions were set. A pressure transducer and thermocouple were installed to monitor and record jet stagnation conditions.

3.1.4 Diffuser

The final component of the supersonic research facility is the diffuser. This device connects the exit of the test section to the exhaust line of the facility. The simple dump diffuser was designed to slow and cool the air flow to appropriate velocities and temperatures required by the air coolers of the facility. Water spray injection cools the flow as required. In addition to its role in deceleration and cooling the flow, the diffuser houses the end-viewing port that allows visual investigation of

the test section cross-sectional plane. The diffuser hangs from an A-frame support allowing a large unobstructed area beneath the test section for placement of necessary optical diagnostic equipment.

3.1.5 Control System

The entire facility is controlled by a Johnson-Yokogawa μXL distributed control system. This system continually monitors and maintains the stagnation conditions in the settling chamber at user specified values. The system is composed of 16 analog and 32 digital I/O lines with internal feedback control routines. The system controls the flow conditions by regulating the inflow from the supply lines and the outflow through the bleed line. When the tunnel valve is closed, 100% of the flow is diverted through the bleed line. When the tunnel valve is open, the stagnation conditions are set by adjusting the bleed valve. Once the conditions are met, the system can maintain the stagnation pressure and temperature within 1% of their nominal values.

3.1.6 Probe Actuator System

The probe actuator system was an L.C. Smith Ball Bearing Rod (BBR) actuator. The BBR actuator is designed for high vibration environments requiring small probe lengths. It has a range of 25.4 cm and can drive a load of 356 N at 25.4 cm/min. The probe is mounted to a platform that traverses along three hardened rods by means of ball bushings. The platform is driven by a bearing screw and D.C. motor assembly providing potentiometer feedback. The entire assembly is attached to the end of the probe insertion and sealing system shown in Figure 3.4. The weight of the system is roughly 6.8 kg. A photograph of the assembly mounted to the tunnel test section is shown in Figure 3.5.

The system is controlled by an L.C. Smith traverse prepositioner control. This system allows the user manual control of the probe position as well as automatic positioning. Up to 24 preset location may be defined. Finally, the system is interfaced to the data acquisition and control PC via an RS-232 serial communications line. This allow for sequencing of data acquisition and probe movements.

3.1.7 Data Acquisition System

All data acquisition, except for the gas sampling, was performed using a Data Translation 2831 analog and digital I/O board in an Intel 80486-based PC. The DT2831 provides up to 16 channels of A/D conversion with 12-bit resolution. It has 2 channels of analog output with independent D/A converters providing 12-bit resolution. There are 8 lines available for digital I/O. The DT2831 provides an Am9513A System Timing Controller which has three counter/timers to automatically initiate A/D, D/A, or simultaneous A/D and D/A conversions, and two counter/timers for external uses such as event counting and frequency measurement. Furthermore, all settings, such as input gain, range, DIO direction, etc., are software configurable.

3.2 Physical Ramp Injector

The physical ramp injector was based on the design concept first introduced by Northam et al.[22] in their supersonic combustion studies. A schematic and photograph of the injector insert are shown in Figures 3.6 and 3.7, respectively. The swept ramp fuel injector was designed to produce quasi-streamwise vortex shedding and local separation (similar to a rearward facing step) that should lead to enhanced mixing. In the present studies, the swept ramp injector (see attached figure) has a 10.3° compression surface with a leading-edge width of 4.03-cm, a trailing-edge width of 1.524-cm, and a length of 6.10-cm. The ramp base is canted at 10.3° and contains the 0.953-cm sonic injection orifice such that the injection axis is parallel to the ramp compression surface.

The objective of this design is to produce a pressure difference between the freestream fluid that passes through the compression wave over the ramp and that which flows undisturbed on either side of the ramp. This pressure difference will necessarily cause a spilling of fluid over the sides of the ramps. The sharp edges along the sides of the ramps will cause the spilling of this fluid to wrap up into a tightly concentrated quasi-streamwise vortex that will shed into the freestream and propagate downstream. Hence, the result is a pair of counter-rotating vortices with positive axes pointed in the downstream direction inducing an upward motion of fluid at the centerline. The interaction of the

fuel jet with the vortex pair results in a dynamic mixing distribution of the fuel in the vertical and spanwise directions. Furthermore, the ramp shock will reflect off the opposite wall and impinge on the plume/vortex structure resulting in a baroclinic torque, possible vortex breakdown and further enhancement of the mixing.

3.3 Aero-Ramp Injector

The aero-ramp injector is an original design of Schetz and was first introduced by Cox et al.[28] The model used for these studies consisted of a three-by-three array of nine flush port injectors located in a square stainless steel block. A schematic and photograph of the injector insert are shown in Figures 3.8 and 3.9, respectively. The injection block was designed to be flush mounted in the tunnel test section. Each sonic injector port has an exit diameter of 0.318 cm. The equivalent diameter of the entire nine-hole array was determined by considering a single hole of equivalent area which was 0.953-cm – the same as the physical ramp studied. The first upstream row of injectors consisted of three ports with a lateral spacing of 0.953-cm, a transverse angle of 15°, and no yaw. The second row of injectors was located 2.22-cm downstream of the first row with a lateral spacing of 0.794-cm, a transverse angle of 30°, and yaw angles of -15°, 0°, and 15°. The third row of injectors was located 4.44-cm downstream of the first row with a lateral spacing of 0.635-cm, a transverse angle of 45°, and yaw angles of -30°, 0°, and 30°.

The objective of this design was to created multiple fuel-vortex interactions similar to those obtained with the physical ramp without the use of intrusive geometry. Each successive row of jets was angled higher than the previous so as to create the "aerodynamic ramp". This achieves two effects; 1) it generates an aerodynamic "effective" body to produce the large-scale vorticity, and 2) it produces three oblique shocks with total losses less than that which would be incurred with the last row of jets alone (similar to a staged supersonic engine inlet). The latter assumes that there are no expansions between the rows of jets. Therefore, the spacing between jets must be relatively small so as to simulate a single and continuous effective body. In terms of orifice diameters, this design

has a spacing of 7 dia. in the axial direction and 2-3 dia. in the lateral direction. The outer jets of each successive row are shifted inward relative to the outer jets of the previous row. This was done to achieve the aerodynamic ramp sweep angle. Multiple studies have shown the swept ramps mix better than unswept ramps. Next, the outer jets of each successive row were angled inward relative to the outer jets of the previous row. This achieves three effects; 1) it increases the lateral spread of the plume and therefore the overall mixing region, 2) it produces a skew-induced vorticity, and 3) it enhances the aerodynamic sweep angle. Next, a baroclinic torque is realized everywhere a helium jet passes through a shock wave. This will occur at each of the two downstream shock structures where the jets of the previous row impinge on the jets of the consecutive row. Finally, each of the two downstream shock structures present potential vortex breakdown and further enhancement of the near-field mixing. The goal of all this was to produce mixing performance comparable to the physical swept ramp while minimizing total pressure losses and avoiding the practical problems associated with an intrusive geometry in a high-enthalphy flow.
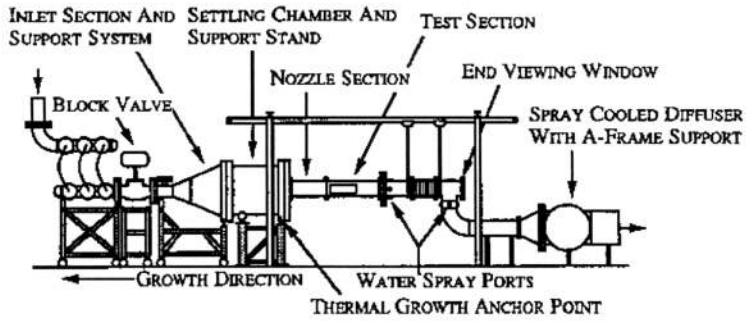
Figure 3.1   Schematic of supersonic combustion facility.
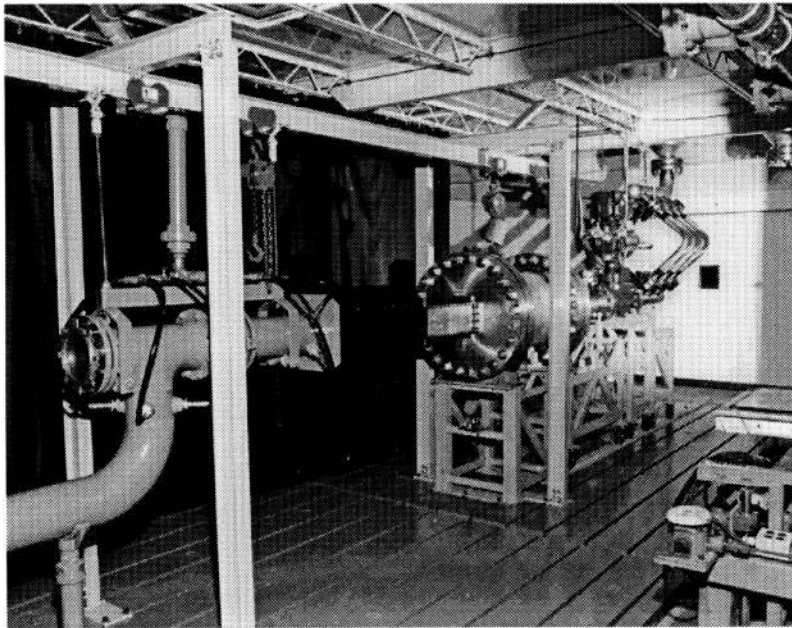
Figure 3.2   Photograph of supersonic combustion facility.

Nozzle Section:
- Transition from round to rectangular
- Two-dimensional planar nozzle
- Sidewall pressure taps along centerline

Freestream Flow

Injectant Flow

Injectant Supply Line

Test Section:
- 12.7 x 15.24 cm rectangular duct
- Quartz windows on sides and top
- Replaceable inserts for injector mounting
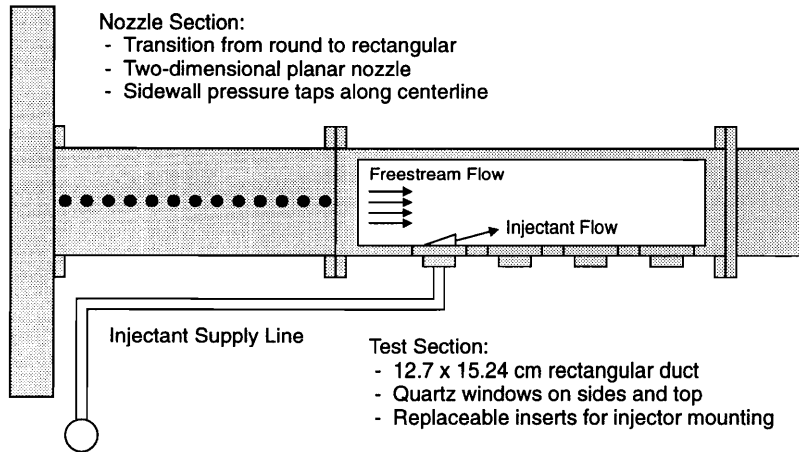
Figure 3.3 Schematic of test section.

Sliding Sidewall Section

O-ring

Nylon Ferrules

Aluminum Canister

Cap

To: Transducer (Pressure)
Gas Sampling System (Concentration)

Diamond Shaped Strut
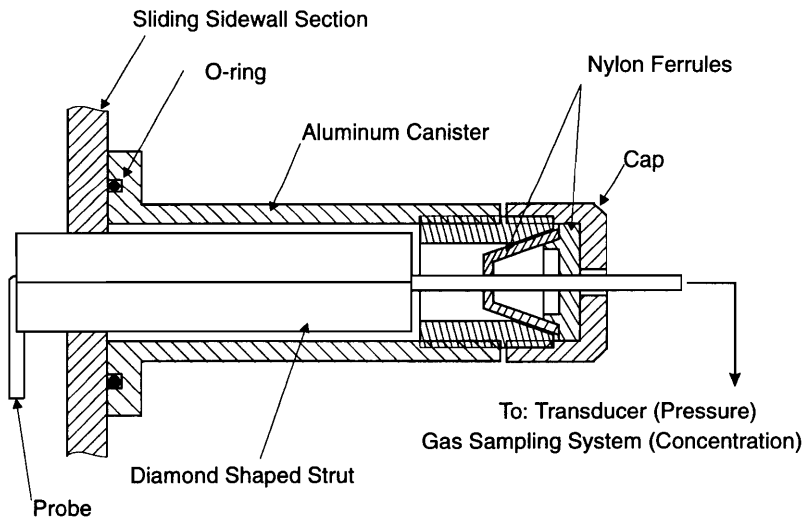
Probe

Figure 3.4 Schematic of probe insertion and sealing system.
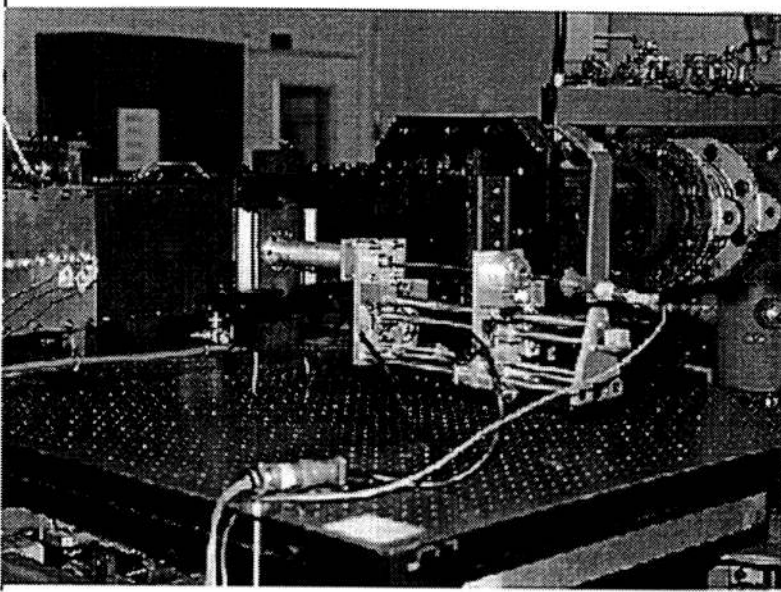
Figure 3.5 Photograph of probe actuator system.
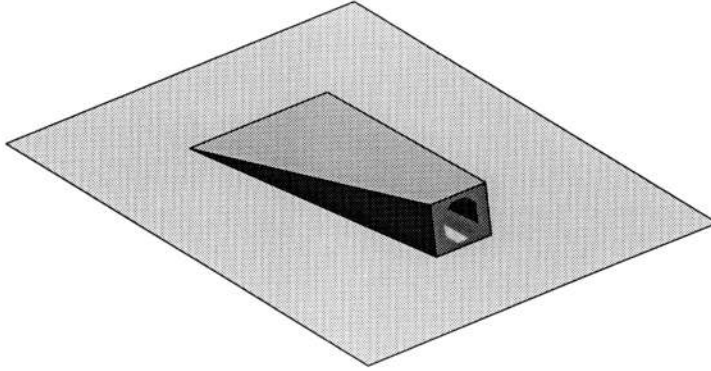
Figure 3.6 Schematic of physical ramp injector.
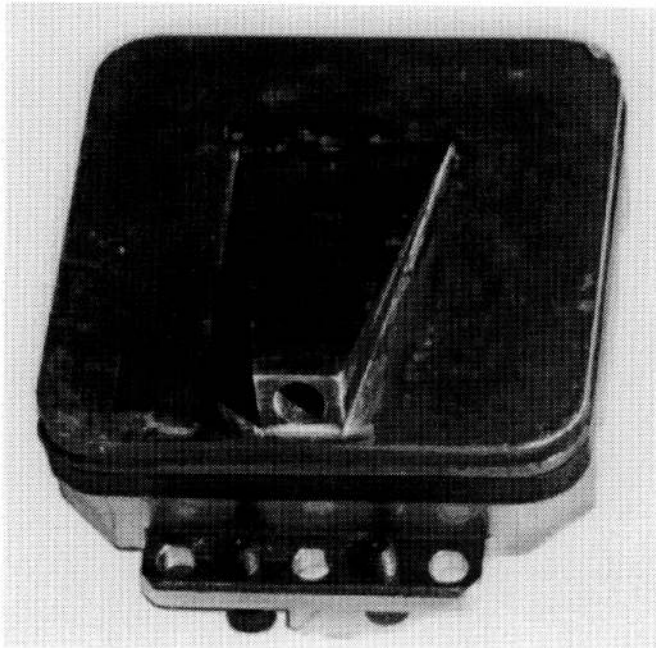
Figure 3.7 Photograph of physical ramp injector.
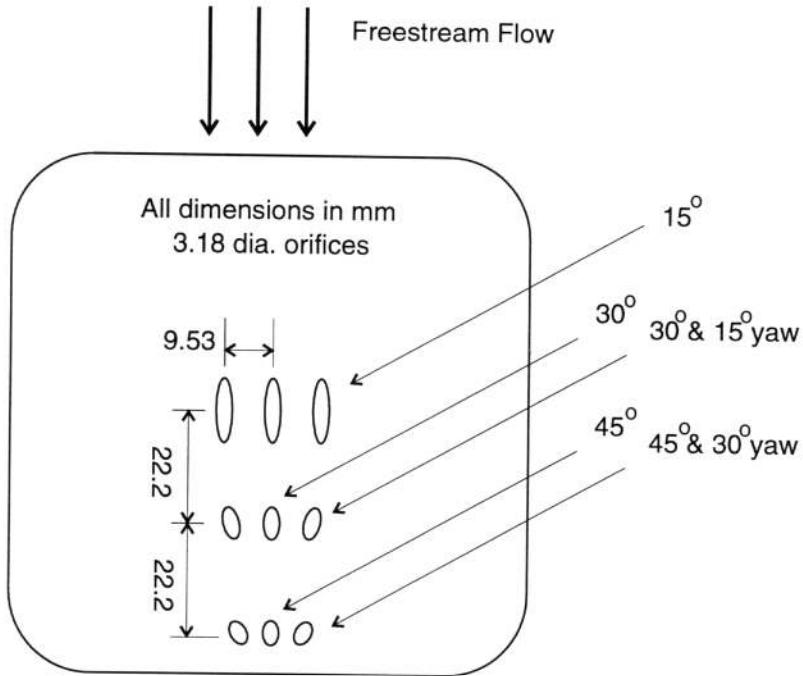
Figure 3.8 Schematic of aerodynamic ramp injector.
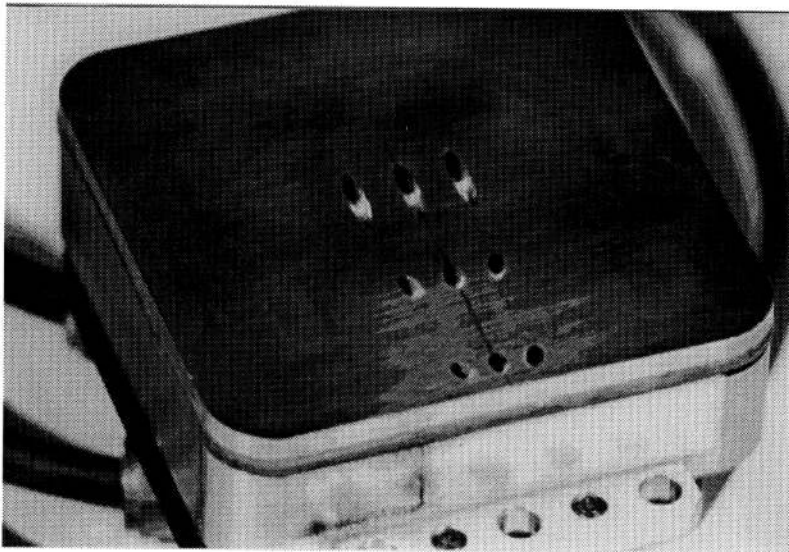
Figure 3.9 Photograph of aerodynamic ramp injector.

Experimental Methods

4.1 Shadowgraph Photography

To obtain detailed visualization of the shock structures in the immediate vicinity of the injectors, shadowgraph photography was employed. The shadowgraph method depends upon the relative deflection of a light beam by gradients in the refractive index of the gas through which the beam of light passes. For a given gas or mixture of gases and wavelength of light, the index of refraction is a function of the density. For flows with variable density or inhomogeneous gases, the light rays passing through the medium will be curved in the direction of increasing density. The amount of curvature, and therefore the deflection, is proportional to the magnitude of the density gradient. If a beam of collimated light is passed through a variable-density or inhomogeneous medium and cast onto a luminous screen, the effect of the ray deflections will be visible. The screen will show a pattern of bright and dark regions where the light rays have converged and diverged, respectively. This effect is the well known *shadow* effect. The shadow effect does not resolve absolute deflections but does resolve relative deflections. That is, the pattern on the screen shows a two-dimensional map of the deflection gradient and therefore the second derivative of the density. The dark and bright regions, respectively, correspond to positive and negative values of the second derivative of the density gradient. Thus, shock waves will appear as a dark line followed by a white line in the direction of the flow normal to the shock. Finally, it is important to note that this is a line-of-sight technique. For three-dimensional flows, the resulting two-dimensional image is an integration of all effects in the path of the light.

A standard shadowgraph technique, depicted in Figure 4.1, was employed. A continuous light source was passed through a very narrow slit aligned perpendicular to the flow direction. The light was then collimated using a parabolic mirror with a focal length of approximately 122 cm and a diameter of 25.4 cm. The collimated beam was passed through the test section and onto another parabolic mirror identical to the first. The beam was allowed to focus and then expand onto a large format, 10.2-cm by 12.7-cm, back plane camera where the images were captured on Polaroid ASA 400 Type-52 film. An iris-type shutter was placed in the path of the light to allow for timed exposures. The image distance, i, the focal distance, f, and the object distance, o, indicated in the figure, were selected so that the image focused on the tunnel centerline plane. The magnification was such that the entire field of interest was captured. The resulting magnification factor was 0.55. The exposure time was set at approximately 0.01 seconds. This exposure time was too long to effectively capture the instantaneous turbulent features of the flow, rather, the *time-averaged* image was recorded.

4.2 Mass Flow Measurements

Due to friction losses, the true mass flow rate through any injector will always be less than ideal. If these losses are significantly different between two injectors, the effective scaling between the two will be misrepresented by the nominal performance. Therefore, the true mass flow rate for a given set of operating conditions must be measured to account for these differences.

The idealized mass flow rate based on quasi-one-dimensional isentropic flow through a sonic orifice is given by

$$\dot{m}_i = \frac{P_t A^* C^*}{\sqrt{T_t}} \qquad [4.1]$$

where C^* is the critical flow function defined by

$$C^* = \sqrt{\frac{\gamma}{R}} \left(\frac{2}{\gamma + 1} \right)^{(\gamma+1)/2(\gamma-1)} \qquad [4.2]$$

However, friction losses will always reduce this value by a fractional factor known as the *discharge coefficient*, c_d. The actual mass flow rate is then given by

$$\dot{m}_a = \frac{c_d P_t A^* C^*}{\sqrt{T_t}} \qquad [4.3]$$

so that the discharge coefficient is simply the ratio of actual to ideal mass flow rate.

$$c_d = \frac{\dot{m}_a}{\dot{m}_i} \qquad [4.4]$$

The discharge coefficient of an arbitrary nozzle is a complicated function of the Reynolds number, geometry and surface roughness. In general, these effects are far too complicated to model with simple equations and must be measured experimentally. Since, the frictional losses leading to the discharge coefficient for a "well-designed" nozzle are generally a small fraction of the total mass flow rate, the measurement technique must be very accurate. For this purpose, standard circular-arc Venturi flowmeters are often employed.

The discharge coefficients for circular-arc Venturi nozzles at critical flow are well documented. Analytical predictions of the discharge coefficients were presented by Smith et al.[33] and Stratford[34] and verified by Arnberg et al.[35] through experimentation. For circular-arc venturi nozzles operating under critical (sonic) conditions, the discharge coefficient is a function of the throat Reynolds number:

$$c_d = f(Re_d); \quad \text{for sonic Venturi} \qquad [4.5]$$

where

$$Re_d = \frac{4\dot{m}_i}{\pi d^* \mu} \qquad [4.6]$$

and d^* is the Venturi throat diameter. After extensive testing of many different Venturi nozzles, with several test gases including air, nitrogen, helium, and argon the following correlation was verified by Arnberg et al.[35]:

$$c_d = 0.99738 - 3.3058 \, Re_d^{-0.5} \qquad [4.7]$$

This correlation was found to be valid for Reynolds numbers ranging from about 4×10^4 to 4×10^6 with a standard deviation of 0.105%. Thus, for a given Venturi nozzle the true mass flow rate may be determined by measuring those parameters required to compute the throat Reynolds number and therefore the Venturi discharge coefficient.

To determine the discharge coefficient of each injector for an arbitrary jet total pressure, the following procedure was employed. A circular-arc Venturi flowmeter with a throat diameter of 0.67 cm was installed serially in-line with the supply line to the injector. The injector operating conditions were varied over a wide range of total pressures. At each injectant total pressure, the static pressure at the Venturi throat and the total temperature at the inlet were measured. Assuming adiabatic flow between the inlet and the throat of the Venturi, the Reynolds number at the throat was computed using these two measurements. This Reynolds number was then used to compute the corresponding discharge coefficient for the Venturi nozzle. This number was used to calculate the true mass flow rate through the Venturi nozzle. Assuming mass continuity between the Venturi nozzle and the injector exit, the true mass flow rate through the injector was then equal to the true mass flow rate through the Venturi. The discharge coefficient for the injector could then be determined. For each injector, approximately 20 data points were taken for injectant total pressures ranging from 100 to 710 kPa. Fourth-order polynomial curve fits were constructed using a least-squares approach to predict the injector discharge coefficient over the entire range of injectant total pressures tested.

The discharge coefficient was determined for each injector over a range of injectant total pressures for a constant total temperature. Polynomial curve fits were constructed to predict the discharge coefficient at any total pressure within the range tested. In each case, the curve fit was a fourth-order polynomial with the following form:

$$C_d = c_0 + c_1 P_{t,j} + c_2 P_{t,j}^2 + c_3 P_{t,j}^3 + c_4 P_{t,j}^4 \qquad [4.8]$$

The following results were obtained:

Table 4.1 Discharge coefficient curve fit constants.

	Aero-Ramp	Physical Ramp
c_0	1.22	1.45
c_1	-2.27×10^{-2}	-3.66×10^{-2}
c_2	2.95×10^{-4}	8.56×10^{-4}
c_3	-8.02×10^{-8}	-8.25×10^{-6}
c_4	-9.97×10^{-9}	2.81×10^{-8}

where $P_{t,j}$ is expressed in psia. Note that these fits are only applicable over the range of

$100\text{kPa} < P_{t,j} < 710\text{kPa}$. For the operating conditions of the current study, the following discharge

coefficients were obtained

Table 4.2 Discharge coefficients, c_d.

	$\bar{q} = 1.0$	$\bar{q} = 2.0$
Physical	0.75	0.84
Aero	0.89	0.92

Recall that the effective injector diameter was defined as the square-root of the discharge coeffi-

cient multiplied by the injector exit diameter. Table 4.3 summarizes the effective diameters for each

injector for each case.

Table 4.3 Effective diameters, d_{eff}.

	$\bar{q} = 1.0$	$\bar{q} = 2.0$
Physical	8.24 mm	8.73 mm
Aero	8.99 mm	9.14 mm

With $\bar{q} = 1.0$, the axial test locations corresponded to $x/d_{eff} = 9.7, 14.3, 25.9, 62.8, 83.6$ for

the physical ramp and $x/d_{eff} = 7.2, 11.4, 22.0, 56.0, 75.0$ for the aero-ramp. With $\bar{q} = 2.0$, mea-

surements were taken at the furthest downstream distance only corresponding to $x/d_{eff} = 79.0$ for

the physical ramp and $x/d_{eff} = 73.8$ for the aero-ramp.

4.3 Gas Sampling

For the complete description of a flowfield generated by a fully-constrained supersonic flow

with foreign gas injection, it is necessary to obtain species composition measurements. Foreign

gas injection creates an inhomogeneous mixture of different species with possibly different ratios of

specific heats. Flow parameters such a Mach number, total pressure, etc. are functions of the local ratio of specific heats and therefore cannot be determined via conventional probing without *a priori* knowledge of the species concentrations.

For the case of air with helium injection, the local ratio of specific heats, γ can vary from 1.39 to 1.67. Almost all of the equations relating thermodynamic variables to Mach number involve γ as an exponential power. Hence, only a slight variation in its value may cause significant changes in the reduced thermodynamic values. Consequently, a technique to measure helium concentrations in a supersonic flowfield is applied before continuing with conventional probing (i.e. Pitot, cone-static, etc.).

Helium concentration measurements were obtained using an intrusive sampling probe and gas analyzer designed specifically for use in supersonic flow. This probe concept was first presented by Ninnemann et al.[36] In the present studies, the sampling probe consisted of a small Pitot tube with a conical tip and an internal divergence. See the schematic in Figure 4.3. This geometry was used so that an isokinetic sample could be extracted from the flow. Isokinetic sampling is ensured in supersonic flow by swallowing the shock into the probe. With a swallowed shock, there is no disturbance upstream of the probe and no distortion of the streamtube entering the probe inlet. The gas analyzer consisted of a hot-film sensor operating in a channel with a pressure tap and a thermocouple. The sample was drawn into the analyzer via the sampling probe and exhausted out through a choked orifice. The flow through the channel is of very low Mach number – typically 0.05. This allows for the measurement of total pressure and total temperature within the sampling channel. The gas analyzer is calibrated to measure the helium concentration uniquely related to a given pressure, temperature and heat transfer sensed at the hot-film operating plane.

4.3.1 Principle of Operation

Figure 4.2 illustrates the model used for the design studies. The sensor plane includes a hot-film sensor, pressure tap, and thermocouple. The condition for mass continuity may be expressed as

$$\rho u = P_t \sqrt{\frac{\gamma}{RT_t}} M \left[1 + \frac{\gamma - 1}{2} M\right]^{-(\gamma+1)/2(\gamma-1)} \qquad [4.9]$$

Since the flow through the choked orifice is sonic ($M = 1$), continuity reduces to

$$(\rho u)^* = \frac{P_t C^*}{\sqrt{T_t}} \qquad [4.10]$$

where C^* is the critical flow function defined by

$$C^* = \sqrt{\frac{\gamma \mathcal{M}}{\hat{R}}} \left(\frac{2}{\gamma + 1}\right)^{(\gamma+1)/2(\gamma-1)} \qquad [4.11]$$

where the * designates sonic conditions at the orifice and $\mathcal{M}$ is the molecular weight. Since the mass flow through the sensor plane must equal the mass flow through the choked orifice ($\rho u A_c = (\rho u)^* A^*$) the mass flux at the sensor plane may be expressed as

$$\rho u = \frac{P_t C^*}{\sqrt{T_t}} \frac{A^*}{A_c} \qquad [4.12]$$

Hence, the mass flux through the sensor plane is a function of the total pressure, total temperature, area ratio, and gas composition. Note that C^* is a function of the gas composition through $\mathcal{M}$ and γ (assuming caloric perfection).

Now consider the heat transfer from the hot-film sensor at the measurement plane to the passing fluid. The rate of heat transfer is given by

$$q_f = I_f^2 R_f \qquad [4.13]$$

where R_f is the film resistance and I_f is the film current supplied by the anemometer. For a constant temperature anemometer, the film current is related to the anemometer response voltage by

$$I_f = \frac{V}{R_f + R_s} \qquad [4.14]$$

where R_s is the series bridge resistance. Now define the Nusselt number in terms of the rate of heat transfer from the hot-film and the temperature difference between the film and the passing fluid as

$$Nu = \frac{q_f}{\pi k l(T_f - T_t)} \qquad [4.15]$$

where k is the thermal conductivity of the gas mixture and l is the active sensing length of the hot-film. Then, combining Equations 4.12, 4.13, and 4.14, the Nusselt number may be expressed as

$$Nu = \frac{R_f}{(R_f + R_s)^2} \frac{V^2}{\pi k l (T_f - T_t)} \qquad [4.16]$$

The Nusselt number may also be related to the mass flux via the Reynolds number, $Re = \rho u d / \mu$, where d is the film diameter as

$$Nu = a \left(\rho u \frac{d}{\mu} \right)^b \qquad [4.17]$$

and a and b are empirically determined constants. Thus, equating Equations 4.15 with 4.16 for Nusselt number and inserting Equation 4.11 for mass flux at the sensor plane, the governing equation for the anemometer response voltage is obtained.

$$V^2 = \frac{(R_s + R_f)^2}{R_f} \pi l k a \left(\frac{d}{\mu} \frac{P_t}{\sqrt{T_t}} \frac{A^*}{A_c} C^* \right)^b (T_f - T_t) \qquad [4.18]$$

The parameters, a, b, C^*, k, and μ are properties of the gas mixture and are therefore a function only of the helium concentration, X_{He}. Furthermore, since a constant temperature anemometer is to be employed, the film resistance T_f and therefore R_f are constant. Finally, the values l, d, and R_s are system parameters and remain constant. Therefore, the anemometer response voltage is a function only of the total pressure, P_t, the total temperature, T_t, and the helium concentration, X_{He}. That is

$$V = f(P_t, T_t, X_{He}) \qquad [4.19]$$

Thus, for a given total pressure and total temperature, the helium concentration is uniquely determined by the anemometer response voltage.

4.3.2 Sampling Probe

Examine concentration probe depicted in Figure 4.2. This basically comprises the complete aerodynamic path of the gas sample. The flow is from left to right beginning at the inlet of the sampling probe, through a diverging channel, the sensing plane, and out through the choked orifice.

For isokinetic sampling, the geometry must be such that the shock forming over the tip of the probe is swallowed into the divergent channel and remains there over a given range of total pressures and helium concentrations. Furthermore, it will be necessary to slow the flow to low subsonic Mach numbers at the sensing plane such that the static and total pressure are only negligibly different (i.e. $P = 0.999P_t$ for $M < 0.05$). This will allow us to determine the total pressure using a static pressure port with negligible error. Hence, the design of the extraction probe and orifice geometry entails trade-off studies between the normal shock location and Mach number at the sensor plane. It can be shown that, to satisfy mass continuity the location of the shock in the diverging inlet must be such that the following relation is satisfied.

$$\frac{P_{t,3}}{P_{t,1}} = \frac{A_1}{A_4}\left[\left(\frac{2}{\gamma+1}\right)\left(1+\frac{\gamma-1}{2}M_1^2\right)\right]^{-(\gamma+1)/2(\gamma-1)}$$

Using the above relation, parametric studies were conducted to optimize the geometry over a large range of flow conditions. A computer program was written to generate solutions of sampling Mach number, M_3, shock location, x/L, and sampling pressure, $P_{t,3}$ for a range of inlet Mach numbers, M_1, total pressures, $P_{t,1}$, and geometries, A_1/A_4. Analysis of the results showed that a geometry with $A_3/A_1 = 15$ and $A_1/A_4 = 1$ would yield optimal results for the current test conditions.

The sampling probe was constructed from 321 stainless steel tubing with an outer diameter of 3.18 mm and an inner diameter 2.36 mm. The inlet was swaged and tapered from a 0.61-mm inlet diameter over a length of 5.54 mm resulting in an internal area ratio of 15. The sampling probe was approximately 60 cm long and was terminated by the gas analyzer. Figure 4.3 shows the sampling probe geometry.

4.3.3   Gas Analyzer

Figure 4.4 illustrates the basic configuration of the gas analyzer. The gas analyzer consisted of a rectangular (84mm × 36mm × 19mm) stainless steel block housing with a 3.86-mm bore through

the center. The housing was designed to fit around the body of a TSI 1220-20 high temperature platinum hot-film sensor. This sensor was mounted internally such that the cylindrical hot-film axis was perpendicular to the flow exhausting from the sampling probe into the analyzer. A thermocouple with a 1.59-mm stainless steel sheath and exposed junction was mounted through the side of the housing such that the junction was placed within the flow and to the side of the hot-film sensor. Opposite to the thermocouple junction is a pressure tap which leads to a pressure transducer. The flow is allowed to pass through the annulus between the inner bore of the housing and the hot-film sensor body so that it may exit through a 0.61-mm diameter choked orifice located near the end opposite to the flow inlet.

4.3.4 Electronics

Data acquisition was performed with a National Instruments AT-MIO-16X multifunction input/output board installed in a Zenith 286 AT personal computer. The AT-MIO-16X has a $10\mu sec$, 16-bit, sampling ADC that can monitor up to 8 differential channels with programmable gains of 1, 2, 5, 10, 20, 50, or 100 for unipolar or bipolar input ranges.

The TSI 1220-20 hot-film sensor was used in conjunction with a Dantec Type-55M01 constant temperature anemometer fitted with a DISA Type-55M10 CTA standard bridge. The output from the hot-film sensor via the anemometer was passed through a Frequency Devices Model 9002 dual-channel programmable filter. The filter used was a low-pass, 8-pole, 6-zero elliptic type. Since only the DC characteristics of the hot-film signal are of concern in the present work, the low-pass filter was set to a cut-off frequency of 50Hz. Both the unfiltered and filtered signals are visually monitored using a Kenwood CS-2110 100MHz Oscilloscope for verification of proper operation. The filtered signal was input to the computer via the AT-MIO-16X I/O board

The pressure was determined using a Genisco PB-923 pressure transducer with a range of 0 to 100 psia. Excitation voltage and output gain was supplied by a Measurements Group 2310 signal conditioning amplifier. The excitation voltage was set to 10V while the gain was set to 350.

These settings generated a final output range of 0-10V for the 0-100 psia input range. The voltage-to-pressure calibration was obtained via a Druck DPI 500 digital pressure indicator. The output voltages for pressures ranging from 0 to 100 psia in increments of 10 psia were recorded using the above mentioned data acquisition system. A first-order relation between pressure and voltage was constructed from this data using the least-squares approximation method.

The Omega Engineering Type-K thermocouple potential was referenced using an Omega Engineering Type-K cold junction compensator. A custom calibration was obtained using an Omega Engineering temperature calibrator. The output voltages from the compensator for temperatures ranging from 482R to 1100R in increments of 50R were recorded using the above mentioned data acquisition system. A second-order relation between temperature and voltage was constructed from the data using a least-squares approximation method.

4.3.5 Calibration

The calibration procedure consisted of two steps. The first step involved recording gas analyzer data (P_t, T_t, and V) while the probe tip was inserted into a static air-helium gas mixture of known concentration at a known temperature and pressure. The second step involved reducing the data obtained from the first step and fitting logarithmic curves relating probe voltage, V, to probe pressure, P_t, at the prescribed helium concentrations and temperature levels.

The first step was achieved by inserting the probe tip into a 16.4 ℓ mixing tank with an internally mounted finned-tube gas heater. The tank was then filled to a specific pressure with air and then to a higher pressure with helium. The helium molar concentration was determined according to Dalton's law of partial pressures. The vacuum source was then applied to draw the sample in through the probe tip and out through the choked orifice. As the mixing tank was evacuated, the probe voltage and temperature were recorded at various pressures. This procedure was repeated for several different helium mole fractions between 0.0 and 1.0 and different temperature levels.

The second step was achieved by running the calibration program *xcalibr8.c* which automatically read the calibration data and generated the constants a and b in Equation 4.17 for each of the different concentration and temperature levels. These constants are then stored in the file *xcalibr8.out* to be used later by the data reduction program *xreduce.c*. Furthermore, the calibration program generated theoretical curve data over a user specified range of pressures for each of the concentration levels. This data was used for calibration verification and plotting. Figure 4.5 shows a typical calibration map used for interpolation in the data reduction procedure. Listings of the programs are provided in *Appendix B*.

4.3.6 Procedure

The sampling probe was secured within a diamond-wedge strut which connected to the probe actuator system. The actuator system was used to move the probe to each of predefined points comprising the measurement grid. The probe was initially retracted and located at the bottom wall surface. The probe tip could not be located at an absolute location of $z = 0$. There was an offset of one-half the diameter of the probe. This was approximately 1.6 mm and is denoted as z_o in the plots. Upon command, the probe was stepped to the first measurement point along the first traverse line. At this stage, the entire process was automated by the computer data acquisition and control system. The helium injection was then activated. After a two second delay, approximately 250 data samples were taken over a 1.5 second times frame. The helium injection was deactivated. As the probe was stepped to the next location, the data values were averaged and then sent to the *on-line* data reduction routine. The reduced values of helium mole fraction and mass fraction were output to the computer screen for verification. The reduced values along with the raw data values were recorded in a file. The helium injection was reactivated and the entire sequence was repeated. The probe was then advanced to next point and so on until the last measurement point was reached. After taking data at the last point along a traverse line, the helium injection was deactivated and the probe was retracted. The entire probe and actuator assembly was then moved up to the next

grid line and the entire sequence was repeated. This continued until the last horizontal line in the measurement grid was completed. One plane of data required 713 discrete measurements across the 23-by-31 point grid and took nearly one hour to complete.

4.4   Conventional Supersonic Flow Probing

A set of three conventional probes was used to interrogate the flow field at several axial stations. This set consisted of a Pitot probe, cone-static pressure probe, and a total temperature probe. Each probe was approximately 60 cm in length with a 90° bend approximately 5 cm from the tip. Midway between probe tip and the bend, each probe has a jog to allow for near-wall measurements (see Figure 4.6). The probes were secured within a diamond-wedge strut for structural rigidity, low-drag and minimal intrusion effects. The strut was then attached to the probe actuator system through the traversing wall access plate discussed previously. Each of these probes, along with the gas sampling probe, are shown schematically in Figure 4.6. Following are the descriptions of each probe used.

4.4.1   Pitot Pressure Probe

A standard round Pitot probe was used to measure the Pitot pressure. This probe was constructed from 3.18-mm stainless steel tubing with an inlet diameter of 2.34 mm, indicating a capture area of 4.29 mm^2. Flexible plastic tubing and pressure fittings were used to connect the Pitot probe to a Statham pressure transducer. This pressure transducer sensed pressures in the range of 0 to 345 kPa and converted them linearly to a corresponding voltage. The voltage output was then amplified using a Preston 8300 XWB signal amplifier before being fed to the data acquisition system. The response time constant of this system was less than 0.5 seconds.

4.4.2   Total Temperature Probe

The total temperature probe was based on an original design of Winkler[37] and is shown in Figure 4.7. The probe housing consisted of a 3.18-mm stainless steel tube with a ceramic diffuser tip. A Type-K thermocouple with a 0.38-mm spherical bead was mounted concentrically within the

diffuser tip. The diffuser tip has an inlet diameter of 1.60-mm and two side vent holes with diameters of 0.51-mm each. These vent holes were located downstream of the thermocouple bead. Geometries were chosen such that the flow entering the probe inlet would be effectively stagnated around the thermocouple bead. This design yielded a temperature recovery factor of approximately 0.98 with a response time constant (time to reach 63% of a step input) of approximately 0.01 seconds. The thermocouple leads were attached to a battery-powered Omega MCJ-K electronic ice point reference. The signal was then amplified using a Preston 8300 XWB signal amplifier before being fed to the data acquisition system.

4.4.3 Cone-Static Pressure Probe

The cone-static pressure probe consisted of a 3.18-mm stainless steel tube with a closed-end, 10° half-angle conical tip. The cone tip had four pressure taps, each of 0.51-mm diameter, located at approximately 75% of the distance from the cone vertex to the base. These pressure taps were spaced azimuthally at 90° intervals. All taps emptied into a common chamber to reduce error due to flow angularity. Flexible plastic tubing and pressure fittings were used to connect the pitot probe to a Bell & Howell pressure transducer. This pressure transducer sensed pressures in the range of 0 to 103 kPa and scaled them linearly to a corresponding voltage. The voltage output was then amplified using a Preston 8300 XWB signal amplifier before being fed to the data acquisition system. The response time constant of this system was less than 0.5 seconds.

4.4.4 Calibration

Both the Pitot and cone-static pressure systems were calibrated using a Druck DPI-500 digital pressure indicator. This device utilized highly accurate internal pressure sensors, a high-pressure dry nitrogen source, and an absolute vacuum reference to provide any absolute pressure in the range of interest. The internal pressure sensors of the DPI-500 were calibrated against a secondary standard. The pressure transducer being calibrated was connected to the DPI-500, and the pressure was varied in equally spaced increments over the entire valid range of the transducer. At each of

these increments, the voltage sensed by the data acquisition system was recorded along with the indicated pressure. A third-order, least-squares fit was then constructed using approximately 10 data points. The calibration coefficients were entered into the data acquisition system so the sensed voltage could be converted to the corresponding pressure. Before proceeding, the calibration was checked by comparing the DPI-500 readings with that of the data acquisition system over the entire range of calibration.

The total temperature system was calibrated using an Omega portable block calibrator capable of providing any reference temperature between ambient and 900 K. An additional reference temperature of 273 K was provided by an ice bath. A ten-point calibration was determined using a third-order least-squares fit. The calibration coefficients were entered into the data acquisition system so the sensed voltage could be converted to the corresponding temperature. Before proceeding, the calibration was checked by comparing the calibrator readings with that of the data acquisition system.

4.4.5 Procedure

Each probe was secured within a diamond-wedge strut which connected to the probe actuator system. The actuator system was used to move the probe to each of predefined points comprising the measurement grid. These points correspond to the same points at which the gas samples were taken. The probe was initially retracted and located at the bottom wall surface. The probe tip could not be located at an absolute location of $z = 0$. There was an offset of one-half the diameter of the probe. This was approximately 1.6 mm and is denoted as z_o in the plots. Upon command, the helium injection was activated and the probe was stepped to the first measurement point. At this stage, the entire process was automated by the computer data acquisition and control system. At each point, 1000 data samples were taken over a 0.5 second time frame, averaged, and recorded. The probe was then advanced to next point and so on until the last measurement point was reached. After taking data at the last point, the helium injection was deactivated and the probe was retracted. The entire

probe and actuator assembly was then moved up to the next grid line and the entire sequence was repeated. This continued until the last horizontal line in the measurement grid was completed. One plane of data required 713 discrete measurements across the 23-by-31 point grid and took nearly one hour to complete. Probe changes could be accomplished in about one-half of an hour. Thus, a complete set of all three probing measurements required nearly 5 hours for the completion of one data plane.

4.5 Fuel Plume Imaging

A planar-laser imaging technique was also utilized to interrogate the flow field at several axial locations. This technique involved seeding the freestream flow with very small particles while recording the scattered light (Rayleigh scattering) pattern as they pass through a sheet of laser light. Since the injectant was unseeded, the intensity of the scattered light should give some indication of the degree of mixedness. Furthermore, through specialized image processing techniques, both qualitative and quantitative mixing characteristics may be identified. The following sections discuss in detail the issues regarding the theory and implementation of this technique.

4.5.1 Rayleigh Light Scattering

For sufficiently small, spherical particles subjected to incident light, analytical models have been developed to predict the light-scattering behavior. If the particle diameter is much smaller than the wavelength of the incident light, the scattered light will be in the Rayleigh regime governed by the Rayleigh theory. If the particles are on the order of or larger than the wavelength of the incident light, the scattered light will be in the Mie regime governed by Mie theory. The scattering intensity is dependent on seed concentration, if any, gas species concentrations, temperature, density, and velocity of the scattering medium. In our application, the light scattering in the Mie regime was negligible when compared to the Rayleigh scattering. Therefore, only those issues associated with Rayleigh theory are discussed here. For more information on Mie theory, the reader should refer to van de Hulst.[38]

For Rayleigh theory to be applicable, the particle size must be small enough to satisfy the following relation

$$\frac{2\pi r_p}{\lambda_i} << 1 \qquad\qquad [4.20]$$

where r_p is the particle radius and λ_i is the wavelength of the incident light. Provided this condition is satisfied, Rayleigh theory predicts the scattering irradiance (radiant flux at a surface) to be

$$E_s = \frac{E_i}{l^2} N \sigma_p \qquad\qquad [4.21]$$

where E_i is the incident irradiance, l is the distance to the point of observation, N is the number of identical independent particles in the probe volume, and σ_p is the scattering cross-section. The scattering cross-section, σ_p, is a complicated function of the particle characteristics and the angle between the incident-beam polarization and the scattered radiation. For more information on calculating the scattering cross-section, the reader should refer to Carter et al.[39]. In general, σ_p is directly proportional to the sixth power of the particle radius ($\sigma_p \propto r_p^6$) and inversely proportional to the fourth power of the incident beam wavelength ($\sigma_p \propto \lambda_i^{-4}$).

The radiant intensity over a given solid angle, $\Delta\Omega$, is given by

$$I_s = \int_{\Delta\Omega} E_s l^2 \, d\Omega \qquad\qquad [4.22]$$

The solid angle, $\Delta\Omega$, is defined by the scattering collection optics. In most applications, for the scattered radiant intensity recorded by a photo-sensitive detector the following approximation may be used[39]

$$I_s = \epsilon E_s N_p V \sigma_p \Delta\Omega \qquad\qquad [4.23]$$

where N_p is the particle number density (particles per unit volume, $N_p = N/V$), V is the probe volume, and ϵ is the efficiency of the collection optics. Hence, the radiant scattering intensity is directly proportional to the particle number density. In many applications, the light scattering particles will be the gas molecules themselves. However, some applications involve seeding the gas with particles that are much larger than the gas molecules yet small enough to scatter in the Rayleigh

regime. In this case, the scattering irradiance produced by the gas molecules will be negligible when compared to that produced by the seed particles due to the extreme sensitivity with particle size ($\sigma \propto r_p^6$). This was the case in these studies where solid silicon dioxide particles were used as the scattering media.

4.5.2 Particle Response

In laser diagnostic applications involving seeded flows, it is crucial that the particles accurately *track* the flow. That is, the particle mass should be negligible under the influence of convective forces produced by turbulent fluctuations in the flow. This will allow for an accurate representation of the flow structures and minimal disturbance of the flow dynamics. Samimy et al.[40] showed that an acceptable particle response may be obtained for a Stokes number of less than 0.05. The Stokes number is defined as the ratio of the particle response time scale to the characteristic fluid dynamic time scale.

$$St = \frac{\tau_p}{\tau_f} \qquad [4.24]$$

The particle time scale, τ_p, is the time required for a spherical particle to accelerate from rest to 63% of a constant freestream velocity. Assuming a Stokesian drag law, Melling[41] determined the following relation

$$\tau_p = (1 + 2.76 \cdot Kn) \frac{\rho_p d_p^2}{18\mu} \qquad [4.25]$$

where ρ_p is the particle density, d_p is the particle diameter, μ is the absolute fluid viscosity, and Kn is the Knudsen number. The Knudsen number is defined here as

$$Kn = \frac{3}{2} \frac{\mu}{\rho c d_p} \qquad [4.26]$$

where ρ is the fluid density and c is the sound speed. The characteristic fluid dynamic time scale is taken to be the large-eddy rollover time. This is the shear layer vorticity thickness divided by the velocity difference across the shear layer as expressed by

$$\tau_f = \frac{\delta_\omega}{\Delta U} \qquad\qquad [4.27]$$

4.5.3 Particle Seeding Technique

The seeding technique chosen for these experiments utilized the injection and combustion of gaseous silane, SiH_4, in the air flow. A dilute mixture of 75% silane in nitrogen was injected into the air via the seed port of the wind tunnel just upstream of the settling chamber. Silane is a pyrophoric gas which, when exposed to oxygen, will spontaneously combust and produce particles of solid silicon dioxide, SiO_2. Hartman et al.[42], in their studies of the SiH_4–O_2 reaction, found that for a lean mixture of silane in air the following reaction takes place

$$3\,SiH_4 + 7\,O_2 \rightarrow 3\,SiO_2 + 6\,H_2O + O_2. \qquad\qquad [4.28]$$
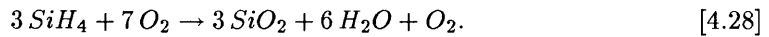
Rogers et al.[43] found that the silicon dioxide particles produced by this reaction have a nominal diameter of 0.2 μm. The density of SiO_2 is roughly 138 lbm/ft^3. These particles yielded a Stokes number, St, of 0.002. Here, the shear layer vorticity thickness, δ_ω, was taken to be the maximum plume height and the velocity difference, ΔU, was equal to the freestream velocity. The calculated Stokes number was an order of magnitude less than the upper limit of 0.05 established by Samimy et al.[40] Thus, the particles should track the flow quite well.

4.5.4 Laser Sheet Lighting

Sheet lighting was provided by a Continuum Surelite I-10 Nd:YAG pulsed laser. The 1064-nm output of this laser was passed through a second harmonic generator to produce a visible 532-nm beam with a maximum energy of 240 mJ per pulse. The pulse repetition rate was 10 Hz with a pulsewidth of 4–6 ns. The maximum pulse power corresponded to a Q-switch delay setting of about 200 μs. The shot-to-shot power drift was approximately ±5%.

The laser was mounted to a large traversing optical table located under the tunnel test section. The laser output beam was parallel to the tunnel axis. The beam was passed through the second

harmonic generator and was then turned perpendicular to the tunnel axis using a right-angle prism. The beam was then focused using a 250-mm plano-convex lens and spread into a sheet using a 50-mm plano-convex cylindrical lens. The sheet was then passed through the test section side window and terminated on the opposing side wall. The sheet thickness was at a minimum along the tunnel centerline and was estimated to be approximately 300 μm. Figure 4.8 shows a schematic of the setup. The entire setup could be traversed in either direction along the tunnel axis without readjustment of the optics. This allowed for visualization of any y–z plane along the x-axis throughout the test section.

4.5.5 Image Capturing

The images were captured using a Princeton Instruments digital image acquisition system. This system consisted of an intensified charge-coupled device (CCD) camera, a controller, pulse generator, cooling system, and software running on an Intel 80486 based PC. The CCD camera had an array of 578 by 384 pixels and a 14-bit intensity resolution. The camera was fitted with a Nikon UV-Nikkor 105-mm f/4.5 telephoto lens to improve spatial resolution. The camera intensifier gain was adjusted to optimize dynamic range. The controller was a Princeton Instruments ST-130 and the pulse generator was a Princeton Instruments PG-10. These were used in conjunction with a LeCroy 500-MHz digital storage oscilloscope to gate the camera in synchronization with the laser pulse. The cooling system consisted of a recirculating water cooler operating at 282 K. The camera interior was purged with dry air to prevent condensation from forming on the CCD elements. Finally, Princeton Instruments CSMA image acquisition software was used to capture and record the digital images on the PC. A schematic and photograph of the entire setup are shown in Figures 4.8 and 4.9, respectively.

4.5.6 Procedure

The following procedure was followed when acquiring the images. At each axial location for each injector, 100 signal images, 20 response images, and 20 background images were taken. The

purpose for each of these three image types will be explained in detail in the next chapter. The signal image included the laser sheet lighting with a seeded flow and helium injection. The response image included the laser sheet lighting with a seeded mainflow and no helium injection. The background image included laser sheet lighting with no mainflow and no injection. For any given image, the CCD camera, laser pulse, and helium injection were synchronized and computer automated. Since the $Si0_2$ particles tended to collect on the windows, periodic cleaning was necessary. Beginning with clean windows, the tunnel was started and allowed to reach the steady test conditions. Upon command, the sequence was activated and computer automation took control. The silane injection was first activated, followed by the helium injection. The system recorded 50 signal images. The helium injection was then deactivated, and the system the recorded 10 response images. The tunnel flow was then shut off and allowed to reach near vacuum conditions. With the laser still flashing, 10 background images were recorded. The windows were then thoroughly cleaned and the above sequence was repeated in reverse order. Note that half of the response and background images were recorded with "dirty" windows and the other half with clean windows. Since the signal images always begin with clean windows and end with dirty windows the correction procedures described in the next section will require both conditions for the background and response images.
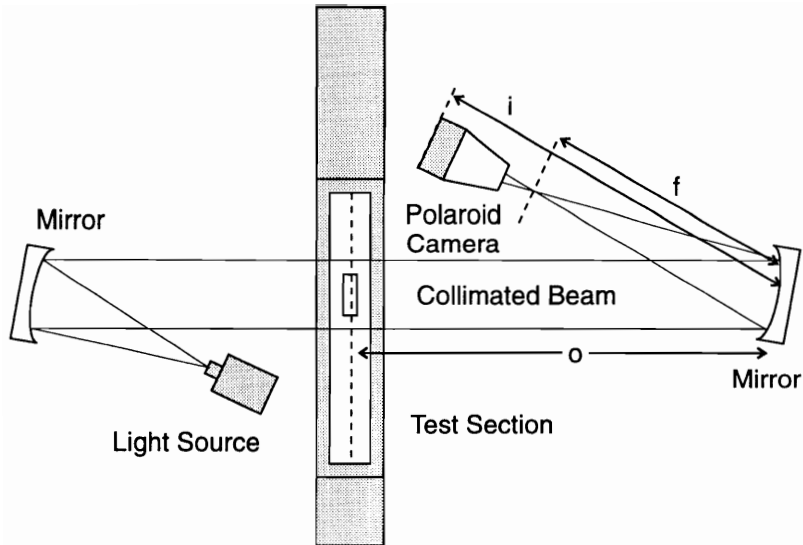
Figure 4.1   Schematic of shadowgraph photography setup.
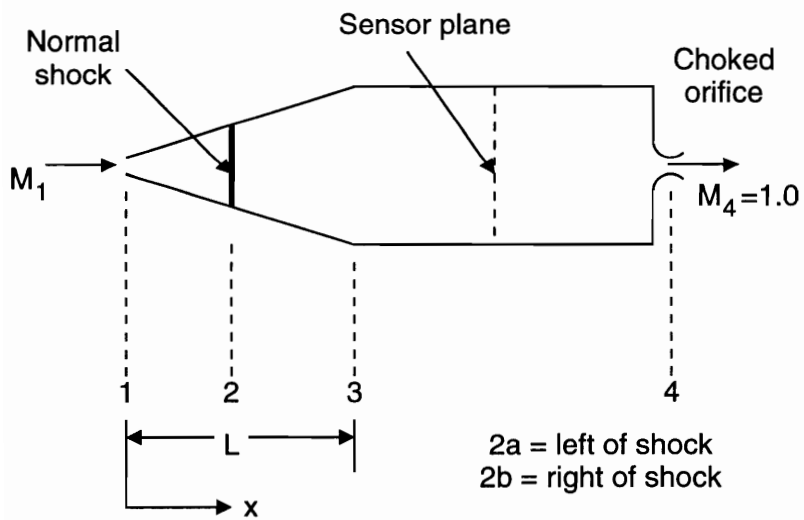
Figure 4.2   Model of gas sampling system.

All dimensions are in mm unless otherwise indicated.
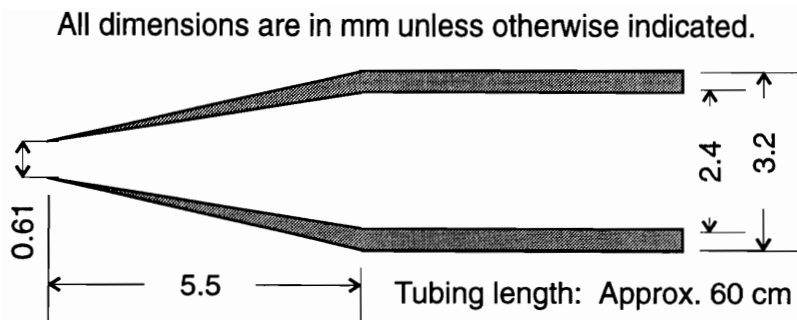
Figure 4.3 Schematic of gas sampling probe geometry.
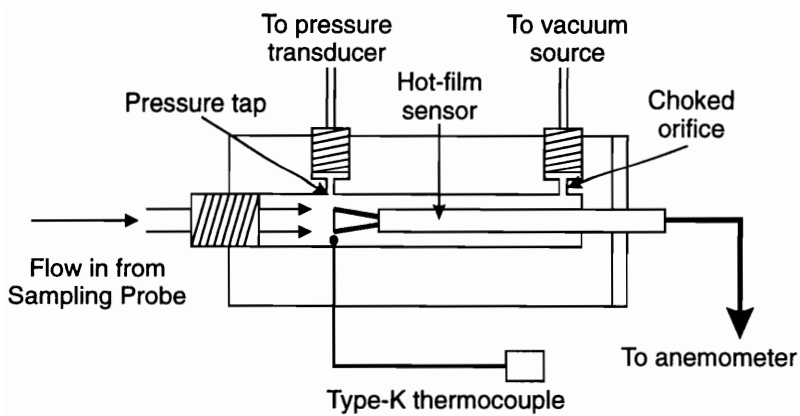
Figure 4.4 Schematic of gas analyzer.
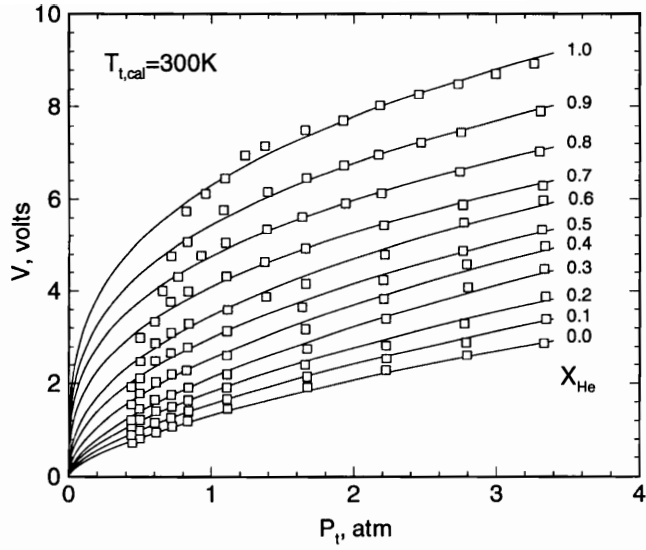
Figure 4.5   Typical gas analyzer calibration map.
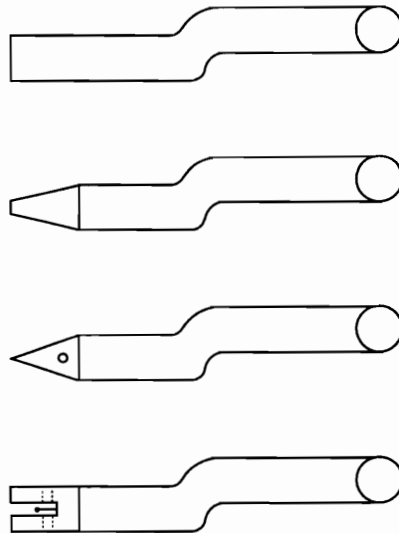
Figure 4.6   Schematic of conventional probes: Top-to-bottom; Pitot
pressure, gas sampling, cone-static pressure, and total temperature.
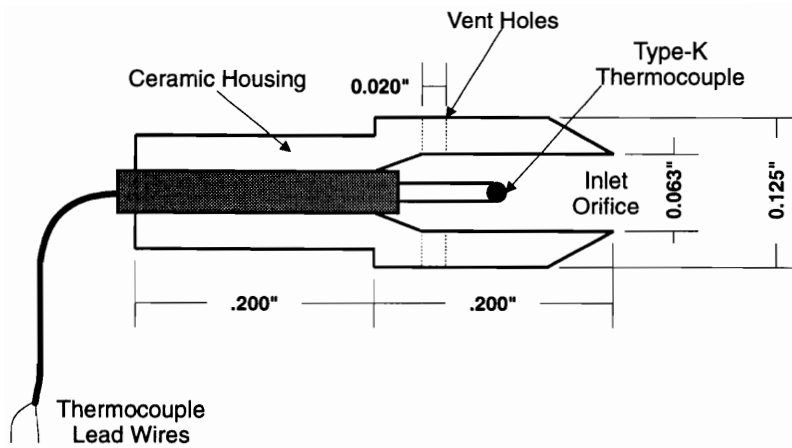
Figure 4.7 Detail of total temperature probe tip.
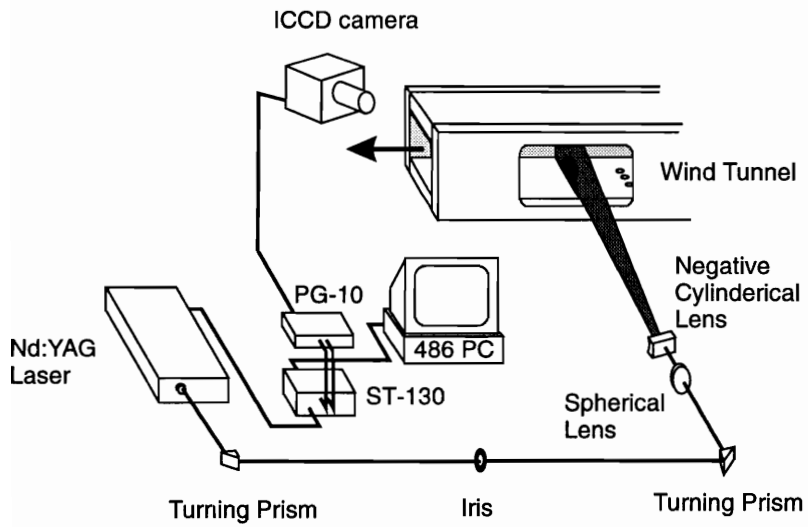
Figure 4.8 Schematic of Rayleigh imaging setup.
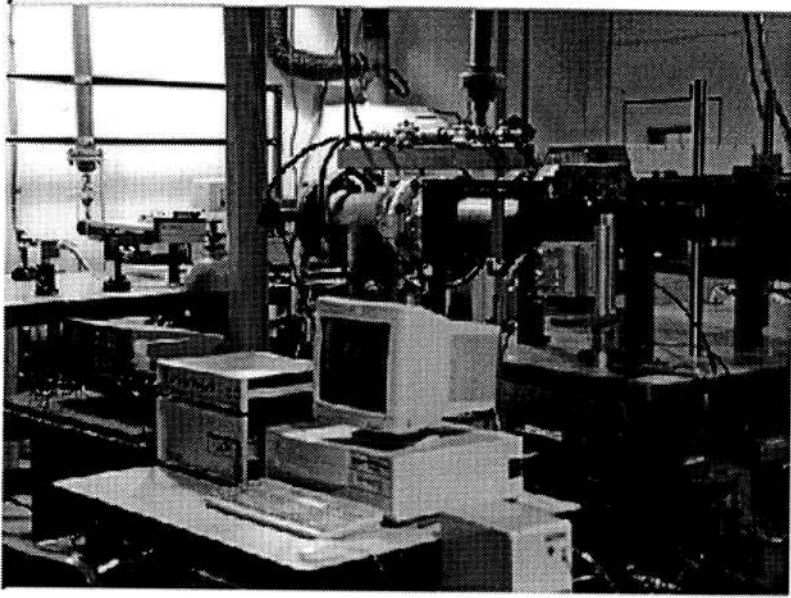
Figure 4.9   Photograph of Rayleigh imaging setup.

5.1 Gas Sampling Data

Recall that the calibration procedure for the gas analyzer yielded curve fits for various given helium concentrations and a fixed calibration temperature (see Figure 4.5). These curve fits gave the hot-film voltage as a function of sampling pressure. Thus, for a measured pair of values, hot-film voltage and sampling pressure, the helium concentration may be interpolated provided the sampling temperature is fairly close to the calibration temperature. That is, at the measured sampling pressure the measured hot-film voltage is bound between two curves representing the upper and lower bounds on the helium concentration. The measured helium concentration was linearly interpolated between these bounds using the measured voltage. For example, say that at a given sampling pressure and temperature, an anemometer response voltage of V is measured. On the calibration map at the measured sampling pressure, this voltage, V, is bounded by a higher voltage, V^+, representing a higher helium mole fraction of X_{He}^+ and a lower voltage, V^-, representing a lower helium mole fraction of X_{He}^-. So that linear interpolation will yield the measured helium mole fraction as

$$X_{He} = \frac{X_{He}^+ - X_{He}^-}{V^+ - V^-}(V - V^-) + X_{He}^- \qquad [5.1]$$

From the helium mole fraction, the helium mass fraction is determined as follows.

$$\alpha_{He} = \frac{X_{He}\mathcal{M}_{He}}{X_{He}\mathcal{M}_{He} + (1 - X_{He})\mathcal{M}_{air}} \qquad [5.2]$$

where α_{He} is the helium mass fraction, $\mathcal{M}_{He}$ is the molecular weight of helium, and $\mathcal{M}_{air}$ is the molecular weight of air. A version of the C code, *xreduce.c*, used to calculate the helium mole and

mass fractions for a measured sampling pressure, temperature and a hot-film voltage, is provide in *Appendix B.*

5.2 Conventional Supersonic Flow Probing Data

The helium concentration, cone-static pressure, Pitot pressure, and total temperature measurements were used to compute the ratio of specific heats, Mach number, total pressure, static pressure, static density, static temperature, sound speed, and velocity. The reduction of these data was performed using a computer program, *meanflow.c*, provided in Appendix B. The flow is assumed to be adiabatic and thermally perfect, but calorically imperfect. This was to allow for high-temperature applications where the specific heat of the gases may change considerably. By presuming caloric imperfection, an iterative solution was required since neither the static temperature nor the ratio of specific heats was known *a priori.* By guessing a static temperature, a ratio of specific heats could be computed. This ratio along with the cone-static pressure and Pitot pressure could be used to solve for a Mach number. This Mach number and ratio of specific heats along with the measured total temperature were used to compute a static temperature. This static temperature was compared to the original guess. If the difference was not within an acceptable tolerance, the procedure was repeated using a new static temperature guess. To automate the process a simple bisection method was applied. When an acceptable tolerance was reached, the computed ratio of specific heats, Mach number, and static temperature and the measured Pitot pressure were used to compute the remaining parameters. The following summarizes the basic data reduction algorithm and nondimensionalization scheme.

5.2.1 Data Reduction Algorithm

Inputs:

P_{t2}	Pitot pressure
P_c	cone-static pressure
T_t	total temperature
X_{He}	helium mole fraction

Outputs:

M Mach number
P_t total pressure
P static pressure
T static temperature
ρ static density
u bulk velocity
γ ratio of specific heats
c sound speed

Steps:

Step 1   Compute the specific gas constant, R, for the local helium mole fraction, X_{He}.

$$R = \frac{\hat{R}}{X_{He}\mathcal{M}_{He} + (1 - X_{He})\mathcal{M}_{air}} \tag{5.3}$$

Step 2   Guess a static temperature, T.

Step 3   Compute the ratio of specific heats, γ, for R and T.

$$c_p = \frac{\mathcal{M}_{He}X_{He}c_{p,He} + \mathcal{M}_{air}(1 - X_{He})c_{p,air}}{X_{He}\mathcal{M}_{He} + (1 - X_{He})\mathcal{M}_{air}} \tag{5.4}$$

$$\gamma = c_p/(c_p - R) \tag{5.5}$$

Step 4   Determine Mach number, M, from the ratio of cone-static to Pitot pressure, P_c/P_{t2}, and γ using a look-up table described below.

Step 5   Compute new T for M and total temperature, T_t, using the adiabatic flow relation:

$$T = T_t\left(1 + \frac{\gamma - 1}{2}M^2\right)^{-1} \tag{5.6}$$

Step 6   Repeat Steps 2–5, using a bisection root finding method, i times until

$$|T_i - T_{i-1}| \leq tol; \quad tol \sim 1\text{K} \tag{5.7}$$

Step 7   Compute static pressure, P, using the Rayleigh-Pitot formula:

$$\frac{P_{t,2}}{P} = \left[\frac{(\gamma + 1)M^2}{2}\right]^{\frac{\gamma}{\gamma-1}}\left[\frac{\gamma + 1}{2\gamma M^2 - (\gamma - 1)}\right]^{\frac{1}{\gamma-1}} \tag{5.8}$$

Step 8   Compute total pressure, P_t, using the isentropic flow relation:

$$P_t = P\left(1 + \frac{\gamma - 1}{2}M^2\right)^{\frac{\gamma}{\gamma-1}} \tag{5.9}$$

Step 9 Compute static density, ρ, and sound speed, c, using the perfect gas relations $\rho = P/RT$ and $c = \sqrt{\gamma RT}$, respectively, and the bulk velocity, u, using $u = Mc$.

The look-up table relating the ratio of $P_c/P_{t,2}$ and γ to M was generated by solving the Taylor-Mccoll equation in conjunction with the Rayleigh-Pitot formula. For supersonic flow over a cone, the governing equation was derived by Taylor et al.[44] This equation is a 2nd order, non-linear, ordinary differential equation which requires a numerical solution. Taylor showed that the ratio of cone-static surface pressure, P_c, to the freestream prssure, P_1, if a function of the Mach number, M_1, and γ.

$$\frac{P_c}{P_1} = f(M_1, \gamma) \qquad [5.10]$$

Dividing Eq. 5.10 by the Rayleigh-Pitot formula in Eq. 5.8, yields

$$M = f(P_c/P_{t,2}, \gamma). \qquad [5.11]$$

Thus, for a given cone-static pressure, Pitot pressure, and γ, the corresponding Mach number may be bilinearly interpolated using an appropriate look-up table. Numerical solution methods have been outlined by Anderson[45] and Sims[46]. Following the solution method of Sims, the Taylor-Mccoll equation was solved for a large range of Mach numbers with γ varying from 1.39 to 1.67. These solutions were combined with solutions of the Rayleigh-Pitot formula to form a very precise look-up table.

If the Mach number should drop below roughly 1.12 for the 10° half-angle cone, the cone-shock will become detached and the above solution method will be rendered invalid. This conditions was indicated when $P_c/P_{t,2}$ was greater than a critical value determined by the cone-flow solutions. When this occurred, the static pressure, P, was interpolated from the nearest non-critical points. The ratio of static-to-Pitot pressure, $P/P_{t,2}$ was then compared to the value for sonic flow, $(P/P_{t,2})_{crit}$. This value is a function of the local helium concentration and is expressed as

$$\left(\frac{P}{P_{t,2}}\right)_{crit} = \left(\frac{\gamma+1}{2}\right)^{\frac{-\gamma}{\gamma-1}} \qquad [5.12]$$

If $(P/P_{t,2}) < (P/P_{t,2})_{crit}$, the flow was supersonic and the Mach number was calculated using the Rayleigh-Pitot formula. If $(P/P_{t,2}) > (P/P_{t,2})_{crit}$, the flow was subsonic and a normal shock did not form over the Pitot probe, so that $P_{t,2} = P_t$ and the Mach number was calculated using the following isentropic flow relation:

$$M = \left[\frac{2}{\gamma - 1} \left(\left(\frac{P}{P_t} \right)^{\frac{1-\gamma}{\gamma}} - 1 \right) \right]^{1/2} \qquad [5.13]$$

Of course, the total temperature measurement is independent of the flow regime since it is conserved whether the shock wave is present or not. The remaining parameters were calculated as prescribed in the original algorithm.

5.2.2 Nondimensionalization Scheme

All lengths were nondimensionalized by an effective diameter, d_{eff}, defined as follows:

$$d_{eff} = c_d^{0.5} d_j \qquad [5.14]$$

where c_d is the injector discharge coefficient and d_j is the jet diameter. This effective diameter is the diameter of an ideal jet having a discharge coefficient of unity and a mass flow rate equal to that of the less-than-ideal jet for the same conditions. Since the aero-ramp consisted of nine individual jets, an equivalent jet diameter, d_{eq}, was defined as the diameter of a single circular orifice having the same area as the combined area of all nine orifices. This equivalent diameter of the aero-ramp was equal to the single jet diameter of the physical ramp. The effective diameter of the aerodynamic ramp was then defined as:

$$d_{eff} = c_d^{0.5} d_{eq} \qquad [5.15]$$

All dimensional quantities were nondimensionalized by their instantaneous freestream counterpart. Here, instantaneous refers to the corresponding freestream value at the instant the probing measurement was taken. This should normalize the values against small fluctuations in the nominal operating conditions. The freestream Mach number was previously measured at 1.98[29]. Along with

every probe measurement taken, the settling chamber conditions were also recorded. The freestream stagnation conditions, $P_{t,\infty}$ and $T_{t,\infty}$, were assumed to be equal to the settling chamber conditions. The freestream static pressure and temperature were calculated using the following isentropic relations:

$$P_\infty = P_{t,\infty}\left(1 + \frac{\gamma - 1}{2}M_\infty^2\right)^{\frac{-\gamma}{\gamma-1}} \qquad [5.16]$$

and

$$T_\infty = T_{t,\infty}\left(1 + \frac{\gamma - 1}{2}M_\infty^2\right)^{-1} \qquad [5.17]$$

The freestream speed of sound was determined using the perfect gas relation:

$$c_\infty = \sqrt{\gamma R T \infty} \qquad [5.18]$$

so that the freestream velocity could be calculated using the definition of Mach number:

$$M_\infty = \frac{u_\infty}{c_\infty} \qquad [5.19]$$

The freestream density was calculated using the perfect gas law:

$$\rho_\infty = \frac{P_\infty}{R T_\infty} \qquad [5.20]$$

5.3   Fuel Plume Image Data

As with most diagnostic techniques, the data obtained often does not reveal a direct measurement of the quantity desired. Just as the probing measurements require special data reduction routines to resolve the variables of interest, so do the image based measurements made here. However, it is important that the routines used to resolve the quantities of interest be purely objective. By no means should the image processing be inconsistent and subjective in the pursuit of aestheticism. Any manipulation of the data must be well founded and consistently applied to all images in question. While the "life-like" appearance of such images allows for visual interpretation, they are still nothing more than a two-dimensional array of discrete measurements. Each of these measurements represents a physical quantity and must be manipulated using only valid physical relationships. With

that said, the image processing techniques will now be described. Each of the following processes were incorporated into a comprehensive image processing package written developed by the author. A listing of the C code has been withheld due to the extreme length and complexity.

5.3.1 Correction Method

The raw images collected in this investigation were subject to many undesirable effects. These effects include nonuniform laser sheet lighting and stray light reflections off surfaces other than the intended scattering particles. Furthermore, the CCD elements of any digital camera are prone to several disturbing factors[47]. These include, blooming, smear, dark current noise, fixed-pattern noise, thermal noise, and quantum noise. A more detailed description of these disturbances is provided in *Appendix A: Error Analysis.* The method of correction used in these studies was first presented by Long.[48] The method requires that three separate images be taken at any given location. These images include a signal image, a background image, and a response image. Each pixel in an $M \times N$ image array with respective coordinates i and j will contain a single intensity value. These pixel intensities will be affected by several influences. Each of the three types of images may be represented as follows:

$$Signal_{i,j} = R_{i,j}(I_{i,j} + B_{i,j}) + F_{i,j} \qquad [5.21]$$

$$Background_{i,j} = R_{i,j}B_{i,j} + F_{i,j} \qquad [5.22]$$

$$Response_{i,j} = R_{i,j}(I^r_{i,j} + B_{i,j}) + F_{i,j} \qquad [5.23]$$

where R represents the two-dimensional detector response function, B is the background light, F is the fixed-pattern noise associated with the detectors, I is the intensity incident upon any given element of the detector, and I^r is the reference scattering intensity from a uniform density of particles, N_r. Assume that the detector response, background light, and fixed-pattern noise are the same for all three images. Dividing the difference between the signal and background images by the difference between the response and background images yields

$$Scalar_{i,j} = N_r \frac{Signal_{i,j} - Background_{i,j}}{Response_{i,j} - Background_{i,j}} = N_r \frac{I_{i,j}}{I_{i,j}^r} \qquad [5.24]$$

Hence, the resulting image is ideally one in which the pixel values are a function only of the light scattering normalized by the reference scattering. Therefore, the image should be a map of the relative particle number density.

5.3.2 Statistical Analysis

To investigate the mean properties of the flow and to make comparisons with the mean probing and sampling measurements, ensemble-averaged images were constructed. Furthermore, since each of the three images (signal, response, and background) were taken separately, the ensemble-averaged background and response images were used in the above correction process. The signal image was either an instantaneous or an ensemble-averaged one.

To obtain the ensemble-averaged image, the following computer procedure was applied. For a given group of images, either signal, response, or background, each $M \times N$ array of pixels was read into memory, converted to floating-point format and additionally stored in an $M \times N$ array of summing registers. After all the images had been processed, each of the summing register values were divided by the number of images processed. This yielded the ensemble-averaged image for the group. Mathematically speaking, each pixel having the coordinates (i, j) in the $M \times N$ array of the resulting image is represented by the following computation,

$$\bar{I}_{i,j} = \frac{1}{K} \sum_{k=1}^{K} I_{i,j} \qquad [5.25]$$

where K is the number of images to be averaged. Hence, each pixel represents the average scattering intensity sampled at that location.

To investigate the fluctuating nature of the flow in time, standard deviation images were constructed. This allowed for the examination of information not available with the probing and sampling measurements. Using the ensemble-averaged image constructed above, the standard deviation of each pixel location was computed according to the usual definition,

$$\sigma_{i,j} = \left[\frac{1}{K-1} \sum_{k=1}^{K} (I_{i,j} - \bar{I}_{i,j})^2 \right]^{1/2} \qquad [5.26]$$

The resulting image is one in which the regions of high intensity indicate the largest fluctuations in fuel-air mixture ratios. These fluctuations show where the bulk of the mixing is occurring.

5.3.3 Histogram Equalization

All processed images were resolution enhanced through a histogram equalization process. The histogram of each final image was produced by dividing the range of pixel intensities up among 1000 equally spaced bins and plotting the bin population versus mean bin value. The histogram was then analyzed for the minimum and maximum bin intensities represented by those bins containing less than 1% of the maximum bin population. These minimum and maximum intensity values were then used to rescale each pixel according to the following operation:

$$\bar{I}_{i,j} = 255 \frac{I_{i,j} - I_{min}}{I_{max} - I_{min}} \qquad [5.27]$$

Hence, the minimum intensity of the image would be represented by a value of 0 while the maximum intensity would be represented by 255. Each pixel value was then converted to an 8-bit integer format.

5.3.4 Low-Pass Filtration

These processes often yielded a *salt-and-pepper* pattern where small, discreet groups of pixels were saturated at either the low or high intensity extremes. To reduce these effects, the final image output was low-pass filtered using a simple spatial averaging operator. To apply this operator, a standard convolution technique was utilized. For each pixel having the coordinates (i, j), a local neighborhood was defined by the collection of pixels in a subarea enclosing the pixel (i, j). In general, the neighborhood will have the dimensions of $(2K + 1) \times (2L + 1)$ such that the neighborhood $\mathbf{F}$ of the pixel (i, j) is defined by the following matrix:

$$\mathbf{F} = \begin{pmatrix} f_{i-K,j-L} & f_{i-K,j-L+1} & \cdots & f_{i-K,j+L} \\ f_{i-K+1,j-L} & f_{i-K+1,j-L+1} & \cdots & f_{i-K+1,j+L} \\ \vdots & \vdots & \ddots & \vdots \\ f_{i+K,j-L} & f_{i+K,j-L+1} & \cdots & f_{i+K,j+L} \end{pmatrix} \qquad [5.28]$$

A local neighborhood operation is one which maps each element of $\mathbf{F}$ into a single output pixel (i, j). If the operation does not depend on the pixel position, it is called *space invariant*. Furthermore, if the operation is linear, it is called a *discrete convolution*. In this case, the operator is a matrix of weighting factors, $\mathbf{W}$, given the term *convolution kernel*. The convolution kernel, $\mathbf{W}$, has the same dimensions as $\mathbf{F}$ and is defined by:

$$\mathbf{W} = \begin{pmatrix} w_{-K,-L} & w_{-K,-L+1} & \cdots & w_{-K,L} \\ w_{-K+1,-L} & w_{-K+1,-L+1} & \cdots & w_{-K+1,L} \\ \vdots & \vdots & \ddots & \vdots \\ w_{K,-L} & w_{K,-L+1} & \cdots & w_{K,L} \end{pmatrix} \quad [5.29]$$

Each output pixel (i, j) is then simply the inner product of $\mathbf{W}$ with $\mathbf{F}$ expressed by

$$\bar{I}_{i,j} = \mathbf{W}^t \mathbf{F} = \sum_{k=-K}^{K} \sum_{l=-L}^{L} w_{k,l} f_{j-k, i-l} \quad [5.30]$$

where $\mathbf{W}^t$ is the transpose of the matrix $\mathbf{W}$. For our purposes, the convolution kernel, $\mathbf{W}$, was simply a 3×3 $(K = 1, L = 1)$ averaging operator used to suppress the high-frequency content within the image. The averaging operator is defined by:

$$\mathbf{W} = \frac{1}{9} \begin{pmatrix} 1 & 1 & 1 \\ 1 & 1 & 1 \\ 1 & 1 & 1 \end{pmatrix} \quad [5.31]$$

After applying this operator to each of the images, the *salt-and-pepper* patterns were removed and the overall image content was unaltered.

5.3.5 Image Warping

The final process involved correcting for the camera angularity. Since the camera viewed the image plane from an angle, the perspective and aspect ratios were altered. The camera line-of-sight was approximately 27° off the tunnel axis. As a result, the image width was contracted to 89% of its true width and the height was skewed from end to end. The *Adobe Photoshop* image processing software was used to correct these issues, by stretching the image horizontally by a factor of 1.12 and re-skewing the image back into a rectangular shape.

6
Results

6.1 Shadowgraph Photography

Figures 6.1 through 6.10 show shadowgraph images of the physical ramp and aero-ramp injectors at various operating conditions. In all cases, the flow is from left to right, and the injector is at the bottom of the image. It is important to bear in mind that these flows are highly three-dimensional and one must exercise caution in interpreting the shock structures.

To separate the effects of geometry and fuel injection, shadowgraphs were also made with the main flow and no fuel injection. Figures 6.1 and 6.2 show the shadowgraph images of the physical ramp and aerodynamic ramp in a Mach 2.0 flow, without fuel injection. The oblique shocks crossing at the extreme left edge of the images originate at the interface between the nozzle and test sections. These are weak disturbances with the angle of a Mach wave in a Mach 2.0 flow. In Figure 6.1, the oblique shock wave originating at the leading edge of the ramp is clearly seen. The angle of this shock is approximately 38° which is slightly less than that predicted for a 10.3° wedge in a Mach 2.0 flow. This is a result of the three-dimensional relieving effect on the ramp similar to a cone of the same angle. Further downstream, a strong oblique shock forms where the flow must negotiate the turn at the wall after expanding over the separated region behind the ramp base. In Figure 6.2 for the aerodynamic, weak shocks form at each of the injector ports. Otherwise, there are no strong shocks present. Hence, the losses due to geometry will be minimal for the aerodynamic ramp.

To visualize the basic shock structure of the underexpanded fuel jet, shadowgraphs were taken with air injection and no main flow. While the injection of helium and the presence of a main flow will most certainly change the appearance of the shock structure, the basic features of the flow in the

jet(s) are often difficult to identify in the presence of the main flow. These images provide a reference when attempting to identify the jet shock structures in the more complicated cases. In each case, the injectant total pressure was set to either 300 kPa or 601 kPa. These pressures would correspond to jet-to-freestream momentum flux ratios, $\bar{q}$, of 1.0 and 2.0, respectively, if the main flow ($M_\infty = 2.0$; $P_{t,\infty} = 310 kPa$) were present. The back pressure in the tunnel test section was subject to exhauster conditions and was approximately 18.2 kPa. This resulted in jet underexpansion ratios of 7.9 and 15.9, respectively. This back pressure was lower than the freestream static pressure obtained with the Mach 2.0 flow. However, we had very little control over this.

Figure 6.3 shows the physical ramp with air injection and no main flow. The upper edge of the barrel shock is clearly present and terminates at the upper edge of the Mach disk. The bottom edge of the barrel shock impinges on the wall surface and causes a reflected shock to intersect with the Mach disk. This reflected shock causes a discontinuity in the slope of the Mach disk at the point of intersection. The remaining length of the lower edge of the barrel shock terminates at the bottom edge of the "kinked" Mach disk. In Figure 6.4, the injectant total pressure was increased to 600 kPa which would correspond to a $\bar{q}$ of 2.0 if the main flow were present. The basic structure did not change, but the overall size did increase. The upper edge of the barrel shock is fuller and more rounded allowing for the greater degree of expansion required to meet the conditions of the quiescent medium. Also, note that the Mach disk is more "kinked" due to the stronger shock reflected off the bottom wall surface. If the injectant were helium, the Mach disk would be approximately the same distance from the jet exit, but the barrel shock would be smaller. The presence of the main flow will, of course, cause a deflection of the whole jet in the downstream direction.

Figures 6.5 and 6.6 show the aerodynamic ramp with air injection and no main flow. In these images, it is difficult to clearly discern the shock structures in each row of jets due to the integration through the three jets across the span. Recall that each of outer jets in the second and third rows are yawed inward. This results in a very complicated and highly three-dimensional flow field. In any event, the jet exits are indicated by the dark nubs within the bright shock structures. The

bright regions surrounding these dark nubs outline the interior of the barrel shock. The dark regions surrounding the barrel shocks outline the jet boundary. The Mach disks are not clearly discernible in any case. Perhaps the most interesting thing to be noted is the effective jet angle. It is quite clear that each of the jets exit at angles greater than their respective injector port angles. This should be expected since the presence of the lower wall prohibits the jet from expanding on the bottom edge to the same degree that it may on the upper edge. Hence, this will cause an upward deflection of the jet. Of course, the presence of a main flow will tend to deflect the jet downstream back towards the wall. This downward deflection of the jet resulting from the main flow should be dependent on the effective back pressure defined in the analogy presented by Schetz, et al.[2] Thus, it appears that the effective jet angle in the main flow case will be difficult to predict. In any event, the approximate effective jet angles for each of the three rows of jets exhausting into a quiescent medium were as follows: for transverse injector port angles of 15°, 30°, and 45°, the respective effective transverse angles were roughly 18°, 34°, and 50° for $P_{t,j} = 300$ kPa and 26°, 43°, and 62° for $P_{t,j} = 601$ kPa. As should be expected, the deflection was greater for the larger injectant pressure. Finally, note the vertically oriented long thin dark regions over the top of the jet structures. These are, presumably the results of impingement of each of the three jets in the second and third rows. There should be no impingement of the first row of jets, since the outer jets are not yawed inward.

Figures 6.7 and 6.8 show the physical ramp injector with helium injected into a Mach 2.0 main flow with a $\bar{q}$ of 1.0 and 2.0, respectively. In both figures, the oblique shock wave originating at the leading edge of the ramp is clearly seen. The angle of this shock is approximately 38° which is slightly less than that predicted for a 10.3° wedge in a Mach 2.0 flow, a result of the three-dimensional relieving effect. Just downstream of the top edge of the ramp base, a recompression shock, similar to a lip shock on a rearward facing step, is observed in both cases. As the flow expands over the ramp base it encounters the jet plume and must negotiate an upward deflection which results in a recompression wave originating at the fuel-air interface. Further downstream along the fuel-air interface, the shock wave originating at the upper edge of the jet Mach disk is clearly seen. Note

that the barrel shock and Mach disk may not be clearly seen in these photographic reproductions. In the case of $\bar{q} = 1.0$, shown in Figure 6.7, two subsequent compression waves following the one formed at the upper edge of the Mach disk can be observed. In the case of $\bar{q} = 2.0$, shown in Figure 6.8, only the wave originating at the Mach disk is observed, however it is stronger than that observed in the previous case. Various weak shocks appear in the jet plume, however these shock are outside the centerline plane and are a result of three-dimensional effects. For background information on the structure of underexpanded jets in a supersonic main flow, the reader should refer to Ref. 5. Finally, note that the observed plume height does not change appreciably when $\bar{q}$ is increased from 1.0 to 2.0. This should be expected, since most of the jet momentum is in the freestream direction,

Figures 6.9 and 6.10 are shadowgraph images of the aerodynamic ramp injecting helium into a Mach 2.0 main flow with jet-to-freestream momentum flux ratios of 1.0 and 2.0, respectively. In both figures, the nine jet interaction shocks appear as three composite shock structures forming over each of the three rows of jets. In the case of $\bar{q} = 1.0$ shown in Figure 6.9, the shocks are curved near the wall and become nearly straight just above the jet plume. The initial shock angles near the wall upstream of the first, second, and third rows are approximately 48°, 40°, and 38°, respectively. All shocks reach a final angle of approximately 35° in the field of view. In the case of $\bar{q} = 2.0$, shown in Figure 6.10, the shocks appear to be stronger, and the jet penetration has increased significantly when compared to the previous case. Indeed, the shocks are stronger with initial angles near the wall upstream of the first, second, and third rows of approximately 55°, 42°, and 41°, respectively. Again all shocks reach a final angle of approximately 35°.

6.2 Probing and Sampling

6.2.1 General Flowfield Structure

Figure 6.11 shows the profiles of helium mass fraction at each of the five stations sampled for the physical ramp injector operating with a jet-to-freestream momentum flux ratio of $\bar{q} = 1.0$. Note that the contour color-scales are not consistent between plots. While the minimum value indicating

the plume boundary is fixed at a mass fraction value of one-half of one percent, the maximum value corresponds to the local station maximum. This was done to preserve structural details of the plume as the mass fractions vary over three orders of magnitude. At $x/d_{eff} = 9.7$, the jet potential core ($\alpha_{He} = 1$) still persists in the plume. On the left and right sides of the plume there are small triangular structures of low-concentration helium. These are the effect of the two counter-rotating vortices stripping helium away from the sides of the plume. At $x/d_{eff} = 14.3$, the plume shape changed dramatically. The helium has begun to wrap around the vortices and lift away from the wall surface at the centerline. At $x/d_{eff} = 25.9$ the helium has now completely enveloped the vortex structure with the maximum concentration occurring at the two vortex cores. At $x/d_{eff} = 62.8$, the vortex pattern convected upwards into the freestream and carried the fuel plume with it. The maximum helium mass fraction is still found in each of the vortex cores. At $x/d_{eff} = 83.6$, it is clear that the mixing distribution is no longer dominated by the vortex structure, and diffusive mechanisms have taken over. The overall structure of the plume is very similar to that observed in the previous plot. The overall area of the plume increased and the maximum helium mass fraction decreased. Again, the maximum helium concentration is located in what remains of the two vortex cores.

Figure 6.12 shows the profiles of helium mass fraction at each of the five stations sampled for the aero-ramp injector operating with a jet-to-freestream momentum flux ratio of $\overline{q} = 1.0$. Again the contour color-scales are not consistent between plots so as to preserve plume structural detail. At $x/d_{eff} = 7.21$, three distinct jet cores appear in the single composite plume produce by the entire nine-jet array. These jet cores are produced by the furthest downstream row of jets. The maximum helium concentration is about one-half of the value produced by the physical ramp at $x/d_{eff} = 9.7$ where the potential core still persists. The diameter of each individual jet comprising the aero-ramp is one-third the size of the single orifice of the physical ramp, therefore the multiple potential cores of the aero-ramp will be much shorter than the single potential core of the physical

ramp. This will result in a substantially larger decay rate of the helium concentrations in the near-field. At $x/d_{eff} = 11.4$, the three previously distinct jet cores have now merged into a single core at the center with the maximum mass fraction occurring near the wall. At $x/d_{eff} = 22.0$, the jet core lifted away from the wall and penetrated farther into the freestream. At $x/d_{eff} = 56.0$, the jet core split into two leaving behind a secondary core in the boundary layer. This was originally identified by Cox et al.[28] as being the effect of two large counter-rotating vortices generated by the aero-ramp in the very near field. These vortices induce an upward motion at the centerline, disperse helium outward at the top, and entrain air inward near the bottom. This results in the apparent bottlenecking of the plume. At $x/d_{eff} = 75.0$, the plume has become more rounded and the two cores are beginning to merge as diffusive mechanisms take control.

Figure 6.13 shows the profile of helium mass fraction at the fifth station sampled for both the physical ramp and aerodynamic ramp injectors operating with a jet-to-freestream momentum flux ratio of $\overline{q} = 2.0$. For the physical ramp, the plume is much fuller compared to the $\overline{q} = 1.0$ case, however there is no discernible change in the penetration. Furthermore, there is only one single maximum in the helium concentration occurring near the plume center indicating a weaker effect of the dual-vortex structure on the mixing distribution. This should be expected, since the higher jet momentum will tend to weaken the vortex structure. For the aerodynamic ramp, the higher $\overline{q}$ also produces a fuller profile. However, unlike with the physical ramp, the penetration increased significantly with $\overline{q}$. Furthermore, the added jet momentum seems to enhance the vorticity generation as indicated by the increased bottlenecking and separation of the primary and secondary cores.

6.2.2 Penetration Trajectory

Overall plume penetration is defined here as the vertical height from the wall surface to the edge of the mixing region where the fuel mass fraction is 0.5%. The penetration trajectory is then defined as the variation with downstream distance of the plume penetration in the vertical centerline plane. Tables 6.1 and 6.2 summarize the penetration heights versus axial distance for the physical ramp

and aero-ramp, respectively, operating at $\bar{q} = 1.0$. Table 6.3 shows the penetration height at the last measurement station for both the physical ramp and aero-ramp operating with $\bar{q} = 2.0$.

Table 6.1 Penetration height; physical ramp, $\bar{q} = 1.0$.

x/d$_{\text{eff}}$	h/d$_{\text{eff}}$
9.7	1.23
14.3	2.16
25.9	4.00
62.8	6.16
83.6	7.08

Table 6.2 Penetration height; aero-ramp, $\bar{q} = 1.0$.

x/d$_{\text{eff}}$	h/d$_{\text{eff}}$
7.2	1.13
11.4	1.41
22.0	2.54
56.0	3.68
75.0	3.96

Table 6.3 Penetration height; aero-ramp and physical ramp, $\bar{q} = 2.0$.

Injector	x/d$_{\text{eff}}$	h/d$_{\text{eff}}$
Physical	79.0	6.13
Aero	73.8	5.60

The penetration trajectories of both injectors are quite complicated in the near field and appear to jump almost discontinuously between $12 < x/d_{eff} < 22$. To predict penetration accurately in the far-field region, where the trajectories are more well behaved, curve fits were constructed correlating penetration height with downstream distance for $\bar{q} = 1.0$. Past studies[7,8,30] have shown the penetration height to vary exponentially with axial distance in the far-field region. Power-law curve fits were constructed using only the data obtained from the last three axial locations. The correlations for $x/d_{eff} > 20$ and $\bar{q} = 1.0$ are as follows: for the physical ramp,

$$h/d_{eff} = 0.95(x/d_{eff})^{0.49} \qquad [6.1]$$

and for the aerodynamic ramp,

$$h/d_{eff} = 0.87(x/d_{eff})^{0.37}. \qquad [6.2]$$

These predictions are shown in Figure 6.14 along with the measured penetration heights at each axial location. Also shown are the penetration heights for each injector at the furthest downstream location with $\bar{q} = 2.0$.

Note that when $\bar{q}$ is increased to 2.0 the normalized penetration for the aero-ramp increases while for the physical ramp it decreases. Recall that, the penetration is nondimensionalized by the effective diameter which is a function of the injector discharge coefficient. The increase in $\bar{q}$ resulted in an increase in the injector discharge coefficient and, therefore, the effective diameter as well. The absolute penetration does indeed increase in both cases, however they are scaled by larger effective diameters. In any event, these results suggest that with further increases in $\bar{q}$ the penetration height for the aero-ramp may surpass that of the physical ramp.

6.2.3 Decay of Maximum Concentration

The decay of maximum concentration with downstream distance for the injectors is presented in Figure 6.15. Tables 6.4 and 6.5 summarize the maximum concentrations versus axial distance for the physical ramp and aero-ramp, respectively, operating at $\bar{q} = 1.0$. Table 6.6 shows the maximum concentration at the last measurement station for both the physical ramp and aero-ramp operating with $\bar{q} = 2.0$.

Table 6.4   Maximum He mass fraction; physical ramp, $\bar{q} = 1.0$.

x/d_{eff}	α_{max}
9.7	1.000
14.3	0.598
25.9	0.160
62.8	0.065
83.6	0.052

Table 6.5   Maximum He mass fraction; aero-ramp, $\bar{q} = 1.0$.

x/d_{eff}	α_{max}
7.2	0.533
11.4	0.318
22.0	0.200
56.0	0.092
75.0	0.074

Table 6.6 Maximum He mass fraction; aero-ramp and physical ramp, $\overline{q} = 2.0$.

Injector	x/d$_{\text{eff}}$	α_{max}
Physical	79.0	0.066
Aero	73.8	0.088

In general, the decay of maximum concentration proceeds exponentially with downstream distance so that it may be correlated using an appropriate power law. The following form can be used to obtain a decay rate, n.

$$\alpha_{max} = \beta \left(x/d_{eff} \right)^{-n} \tag{6.3}$$

A larger value of n indicates a faster overall rate of decay. Using the data obtained in the experiments, correlations were constructed using a least squares approach. The correlations for $\overline{q} = 1.0$ are as follows: for the physical ramp,

$$\alpha_{max} = 21.8(x/d_{eff})^{-1.40} \tag{6.4}$$

and for the aerodynamic ramp,

$$\alpha_{max} = 2.6(x/d_{eff})^{-0.82}. \tag{6.5}$$

The decay rate for the physical ramp injector was 1.40 and for the aero-ramp injector it was 0.82. The physical ramp injector exhibits a very high rate of decay when compared to the average rate of 0.8 determined through an extensive review study conducted by Schetz et al.[9] However, note that in the near-field region the initial decay produced by the aero-ramp upstream of the first measurement station is far superior to that of the physical ramp injector. As a result, the far-field values of maximum concentration are comparable despite the large decay rate produced by the physical ramp downstream of the first measurement station. Setting $\alpha_{max} = 0.0292$, the stoichiometric mass fraction of hydrogen in air, and solving for x/d_{eff} gives the distance at which all of the mixture is at or below the stoichiometric mass fraction of hydrogen in air. At this distance, denoted as x_{fm}, the injectant is considered "fully mixed." For the physical ramp, the fully mixed distance is $113\, d_{eff}$ and

for the aero-ramp, it is $240\,d_{eff}$. While these fully-mixed distances are quite different, the near-field fuel concentrations will certainly have a strong impact on flame ignition and combustion.

When plotting α_{max} for different values of $\bar{q}$ it is appropriate to account for the added fuel mass by rescaling the axial distance with the square-root of the jet-to-freestream mass flux ratio. This is essentially the same as correcting for the discharge coefficient by considering the effective jet diameter when nondimensionalizing the axial distance. Figure 6.16 shows the maximum helium mass fraction plotted against this variable. As a result of the correlation, when $\bar{q}$ was increased to 2.0, the maximum fuel mass fraction is nearly equal to that predicted for the case of $\bar{q} = 1.0$.

6.2.4   Relative Plume Area

The overall plume, area, A is defined here by that area enclosed by the outermost contour representing a fuel mass fraction of 0.5%. Figure 6.17 shows the relative plume area versus axial distance for each case tested. The relative plume area is defined as follows.

$$\bar{A} = \frac{A - A_u}{A_s - A_u} \qquad [6.6]$$

where A_u is the area to which a segregated jet (a perfectly unmixed jet) would expand if allowed to reach a uniform static pressure equal to the freestream and A_s is the area required for a uniformly stoichiometric jet given the jet-to-freestream mass flux ratio and jet exit area at the freestream pressure defined by:

$$A_s = \frac{\lambda}{\alpha_s} A_j \qquad [6.7]$$

Thus $\bar{A}$ is a measure of the degree to which the plume has expanded. A_u and A_s will vary with the jet operating conditions. An increase in $\bar{q}$ will result in a linear increase in A_u and A_s. Therefore, a constant value of $\bar{A}$ with increasing $\bar{q}$ means the plume is growing in proportion to $\bar{q}$.

Tables 6.7 and 6.8 summarize the relative plume areas versus axial distance for the physical ramp and aero-ramp, respectively, operating at $\bar{q} = 1.0$. Table 6.9 shows the relative plume area at the last measurement station for both the physical ramp and aero-ramp operating with $\bar{q} = 2.0$.

Table 6.7   Relative plume area; physical ramp, $\bar{q} = 1.0$.

x/d$_{\text{eff}}$	A
9.7	0.084
14.3	0.296
25.9	0.639
62.8	1.261
83.6	1.538

Table 6.8   Relative plume area; aero-ramp, $\bar{q} = 1.0$.

x/d$_{\text{eff}}$	A
7.2	0.238
11.4	0.242
22.0	0.491
56.0	0.686
75.0	0.901

Table 6.9   Relative plume area; aero-ramp and physical ramp, $\bar{q} = 2.0$.

Injector	x/d$_{\text{eff}}$	A
Physical	79.0	0.974
Aero	73.8	0.872

The correlations for $x/d_{eff} > 20$ and $\bar{q} = 1.0$ are as follows: for the physical ramp,

$$\bar{A} = 0.06(x/d_{eff})^{0.75} \qquad\qquad [6.8]$$

and for the aerodynamic ramp,

$$\bar{A} = 0.12(x/d_{eff})^{0.46}. \qquad\qquad [6.9]$$

In the near-field, the plume area produced by the aero-ramp is larger than that produced by the physical ramp. In the far-field region, the plume produced by the physical ramp quickly grows and surpasses the aero-ramp plume in terms of size. However, note that when the jet-to-freestream momentum flux ratio is increased to 2.0, the nondimensional plume area decreases significantly for the physical ramp while it remains approximately the same size for the aero-ramp. That is, the plume produced by the physical ramp does not grow much with increasing $\bar{q}$, whereas the plume produce by the aero-ramp grows significantly. These results suggest that further increases in $\bar{q}$ may lead to a larger plume area with the aero-ramp when compared to the physical ramp.

6.2.5 Mixing Efficiency

The mixing efficiency is defined as that fraction of the least available reactant which would react if the fuel-air mixture were brought to chemical equilibrium without additional local or global mixing (Mao et al.[49]). Thus, in fuel-rich regions, all of the local air is considered mixed, while in fuel-lean regions all of the local fuel is considered mixed. A two-part definition for mixing efficiency is required depending on whether the flow is globally fuel-rich or fuel-lean. In this study of single injectors in a relatively large duct, the flow is globally fuel-lean, and the mixing efficiency is defined as follows.

$$\eta_m \equiv \frac{\dot{m}_{f,mix}}{\dot{m}_{f,tot}} = \frac{\int \alpha_r \rho u \, dA}{\int \alpha \rho u \, dA} \qquad [6.10]$$

where

$$\alpha_r \equiv \begin{cases} \alpha & \alpha \leq \alpha_s \\ \left(\frac{1-\alpha}{1-\alpha_s}\right)\alpha_s & \alpha > \alpha_s \end{cases} \qquad [6.11]$$

and

α	fuel mass fraction
α_s	H_2-air stoichiometric mass fraction
A	plume area
$\dot{m}_{f,mix}$	mixed fuel mass flow rate
$\dot{m}_{f,tot}$	total fuel mass flow rate

So $\eta_m = 0$ corresponds to a perfectly segregated jet, and $\eta_m = 1$ corresponds to a perfectly mixed jet.

Tables 6.10 and 6.11 summarize the mixing efficiencies versus axial distance for the physical ramp and aero-ramp, respectively, operating at $\bar{q} = 1.0$. Table 6.12 shows the mixing efficiency at the last measurement station for both the physical ramp and aero-ramp operating with $\bar{q} = 2.0$.

Table 6.10 Mixing efficiency; physical ramp, $\bar{q} = 1.0$.

x/d_{eff}	η_m
9.7	0.152
14.3	0.272
25.9	0.523
62.8	0.802
83.6	0.884

Table 6.11 Mixing efficiency; aero-ramp, $\overline{q} = 1.0$.

x/d$_{\text{eff}}$	η_{m}
7.2	0.237
11.4	0.252
22.0	0.440
56.0	0.643
75.0	0.701

Table 6.12 Mixing efficiency; aero-ramp and physical ramp, $\overline{q} = 2.0$.

Injector	x/d$_{\text{eff}}$	η_{m}
Physical	79.0	0.741
Aero	73.8	0.651

Figure 6.18 shows the integrated mixing efficiencies versus axial distance for both injectors tested. Fitting a power law to the three downstream points yields predictions for the far-field mixing efficiencies of each injector. The correlations for $x/d_{eff} > 20$ and $\overline{q} = 1.0$ are as follows: for the physical ramp,

$$\eta_m = 0.12(x/d_{eff})^{0.46} \qquad\qquad [6.12]$$

and for the aerodynamic ramp,

$$\eta_m = 0.13(x/d_{eff})^{0.39}. \qquad\qquad [6.13]$$

In the near-field, the mixing efficiency produced by the aero-ramp is superior to that produced by the physical ramp. In the far-field, however, the mixing efficiency produced by the physical ramp prevails. This is consistent with the results of the maximum fuel concentration and fuel plume area measurements. As the maximum concentration goes down and the plume area goes up, the mixing efficiency must necessarily go up. Furthermore, if the maximum fuel concentration is lower and the fuel plume area is larger in one case when compared to another, the mixing efficiency will necessarily be higher.

When $\overline{q}$ was increased to 2.0, the mixing efficiencies were reduced in both cases as shown in Table 6.12 and Figure 6.18. However, the reduction was more severe for the physical ramp. Both injectors rely heavily on streamwise vorticity for mixing enhancement. As stated earlier, the physical ramp

vorticity is reduced with increasing jet momentum, while for the aero-ramp it appears to increase. As a result, further increases in jet momentum will most likely cause the physical ramp to suffer more than the aero-ramp in terms of mixing efficiency.

Finally, note that when $\alpha_{max} \leq \alpha_s$, the mixing efficiency, η_m, equals unity. Thus, the fully-mixed distance, x_{fm}, also corresponds to that distance when then mixing efficiency first reaches unity. The predictions were used to compute the fully-mixed distances. For the physical ramp, $x_{fm} = 100\, d_{eff}$ and for the aero-ramp, $x_{fm} = 187\, d_{eff}$. These distances are comparable, in terms of relative magnitude, to those computed based on the maximum fuel concentration predictions. The fully-mixed distance for the aero-ramp is approximately twice the fully-mixed distance for the physical ramp. Again, bear in mind that the near-field behavior will most certainly dominate flame ignition characteristics, and the reacting flow will most likely alter the "fully-mixed" distance.

6.2.6 Spatial Mixedness

An unmixedness parameter that quantifies mixing rates based on the variance of the concentration distribution was defined by Liscinsky et al.[50] as,

$$U_s = \frac{\alpha_{var}}{\alpha_{eq}(1 - \alpha_{eq})} \qquad [6.14]$$

where,

$$\alpha_{var} = \frac{1}{n}\sum_{i=1}^{n}(\overline{\alpha}_i - \alpha_{eq})^2 \qquad [6.15]$$

$$\alpha_{eq} = \frac{\dot{m}_j}{\dot{m}_j + \dot{m}_\infty} \qquad [6.16]$$

$$\overline{\alpha}_i = \alpha_i \alpha_{eq}\left[\frac{1}{n}\sum_{i=1}^{n}\alpha_i\right]^{-1} \qquad [6.17]$$

A value of zero for U_s corresponds to a perfectly mixed system, and a value of unity corresponds to a perfectly segregated system. The value of this parameter is that it requires fuel concentration measurements only and does not rely on aerothermodynamic measurements. It was originally developed for planar-laser fuel plume imaging. Here, we have chosen to plot $1 - U_s$ so as to be consistent

with the information provided by the plume area and mixing efficiency (i.e. a larger value indicates better mixing).

Tables 6.13 and 6.14 summarize the spatial mixedness results versus axial distance for the physical ramp and aero-ramp, respectively, operating at $\bar{q} = 1.0$. Table 6.15 shows the spatial mixedness at the last measurement station for both the physical ramp and aero-ramp operating with $\bar{q} = 2.0$.

Table 6.13   Spatial mixedness; physical ramp, $\bar{q} = 1.0$.

x/d_{eff}	$1 - U_s$
9.7	0.822
14.3	0.884
25.9	0.962
62.8	0.982
83.6	0.986

Table 6.14   Spatial mixedness; aero-ramp, $\bar{q} = 1.0$.

x/d_{eff}	$1 - U_s$
7.2	0.872
11.4	0.878
22.0	0.935
56.0	0.956
75.0	0.969

Table 6.15   Spatial mixedness; aero-ramp and physical ramp, $\bar{q} = 2.0$.

Injector	x/d_{eff}	$1 - U_s$
Physical	79.0	0.976
Aero	73.8	0.970

Figure 6.19 shows the computed spatial mixedness $(1 - U_s)$ versus axial distance along with the correlations for both injectors tested. The correlations for $x/d_{eff} > 20$ and $\bar{q} = 1.0$ are as follows: for the physical ramp,

$$1 - U_s = 0.90(x/d_{eff})^{0.022} \qquad\qquad [6.18]$$

and for the aerodynamic ramp,

$$1 - U_s = 0.86(x/d_{eff})^{0.028}. \qquad\qquad [6.19]$$

The fully mixed distances ($U_s = 0$) based on the predictions are $x_{fm} = 120 \, d_{eff}$ for the physical ramp and $x_{fm} = 218 \, d_{eff}$ for the aero-ramp. Again, the distances are comparable to those previously computed using the maximum concentration and mixing efficiency predictions.

When $\overline{q}$ was increased to 2.0, the spatial mixedness decreased with the physical ramp while it slightly increased for the aero-ramp, yet again indicating better mixing performance with increasing $\overline{q}$ for the aero-ramp.

6.2.7 Total Pressure Losses

Figure 6.20 shows the profiles of total pressure at each of the five stations sampled for the physical ramp injector operating with a jet-to-freestream momentum flux ratio of $\overline{q} = 1.0$. In each of the plots shown, the contour color-scales are consistent, so that plot-to-plot comparisons may easily be made. At $x/d_{eff} = 9.7$, the effects of the ramp and jet are clearly visible in the plot. Three local minima occur corresponding to the two vortex cores and the jet. The local minimum of total pressure occurring in the jet results from shock losses through the Mach disk. The outer minima clearly identify the location of the two vortices where the apparent reduction in total pressure results from a transfer of axial kinetic energy to the transverse directions. Note that the ramp shock is not apparent in this plot, since it was above the vertical extent of measurement. However, the lip shock can be identified just above the fuel-vortex structure. At $x/d_{eff} = 14.3$, the losses in the jet core have been distributed over a larger area encompassing the plume and a certain amount of pressure recovery has been realized. The vortices have retained their strength and position as indicated by the total pressure. The recompression shock downstream of the lip shock can be identified over the fuel-vortex structure. The resolution of this shock results from an undesirable interaction with the cone-static pressure probe leading to slight inaccuracies over the range of impingement. This is why the shock appears as a wide band rather than a discrete step. At $x/d_{eff} = 25.9$, the vortex structures have convected upwards carrying the plume with them. At $x/d_{eff} = 62.8$, the losses are

less concentrated indicating a dissipation of the streamwise vorticity. At $x/d_{eff} = 83.6$, the profile is similar to the previous plot with smaller gradients and a larger distribution of losses.

Figure 6.21 shows the profiles of total pressure at each of the five stations sampled for the aero-ramp injector operating with a jet-to-freestream momentum flux ratio of $\bar{q} = 1.0$. The contour color-scales are consistent between plots. At $x/d_{eff} = 7.2$, the losses are confined to the boundary layer very near the wall surface. The aero-ramp does not appear to separate the boundary layer – at least not to the same extent as was observed with the physical ramp. This will most certainly contribute less drag and minimize the occurrence of "hot spots" in the scramjet combustor. The center jet imparts added total pressure to the boundary layer as indicated by the small local maximum just above the wall at $y/d_{eff} = 0$. The three composite shock patterns forming over each of the three rows of jets can be identified. As explained earlier, the resolution of these shocks results from an undesirable interaction between the jet shock and the cone-static pressure probe shock. Thus, it is an effect of the jet shocks which appears in the plots and not the measurement of a true pressure difference. The actual shock locations are at the lower edge of these bands where the jet shock first impinges on the cone-static pressure probe. At $x/d_{eff} = 11.4$, where the three jets have now merged to form one single core of helium, the total pressure losses are larger and cover a larger area. The three composite jet interaction shocks can still be identified as they have moved upward with axial distance. At $x/d_{eff} = 22.0$, some of the total pressure has been recovered within the helium core as the losses have been distributed over a larger region. At $x/d_{eff} = 56.0$, the jet plume finally emerges from the boundary layer as a secondary boundary layer is developing near the wall surface. At $x/d_{eff} = 75.0$, the gradients have become less severe and the pressure losses are distributed over a greater area. Note that no strong vortex patterns persist downstream of the first station. Hence, the mixing downstream of the first station is not dominated by large scale vorticity as is the case for the physical ramp.

Figure 6.22 shows the profiles of total pressure at the fifth station sampled for both the physical ramp and aerodynamic ramp injectors operating with a jet-to-freestream momentum flux ratio of

$\bar{q} = 2.0$. For the physical ramp, the added jet momentum tends to lessen the vorticity generated by the ramp. This is evidenced by the contours where only a single core exists and the gradients are less severe. Of course, the added jet momentum will also tend to alleviate the losses associated with flow separation and add to the total pressure sensed downstream. For the aerodynamic ramp, note that while the pressure losses are distributed over a greater area, the magnitude of the losses have been lessened by the added jet momentum. In comparing the aerodynamic ramp to the physical ramp, the magnitude of the losses are less severe and they do not spread out over as large of an area.

6.2.8 Total Pressure Loss Parameter

The total pressure losses due to fuel injection can seriously affect the thermodynamic efficiency of a scramjet engine. Therefore, the evaluation of a given injector must include some quantification of losses. The total pressure of the incoming air is reduced by viscous forces in the boundary layer, shock waves, flow separation, and fuel-air mixing. Unfortunately, these losses are often very difficult to assess in the cold-flow situation. Previous studies conducted by Fuller et al.[9] and Mays et al.[51] have defined quantitative measures for such assessments. In each case, losses were quantified by examining the mass-weighted field values of the total pressure normalized by the freestream conditions. However, the area over which the integration takes place is often facility dependent or based on a complex analysis of data not readily available. In order to simplify these measures, an adaptation of those previously defined forms was developed here. A new total pressure loss parameter was defined as follows:

$$\Pi = \frac{\int \rho u (P_{t,\infty} - P_t) dA}{\rho_\infty u_\infty P_{t,\infty} A_s + \rho_j u_j P_{t,j} A_j} \qquad [6.20]$$

where

$$A_s = \frac{\lambda}{\alpha_s} A_j \qquad [6.21]$$

That is, A_s is the area required for a uniformly stoichiometric jet given the jet-to-freestream mass flux ratio and jet exit area at the freestream pressure. A parameter value of $\Pi = 0$ indicates no

losses. However, the total pressure parameter is essentially unbounded and a value of unity does not indicate total loss. A larger value of Π does indicate larger losses.

Tables 6.16 and 6.17 summarize the total pressure loss parameter versus axial distance for the physical ramp and aero-ramp, respectively, operating at $\bar{q} = 1.0$. Table 6.18 shows the total pressure loss parameter at the last measurement station for both the physical ramp and aero-ramp operating with $\bar{q} = 2.0$.

Table 6.16   Total pressure loss parameter; physical ramp, $\bar{q} = 1.0$.

x/d_{eff}	Π
9.7	0.127
14.3	0.137
25.9	0.180
62.8	0.325
83.6	0.384

Table 6.17   Total pressure loss parameter; aero-ramp, $\bar{q} = 1.0$.

x/d_{eff}	Π
7.2	0.113
11.4	0.111
22.0	0.136
56.0	0.230
75.0	0.265

Table 6.18   Total pressure loss parameter; aero-ramp and physical ramp, $\bar{q} = 2.0$.

Injector	x/d_{eff}	Π
Physical	79.0	0.221
Aero	73.8	0.167

The computed total pressure parameter versus axial distance for each injector is plotted in Figure 6.23. Again, power-law curve fits have been constructed using the last three data points. The correlations for $x/d_{eff} > 20$ and $\bar{q} = 1.0$ are as follows: for the physical ramp,

$$\Pi = 0.022(x/d_{eff})^{0.65} \qquad [6.22]$$

and for the aerodynamic ramp,

$$\Pi = 0.025(x/d_{eff})^{0.55}. \qquad [6.23]$$

The pressure loss incurred with the physical ramp injector is more severe than that exhibited by the aero-ramp injector for both cases of $\bar{q} = 1.0$ and $\bar{q} = 2.0$. Note that when $\bar{q}$ is increased from 1.0 to 2.0 there is a reduction in total pressure loss parameter as was indicated in the total pressure contours. These reductions result from the added momentum in the freestream direction. Furthermore, the reduction in the case of the physical ramp is greater. This should be expected, since a much greater part of the jet momentum is directed into the freestream.

6.2.9   Mach Number and Velocity Contours

Figures 6.24 and 6.25 show the profiles of Mach number and velocity, respectively, at each of the five stations sampled for the physical ramp injector operating with a jet-to-freestream momentum flux ratio of $\bar{q} = 1.0$. In each of the plots shown, the contour color-scales are consistent so that plot-to-plot comparisons may easily be made. Contour level limits were chosen so as to preserve dynamic range across all plots. In some cases, the minimum and maximum values are truncated. This was carefully done so as not to lose any important features. At $x/d_{eff} = 9.7$, the Mach number is very near the freestream value between $z/d_{eff} = 3$ and 5 as indicated by the bright red contour. Again, the shock at the extreme upper edge of the plot is only visible due to an undesirable interaction with the cone-static pressure probe. In the wake of the physical ramp injector, the Mach number is near unity in and around the jet and vortex cores. The minimum Mach number is actually subsonic with a value of approximately 0.7 at the center of the right vortex core. The helium jet expands to a high velocity within the barrel shock with a maximum value of $u/u_\infty = 2.4$. Across the helium jet, the Mach number is much less than the freestream value of 2.0, while the velocity is much greater than the freestream value. This is a result of the large change in sound speed across the jet. Recall that the sound speed for a perfect gas mixture is a function of the gas composition and temperature (i.e. $a = \sqrt{\gamma R T}$). For a given temperature, the helium-to-air sound speed ratio is approximately 2.9 for pure compositions. This clearly explains the dramatic visual differences between the Mach number and velocity contours within the jet plume. At $x/d_{eff} = 14.3$, the Mach number contours

are very similar to the total pressure contours with low, near-sonic values in the jet with a minimum value of 0.7 in the vortex cores. The velocity contours, however, are quite different and provide some interesting information. The counter-rotating vortices are clearly indicated by the low-speed regions near the wall on either side of the centerline. The high speed fuel-air mixture has been pushed away from the wall through the upward motion induced at the centerline by these counter-rotating vortices. It has also been stretched across the spanwise direction on top of the vortices. Note that the boundary layer is very thin in these plots. Further downstream, the Mach number contours continue to provide essentially the same information as the total pressure contours with the minimum occurring in each of the vortex cores. As the jet influence spreads, the Mach number recovers somewhat with a minimum of about 1.5 in the plume. Note that the wall boundary layer has reformed and is growing quickly with downstream distance. The velocity profile in the far field is quite uniform outside the boundary layer. This is important, since non-uniform velocity profiles can seriously affect nozzle performance downstream of the scramjet combustor.

Figures 6.26 and 6.27 show the profiles of Mach number and velocity, respectively, at each of the five stations sampled for the aero-ramp injector operating with a jet-to-freestream momentum flux ratio of $\bar{q} = 1.0$. At $x/d_{eff} = 7.21$, the maximum Mach number is near that of the freestream while the minimum Mach number is 0.97. This much higher than the minimum Mach number of 0.7 suffered by the physical ramp at the same location. The maximum velocity was found in the center jet core with a value of $u/u_\infty = 1.9$. At $x/d_{eff} = 11.4$, the high-speed region does not correlate with the helium concentration across the entire plume. Rather, the high-speed region correlates with injectant concentration only at the upper edge of the fuel plume outside the momentum boundary layer. The point of maximum velocity is presumably where the three downstream jets impinge and form a single jet structure. Below this impingement point, there is a pocket of low-speed fluid in the wake of the centerline jet. On either side of this pocket of low-speed fluid there are "wings" of high-speed fluid which are presumably the effects of the outer jets in the first row which have no inward yaw angle. Further downstream, the Mach number contours continue to provide the same

information as the total pressure contours. As the jet influence spreads, the Mach number shows some recovery outside the boundary layer. The velocity contours at $x/d_{eff} = 22.0$ indicate that the wall boundary layer was stripped away further upstream. Further downstream, the wall boundary layer quickly redevelops and the velocity profile becomes very uniform outside the boundary layer.

Figures 6.28 and 6.29 show the profiles of Mach number and velocity, respectively, at the farthest downstream location for each injector operating with a jet-to-freestream momentum flux ratio of $\bar{q} = 2.0$. The extent of influence on Mach number is greater for the physical ramp than for the aero-ramp. Overall, the Mach numbers are higher for the aero-ramp, and the profile is slightly more uniform. In each case, the minimum Mach number occurs in the wall boundary layer and is 1.13. The maximum Mach numbers are also essentially the same with a value of 1.94 for the physical ramp and a value of 1.96 for the aero-ramp. In each case, the velocity profiles are very uniform outside the wall boundary layer. The velocity profile for the physical ramp is slightly more uniform. Again, this is important to nozzle performance downstream of the scramjet combustor.

6.2.10 Static Properties

Figures 6.30 through 6.38 show contours of the static pressure, density, and temperature for each injector at each of the 5 stations sampled for each case tested. Much of the same information shown in the previous contours are also conveyed in these contours. However, one can note the strong asymmetries in the static pressure contours. These asymmetries are presumed to be the effects of probe angularity and/or probe/strut interference. These asymmetries are strongest in the near field and dampen out quickly in the far field. If there was some probe angularity in the spanwise direction, there would be some preferential error depending on what side of the jet the probe resided. Furthermore, since the cone-static pressure probe suffers most severely in the presence of shock interference, probe angularity would cause different effects on either side of the ramp. It is highly suspected, that the *true* static pressure field does not exhibit such asymmetries. Furthermore, the errors most likely result from problems with the cone-static pressure probe. The other reduced

variables do not exhibit these asymmetries as they are governed more strongly by the Pitot pressure and total temperature measurements. Had these asymmetries in the static pressure truly existed, one would most certainly observe them in the other variables.

The density contours closely resemble the helium mass fraction contours. This is as one should expect, since, in the absence of shock waves, the mass density in a plane orthogonal to the direction of a quasi-one-dimensional flow should be a function of the gas composition. Any differences between the two results from three-dimensionalities created upstream (i.e. vortices). As these three-dimensionalities dampen out with downstream distance, the appearance of the density and helium mass fraction contours become more and more similar.

The temperature contours closely resemble the Mach number contours. In the combusting case, temperature profiles become important to nozzle performance. It is desirable to have a uniform temperature distribution across the entire flow exiting the combustor. However, this is meaningless in the case of cold-flow studies, since combustion will certainly drastically alter these contours. In the cold-flow case, it is more important to examine fuel mass fraction uniformity across the combustor exit. The heat release due to fuel-air combustion will determine the temperature profile. Therefore, a uniform fuel-air mixture should provide a uniform temperature profile.

6.2.11   Integrated Mass Flow Rate

As a check on the measurement accuracy, an integration of the helium mass flow rates across each of the planes was performed. The field integrated mass flow rates were compared to the measured injector flow rates to determine the amount of helium recovery at each plane. The *helium recovery factor* is defined as follows

$$He_r = \frac{1}{\dot{m}_j} \int_\infty \alpha_{He} \rho u \, dA \qquad [6.24]$$

so that a value of unity indicates full helium recovery. Tables 6.19 and 6.20 summarize the helium recovery factors at each of the planes sampled for the physical ramp and aero-ramp, respectively, operating at $\bar{q} = 1.0$.

Table 6.19   Helium recovery factor; physical ramp, $\bar{q} = 1.0$.

x/d_{eff}	He_r
9.7	1.42
14.3	1.13
25.9	1.30
62.8	1.43
83.6	1.48

Table 6.20   Helium recovery factor; aero-ramp, $\bar{q} = 1.0$.

x/d_{eff}	He_r
7.2	0.95
11.4	1.06
22.0	1.08
56.0	0.80
75.0	1.01

The above results do take into account the injector discharge coefficients. While the helium recovery for the aerodynamic ramp faired quite well, the recovery for the physical ramp was in significant error. The source of these errors are the very large gradients and high three-dimensionality of the flow downstream of the physical ramp. It is important to bear in mind that these calculations involve the integration of four separate measurements each having errors of their own. The ability to resolve large gradients in the flow depends on the spatial resolution of the measurements. The ability to accurately resolve ρ and u depends heavily on the assumption of a small flow angularity. Note that the helium recovery for the physical ramp is best at $x/d_{eff} = 14.3$ where the bulk of the helium is outside the vortex structures. Finally, the helium recovery of only 80% for the aero-ramp at $x/d_{eff} = 56.0$ results from a suspected missed line of data. By examining the helium mass fraction contours at that location, one will notice the apparent discontinuity in the contours at approximately $z/d_{eff} = 2.6$.

The helium recovery factor at $\bar{q} = 2.0$ for the last station sampled was 1.16 for the physical ramp and 1.10 for the aerodynamic ramp. Here, the helium recovery for the physical ramp has improved since the added jet momentum has destroyed some of the error producing vorticity.

6.3 Fuel Plume Imaging Results

Figures 6.39-6.44 show the results of the fuel plume imaging. Each figure shows, from top to bottom, an instantaneous (10 ns) image, the ensemble-averaged image, and an image of the standard deviation. In the instantaneous and ensemble-averaged images, the intensities values have been inverted so that, high intensity indicates a high helium concentration. In each case, the dynamic range of the intensity resolution was optimized to preserve structural detail, hence the color scales are not consistent between images. In examining these images, one must be careful when comparing them to the gas sampling measurements. The images intensities are proportional to the local particle number density. It will be shown later, that this particle number density is not only a function of the helium concentration but of the local temperature and pressure as well. However, for the most part, the images and the mass fraction contours compare quite well. The following sections analyze each image in detail.

6.3.1 Instantaneous Images

Figure 6.39a at the top shows an instantaneous fuel plume image for the physical ramp operating with $\overline{q} = 1.0$ at $x/d_{eff} = 9.7$. The quality of this image is poor due to strong reflections off the base of the physical ramp injector. These reflections distort the image and raise the background noise levels. The fuel jet is indicated by the red and yellow regions which are interrupted by the blue region produced by reflections off the ramp. In any event, the periphery on the right side of the jet is quite clear. The eddies along the fuel-air interface may be observed. This indicates that the 10-ns exposure time was sufficient to effectively "freeze" the turbulent action. By examining the upper edge of the right side of the plume, the effect of the vortex stripping fluid away from the plume may be observed. The vortices are located about midway between the wall surface and the upper edge of the plume on either side of the jet. Just above the plume, the curved line delineating the blue and green regions is the effect of the oblique lip shock identified in the shadowgraph images. The shock

wave increases the density downstream and therefore the scattering intensity. Since it is a negative image, the intensity is higher in the less dense region upstream of the shock.

Figure 6.40a at the top shows an instantaneous fuel plume image for the physical ramp operating with $\overline{q} = 1.0$ at $x/d_{eff} = 14.3$. Here, the image quality has improved, however the reflections off the ramp are still present and do tend to raise the background noise levels. The reflection of the ramp can be seen on the left-hand side of the image. Note that the plume is uninterrupted by the ramp reflections. It is quite clear that the vortices have pushed the fuel up and away from the wall at the centerline. The fuel has begun to wrap around the vortices as the air is entrained from the bottom outside corners up through the middle. This dynamic mixing distribution has taken all of the fuel and completely removed it from the wake of the ramp. The area which contained all the fuel in the previous image, now contains only air.

Figure 6.41a at the top shows an instantaneous fuel plume image for the physical ramp operating with $\overline{q} = 1.0$ at $x/d_{eff} = 25.9$. The plume has spread to cover a much larger area. The strong effects of the air entertainment at the bottom of the jet up through the middle are still quite obvious. The air is sucked in at the bottom and surges all the way up through the plume and disperses at the top. This results in the low concentrations at the top of the plume. The spatial concentration fluctuations across the plume have increased. This is the effect of small-scale mixing mechanisms taking over as the large-scale counter-rotating vortices lose their strength.

Figure 6.42a at the top shows an instantaneous fuel plume image for the aerodynamic ramp operating with $\overline{q} = 1.0$ at $x/d_{eff} = 7.21$. Unlike for the physical ramp, the image for the aero-ramp exhibits large spatial fluctuations in the near field. This contributes to the large degree of mixing observed with the probing measurements. Each of three jets in the final row of the aero-ramp can be identified. These jets show less spatial fluctuation than does the entire field over which they are superimposed. As a result of the complex nature of the flow pattern and the large degree of initial mixing, the periphery of the composite plume is not well defined. This behavior will most certainly cause early ignition in the combusting case. Finally, notice that the shock wave forming over the

third row of jets is clearly defined, smooth and extends over the entire span of the image. This indicates that the jets appear as a single bluff body to the oncoming flow as opposed to discreet disturbances. While the shock is clearly observed, the density change across it is not enough to cause a significant change in the scattering intensity. This is consistent with the probing where the shock was perceptible due to probe interference but not strong enough to cause a significant increase in the density.

Figure 6.43a at the top shows an instantaneous fuel plume image for the aerodynamic ramp operating with $\overline{q} = 1.0$ at $x/d_{eff} = 11.4$. The plume has spread to cover a large area, and the spatial fluctuations have increased. Notice the two lobes on either side of the bulk of the plume where there exist sparse chunks of fuel. The plume shows a large degree of asymmetry which is a result of large temporal fluctuations. Real-time observation of the plume shows a highly unsteady behavior.

Figure 6.44a at the top shows an instantaneous fuel plume image for the aerodynamic ramp operating with $\overline{q} = 1.0$ at $x/d_{eff} = 22.0$. Again, the plume has spread to cover a larger area, and the spatial fluctuations have increased. The two lobes at the bottom outside edges containing sparse chunks of helium still exist.

6.3.2 Ensemble-Averaged Results

Figure 6.39b in the middle shows the mean image of the fuel plume for the physical ramp operating with $\overline{q} = 1.0$ at $x/d_{eff} = 9.7$. Again, the image quality is poor due to the reflections off the ramp base. Unlike the instantaneous image, this image is smooth, and the eddies have been averaged out. The plume boundary is well defined, and the effects of the vortices are clear. Since the vortices are generated by the ramp geometry, they exist in the response images as well as the signal images. Therefore, the correction process actually removes the vortices from the image. At the center of the vortices, the pressure drops and the seed density goes down. Therefore, the vortex will give the false impression of a non-zero helium concentration if not removed. Since the shock is

produced by the helium jet which is not present in the response image, it will not be removed by the correction process. In all these images, all characteristics are produced by the presence of the helium injection only. Since the reflections off the ramp base were stronger in the response image than in the signal image, they could not be removed. This is an unwanted effect associated with the presence of the helium jet. However, if one visually removes the ramp base, the plume looks very similar to that obtained with the gas sampling probe measurements.

Figure 6.40b in the middle shows the mean image of the fuel plume for the physical ramp operating with $\overline{q} = 1.0$ at $x/d_{eff} = 14.3$. The plume boundaries are smooth and well-defined. The appearance is very much like that of the mass fraction contours obtained with the gas sampling probe. The bulk of the helium lies in the oblong layer riding on top of the two counter-rotating vortices. The vortex cores are centered around the two lobes which extend down below the bulk of the plume. Clearly, the helium has been pushed up away from the wall at the centerline. Furthermore, air is being entrained from the sides near the wall and pushed up through the center of the plume and around the vortices. The fuel-air interface around the vortex just under the bulk of the plume forms a very interesting pattern similar to a large ocean wave crest just before it breaks.

Figure 6.41b in the middle shows the mean image of the fuel plume for the physical ramp operating with $\overline{q} = 1.0$ at $x/d_{eff} = 25.9$. The plume has become more diffuse, and the spatial fluctuations have increased. The plume boundary is not as well defined, particularly at the top where the intensities are the lowest. Note how the air is entrained from the bottom outside corners, surges up through the middle of the plume and then spreads out at the top. The action of the vortices located at the large intensity peaks has essentially caused the plume to split into two halves. Each halve has a kidney shape, and they are separated by the airstream surging up between them. Again, the appearance of the plume is very similar to that obtained with the gas sampling probe.

Figure 6.42b in the middle shows the mean image of the fuel plume for the aerodynamic ramp operating with $\overline{q} = 1.0$ at $x/d_{eff} = 7.21$. The plume boundaries are smooth and well-defined. The core of each of the three jets in the furthest downstream row are clearly observed. The shock

wave forming over the last row of jets is clearly seen. Note that the shock wave is very smooth and rounded. Again, this indicates that the row of jets appear as a single solid bluff body to the incoming main flow. Furthermore, the mean shock band is quite narrow, indicating a very steady shock location.

Figure 6.43b in the middle shows the mean image of the fuel plume for the aerodynamic ramp operating with $\overline{q} = 1.0$ at $x/d_{eff} = 11.4$. The plume boundary is still well defined except at the outside edges where the intensities are very low. It is interesting to note here that, unlike with the gas sampling profile, the high concentrations do not extend all the way down to the wall. This is presumably a result of density differences affecting the scattering intensity.

Figure 6.44b in the middle shows the mean image of the fuel plume for the aerodynamic ramp operating with $\overline{q} = 1.0$ at $x/d_{eff} = 22.0$. The plume has become more diffuse, and the spatial fluctuations have increased. The plume boundary is not as well defined, particularly at the bottom where the intensities are the lowest. The bulk of the plume has lifted away from the wall. Again, unlike with the gas sampling contours, high intensities near the wall are not apparent. We must be careful here not to interchange concentrations with intensities. As will soon be shown, the intensities are not only a function of helium concentration, but they are a function of mass density as well.

6.3.3   Mean Penetration

Defining the absolute penetration of the plume based on the Rayleigh imaging has proved to be difficult. Selecting a specific intensity value as the absolute plume boundary is meaningless, since each of the images have been normalized and rescaled. Hence, to avoid subjectivity, the plume boundary was defined as 5% of the peak intensity. By so doing, the penetration versus axial distance could be determined. Tables 6.21 and 6.22 summarize the penetration heights versus axial distance for the physical ramp and aero-ramp, respectively, operating at $\overline{q} = 1.0$ as determined from the Rayleigh images.

Table 6.21 Penetration height; physical ramp, $\bar{q} = 1.0$.

x/d$_{\text{eff}}$	h/d$_{\text{eff}}$
9.7	1.6
14.3	2.4
25.9	3.6

Table 6.22 Penetration height; aero-ramp, $\bar{q} = 1.0$.

x/d$_{\text{eff}}$	h/d$_{\text{eff}}$
7.2	1.5
11.4	1.9
22.0	2.6

These results are consistent with those obtained from the gas sampling measurements. That is, the penetration of each injector is approximately equal in the very near field. However, the penetration of the physical ramp surpasses the aero-ramp for $\bar{q} = 1.0$. Figure 6.45 shows the plot of penetration height versus axial distance for both injectors operating at a $\bar{q} = 1.0$. The data obtained from the gas sampling has been included for comparison.

6.3.4 Relative Plume Area

The absolute plume area is defined here by that area enclosed by the contour representing 5% of the maximum intensity. The relative plume area is the same as that defined in Section 6.3.4. These definitions were applied to the data obtained in the Rayleigh-imaging experiments, and Tables 6.23 and 6.24 summarize the relative plume areas versus axial distance for the physical ramp and aero-ramp, respectively, operating at $\bar{q} = 1.0$.

Table 6.23 Relative plume area; physical ramp, $\bar{q} = 1.0$.

x/d$_{\text{eff}}$	A
9.7	0.08
14.3	0.24
25.9	0.56

Table 6.24 Relative plume area; aero-ramp, $\bar{q} = 1.0$.

x/d$_{\text{eff}}$	$\bar{\text{A}}$
7.2	0.16
11.4	0.28
22.0	0.35

The results here are consistent with those obtained from the gas sampling measurements. That is, the size of the aero-ramp plume is initially larger than the physical ramp plume. However, the physical ramp plume grows larger than the aero-ramp plume with downstream distance. Figure 6.46 shows the plot of relative plume area versus axial distance for both injectors operating at a $\overline{q} = 1.0$. The data obtained from the gas sampling has been included for comparison.

6.3.5 Standard Deviation Results

Figure 6.39c at the bottom shows the standard deviation image of the fuel plume for the physical ramp operating with $\overline{q} = 1.0$ at $x/d_{eff} = 9.7$. In this case, the reflections off the base of the ramp do not seriously affect the quality of the image. The largest fluctuations are indicated by the red, while the lowest fluctuations are indicated by the blue. The largest fluctuations occur on the periphery of the plume in a very narrow band. Inside the jet, where the potential core still persists, the fluctuations are essentially zero. On the right side of the plume, one will notice the moderate fluctuations around the periphery of the vortex. Note that the fluctuations at the center of the vortex are near zero.

Figure 6.40c at the bottom shows the standard deviation image of the fuel plume for the physical ramp operating with $\overline{q} = 1.0$ at $x/d_{eff} = 14.3$. The highest fluctuations occur in a thin narrow band along the upper edge of the fuel-air interface. Beneath this band, the fluctuations are very low where the helium concentrations are the highest. This is as one should expect, since the fluctuations indicate where the bulk of the mixing is occurring. The fluctuations are near zero across the vortices. While there is certainly a mixture of fuel and air within the vortices, the composition is very steady in time. Finally, there are modest fluctuations occurring between the vortices beneath the bulk of the plume where air is entrained from outside. These are most likely density fluctuations, since the helium concentrations are near zero within that region.

Figure 6.41c at the bottom shows the standard deviation image of the fuel plume for the physical ramp operating with $\overline{q} = 1.0$ at $x/d_{eff} = 25.9$. The fluctuations now occur over the entire spatial

extent of the fuel-air mixture. Furthermore, the fluctuations are relatively uniform across the entire region except on the right side. This uniformity indicates that the bulk mixing is occurring everywhere across the plume. The high intensity region that occurs on the right side of the plume, and not on the left side, is presumably an effect of laser attenuation. The laser comes in from the right-hand side and is attenuated as it passes through the cloud of SiO_2 particles.

Figure 6.42c at the bottom shows the standard deviation image of the fuel plume for the aerodynamic ramp operating with $\overline{q} = 1.0$ at $x/d_{eff} = 7.21$. Unlike the physical ramp plume at the same near-field station, high amplitude fluctuations occur across the entire plume for the aero-ramp. These fluctuations are responsible for the significant mixing observed in the near field. The largest fluctuations occur near the top edge of the plume at the fuel-air interface. There are four small localized regions of low fluctuation near the wall. These are most likely the effects of the vortices generated by the injector flow field. Finally, note that the shock over top of the plume is indicated by a very thin and smooth line. This indicates that the shock is very steady in time.

Figure 6.43c at the bottom shows the standard deviation image of the fuel plume for the aerodynamic ramp operating with $\overline{q} = 1.0$ at $x/d_{eff} = 11.4$. The largest fluctuations now occur only in a thick, well-defined band along the upper edge of the plume at the fuel-air interface. The area over which these fluctuations occur is still larger than that for the physical ramp at the same location. Again, this results in the superior mixing performance of the aero-ramp at that location.

Figure 6.44c at the bottom shows the standard deviation image of the fuel plume for the aerodynamic ramp operating with $\overline{q} = 1.0$ at $x/d_{eff} = 22.0$. The fluctuations are more uniform now, and the appearance of the image is similar to that of the physical ramp. The spatial extent of the fluctuations is smaller than that obtained with the physical ramp. This is the point where the mixing with physical ramp surpasses the aero-ramp. Again, the intensity is higher on the right-hand side than on the left-hand side and is assumed to be an effect of laser attenuation.

6.3.6   Correlation with Probing Data

Recall from Section 4.5.1, that the radiant scattering intensity, I_s, is directly proportional to the particle number density, N_p. If, for the SiO_2 particles in air, we assume a uniform particle number density, uniform particle size, and that the particles accurately track the flow, then the scattering intensity will also be proportional to the air number density. That is,

$$I_s \propto N_{air} \qquad [6.25]$$

The number density of air is simply the moles of air multiplied by Avogadro's number divided by the volume under consideration.

$$N_{air} = \frac{1}{V}\mathcal{N}_{air}\hat{N} \qquad [6.26]$$

So that,

$$I_s \propto \frac{\hat{N}}{V}\mathcal{N}_{air} \qquad [6.27]$$

The mole fraction of helium is given by

$$X_{He} = 1 - X_{air} = 1 - \frac{\mathcal{N}_{air}}{\mathcal{N}} \qquad [6.28]$$

so that

$$\mathcal{N}_{air} = \mathcal{N}(1 - X_{He}) \qquad [6.29]$$

where $\mathcal{N}$ is the total number of moles. Then, substituting in Eq. 6.18 into Eq. 6.16 yields

$$I_s \propto \frac{\hat{N}\mathcal{N}}{V}(1 - X_{He}) \qquad [6.30]$$

For a mixture of perfect gases,

$$pV = \mathcal{N}\hat{R}T \qquad [6.31]$$

where $\hat{R}$ is the universal gas constant. This yields,

$$I_s \propto \frac{\hat{N}}{\hat{R}}\frac{p}{T}(1 - X_{He}) \qquad [6.32]$$

or

$$I_s \propto \frac{p}{kT}(1 - X_{He})$$

[6.33]

where k is the Boltzmann constant, $\hat{R}/\hat{N}$. Then, assuming a constant of proportionality, $1/\beta$, we get

$$I_s = \frac{p}{\beta kT}(1 - X_{He})$$

[6.34]

Hence, relating the scattering intensity directly to helium concentration requires knowledge of the temperature and pressure field.

Figures 6.47 and 6.48 show the contours of $(1 - X_{He})p/\beta kT$ calculated from the probing measurements along with the corresponding scattering intensities. Each have been normalized based on the maximum and minimum values within the respective plot. Comparison of the predicted scattering intensity with the actual scattering intensity was qualitatively good but not as quantitatively good as was hoped. One will notice that, the comparison gets worse with downstream distance. Had the reflections off the base of the physical ramp not been a problem, the comparison at $x/d_{eff} = 9.70$ would have been fairly good. The comparison at $x/d_{eff} = 14.3$ for the physical ramp is perhaps the best of all cases. Note that in all cases, the comparison is poorest near the bottom wall surface. This is due to reflections of the wall surface that could not be removed in the image correction process. As the overall scattering intensities decreased across the plume due to mixing, the effect of wall surface reflections became more significant.
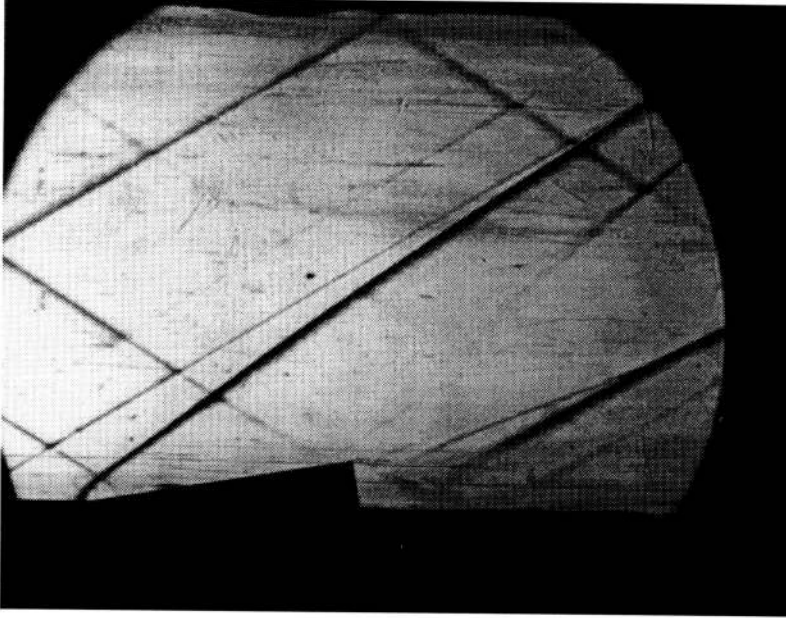
Figure 6.1 Shadowgraph; physical ramp, no injection, $M_\infty = 2.0$.
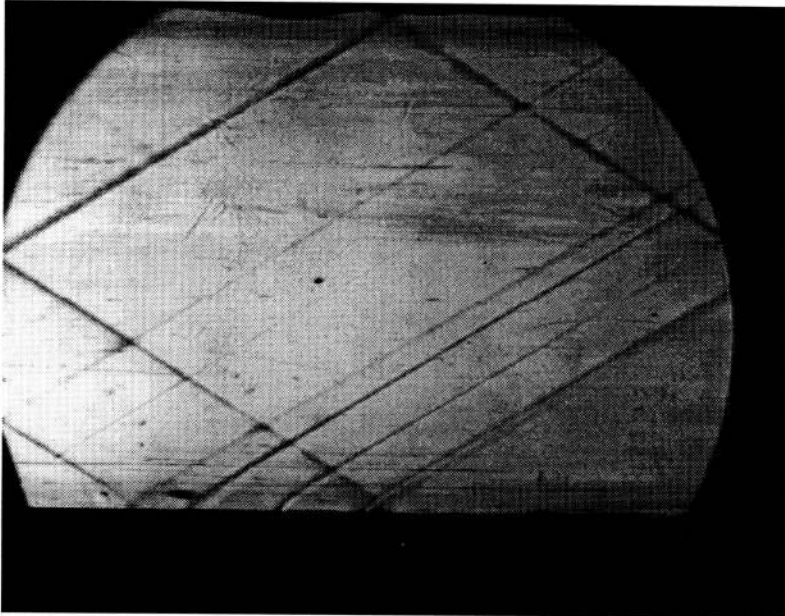
Figure 6.2 Shadowgraph; aero-ramp, no injection, $M_\infty = 2.0$.
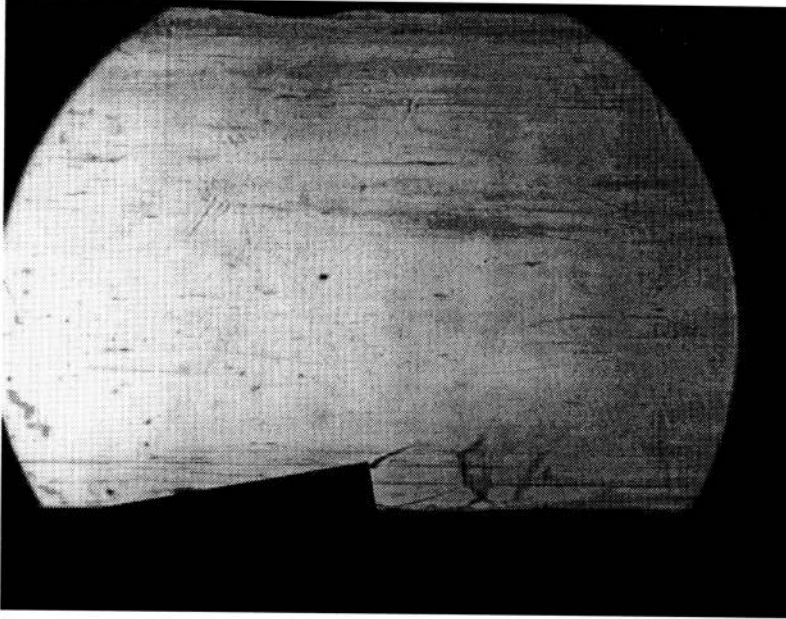
Figure 6.3 Shadowgraph; physical ramp, air injection, no main flow, $P_{t,j} = 300$ kPa.
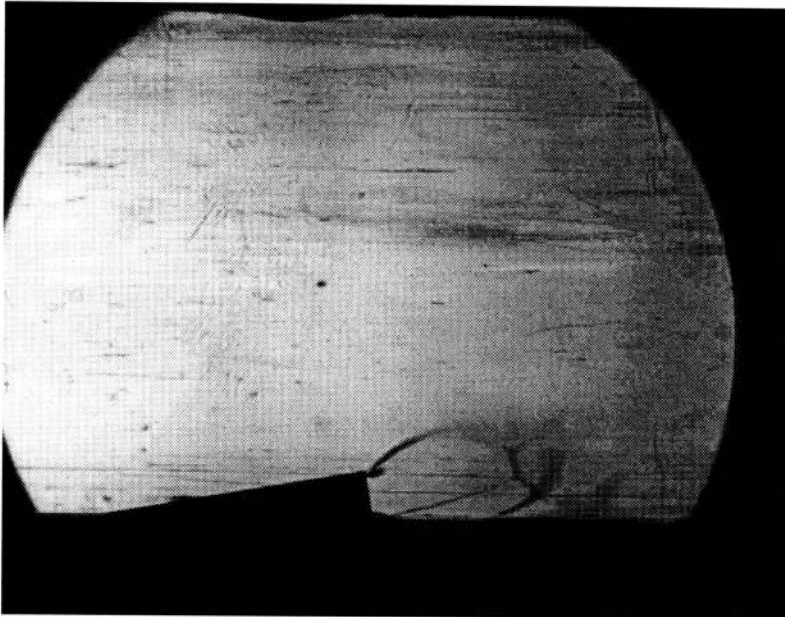
Figure 6.4 Shadowgraph; physical ramp, air injection, no main flow, $P_{t,j} = 601$ kPa.
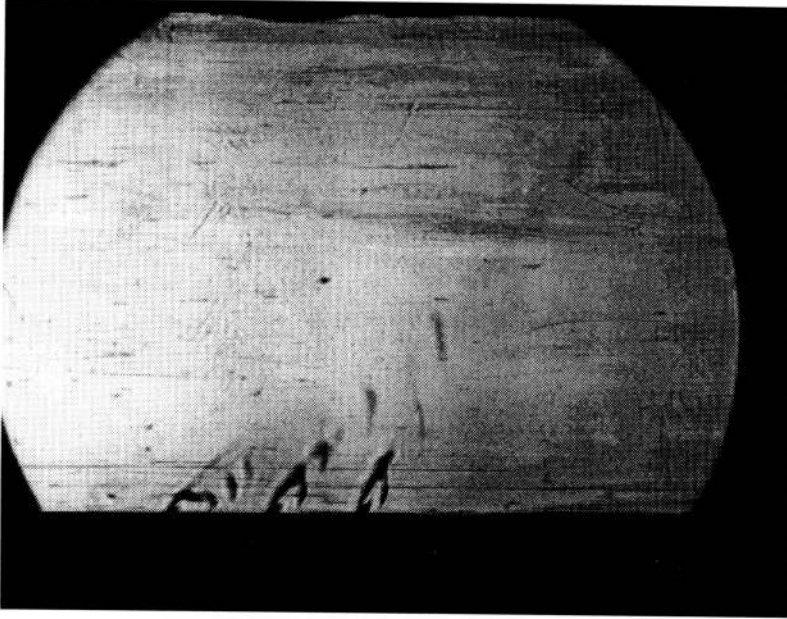
Figure 6.5 Shadowgraph; aero-ramp, air injection, no main flow, $P_{t,j} = 300$ kPa.
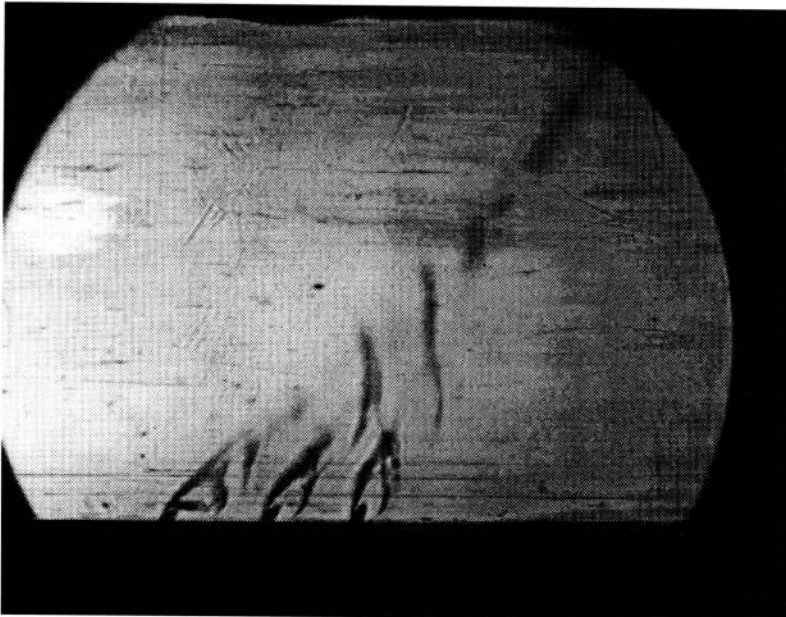
Figure 6.6 Shadowgraph; aero-ramp, air injection, no main flow, $P_{t,j} = 601$ kPa.
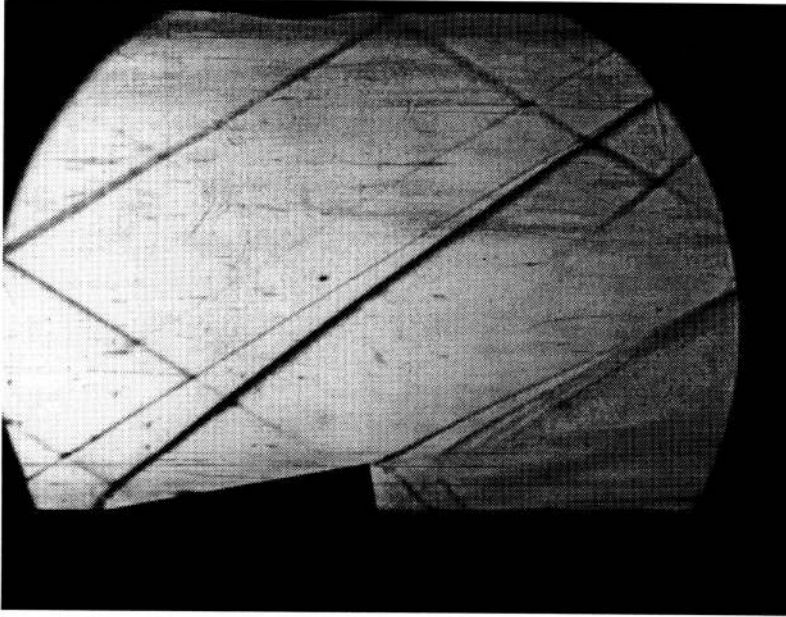
Figure 6.7 Shadowgraph; physical ramp, He injection, $M_\infty = 2.0$, $\overline{q} = 1.0$.
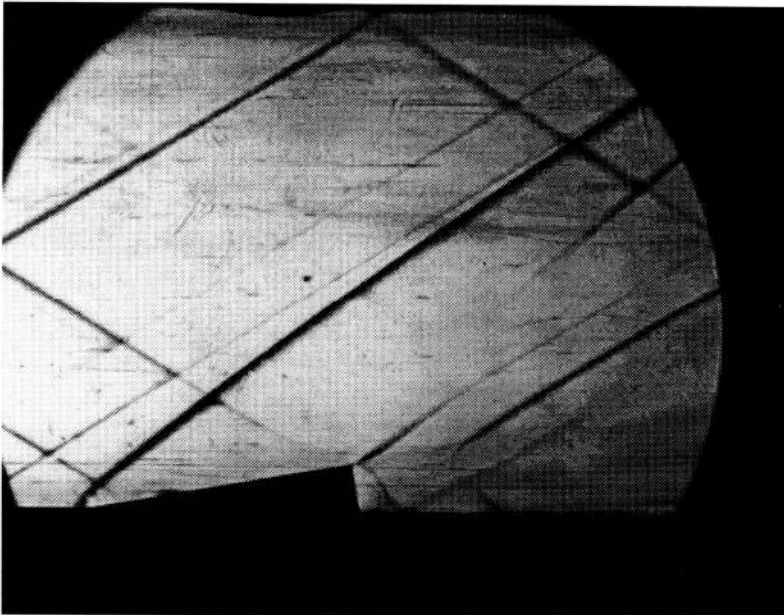
Figure 6.8 Shadowgraph; physical ramp, He injection, $M_\infty = 2.0$, $\overline{q} = 2.0$.
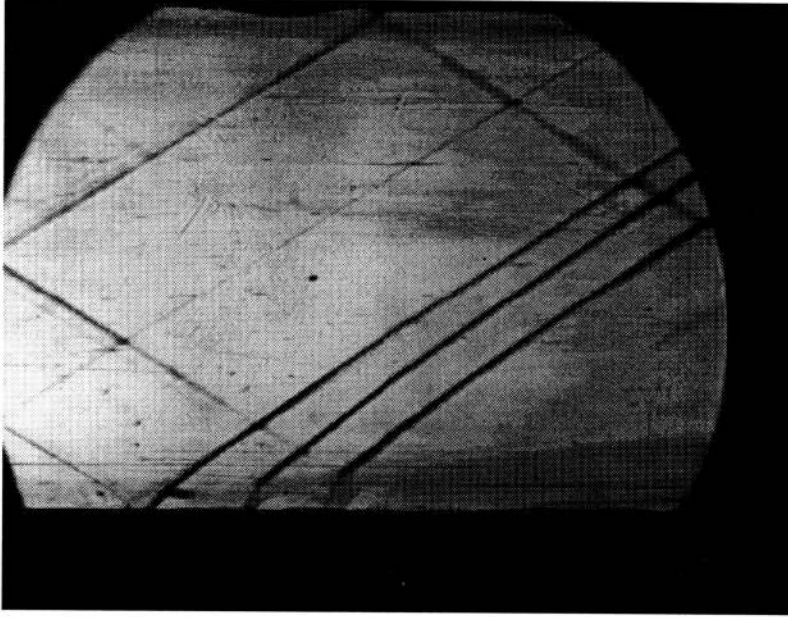
Figure 6.9   Shadowgraph; aero-ramp, He injection, $M_\infty = 2.0$, $\overline{q} = 1.0$.
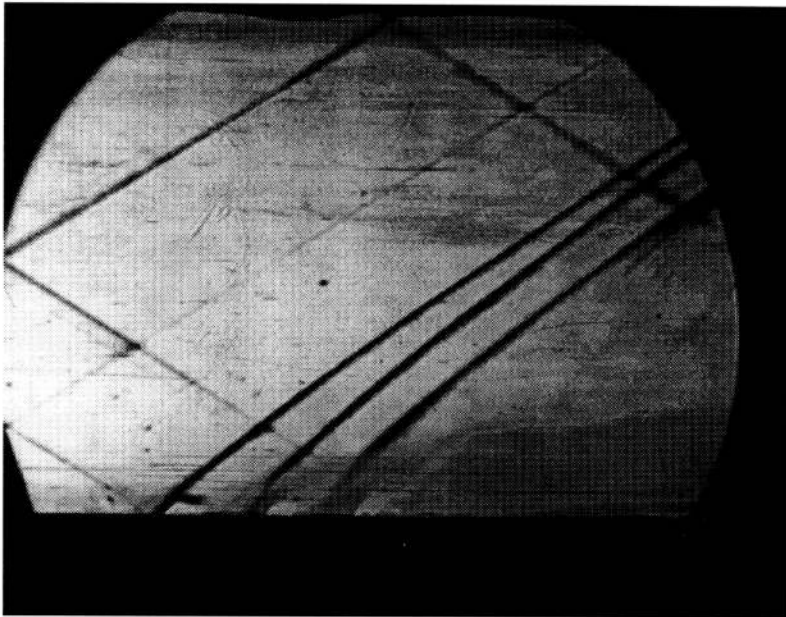
Figure 6.10   Shadowgraph; aero-ramp, He injection, $M_\infty = 2.0$, $\overline{q} = 2.0$.
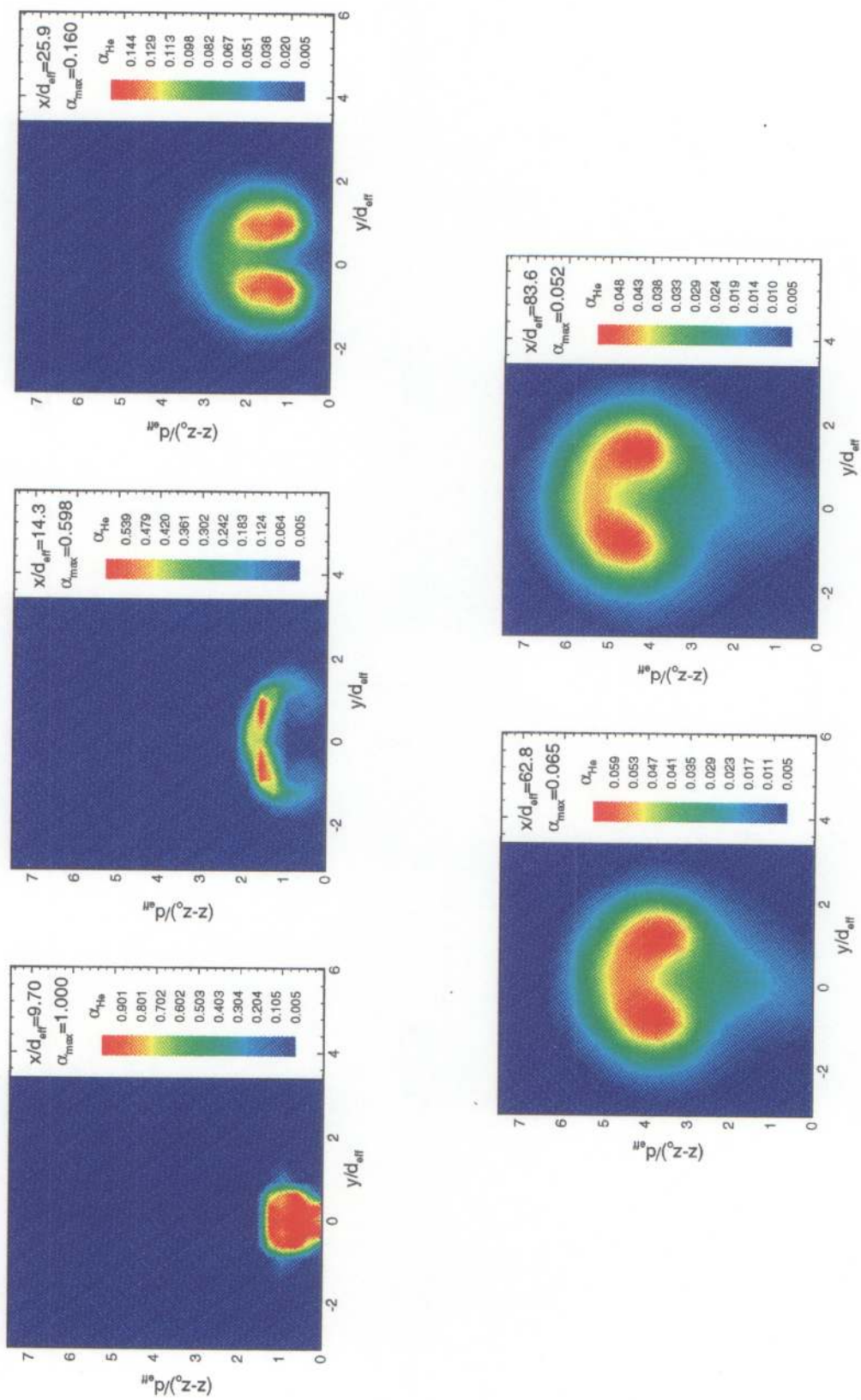
Figure 6.11   Helium mass fraction contours; physical ramp, $\bar{q} = 1.0$
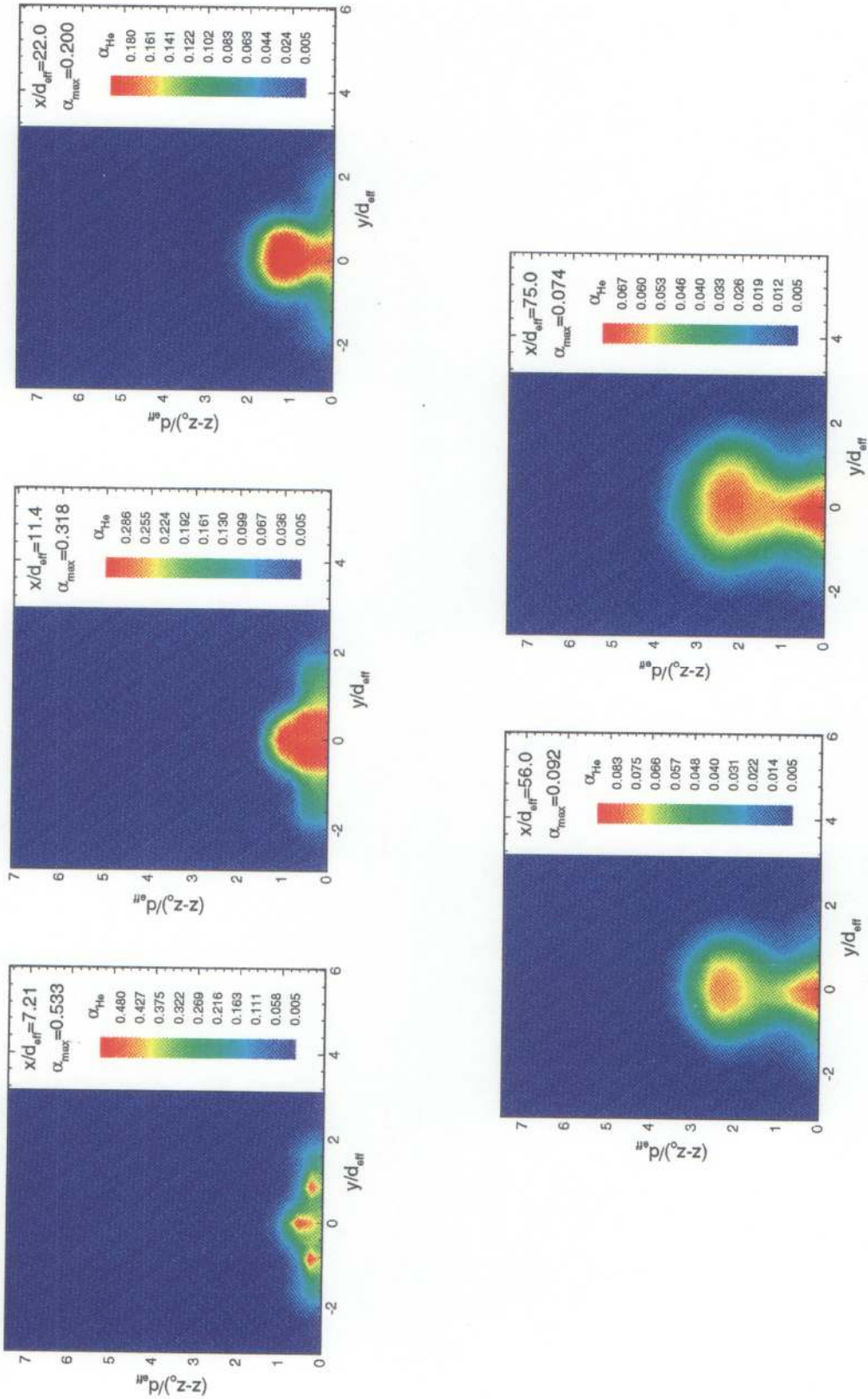
Figure 6.12 Helium mass fraction contours; aero-ramp, $\bar{q} = 1.0$
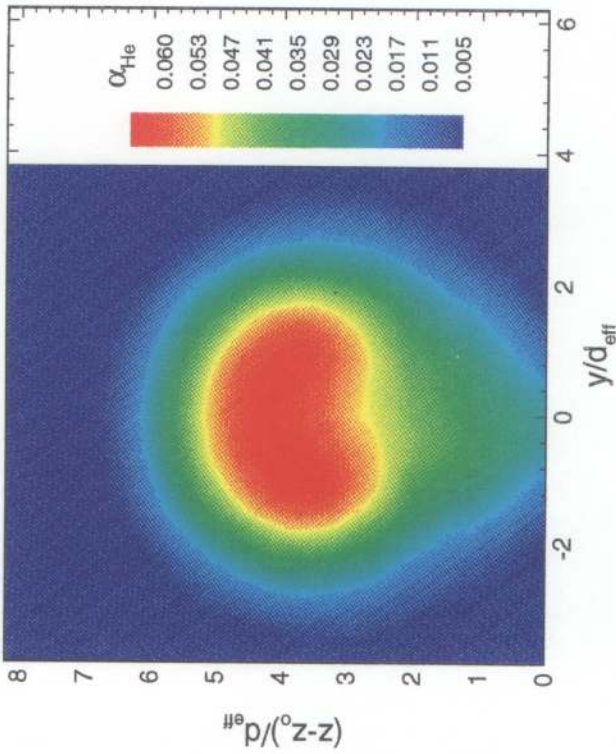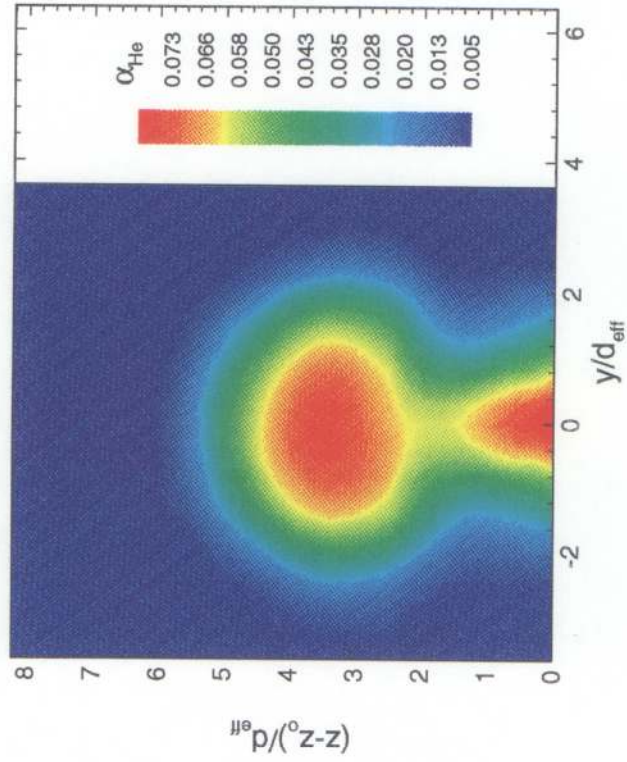
Figure 6.13   Helium mass fraction contours; physical ramp and aero-ramp, $\bar{q} = 2.0$
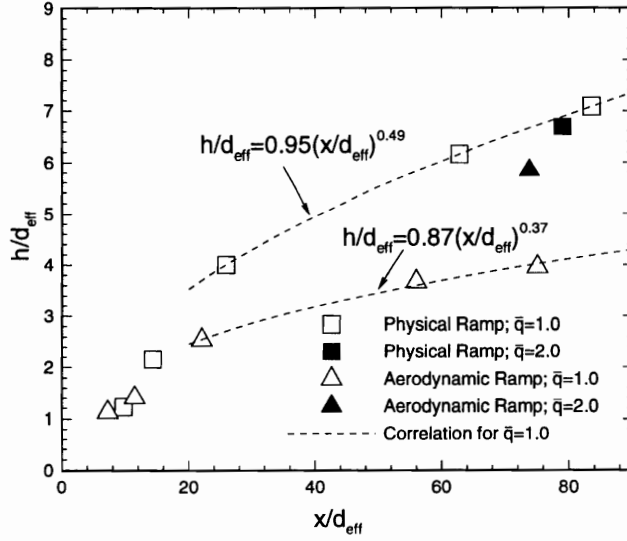
Figure 6.14 Injectant penetration trajectory.
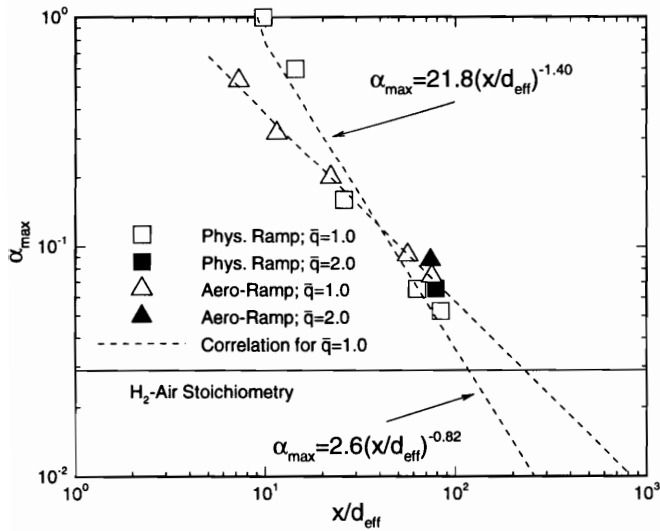
Figure 6.15 Decay of maximum concentration.
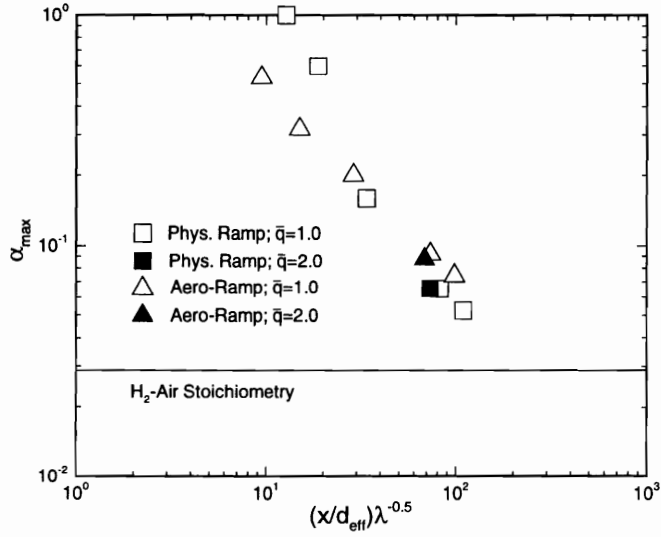
Figure 6.16   Correlated decay of maximum concentration.
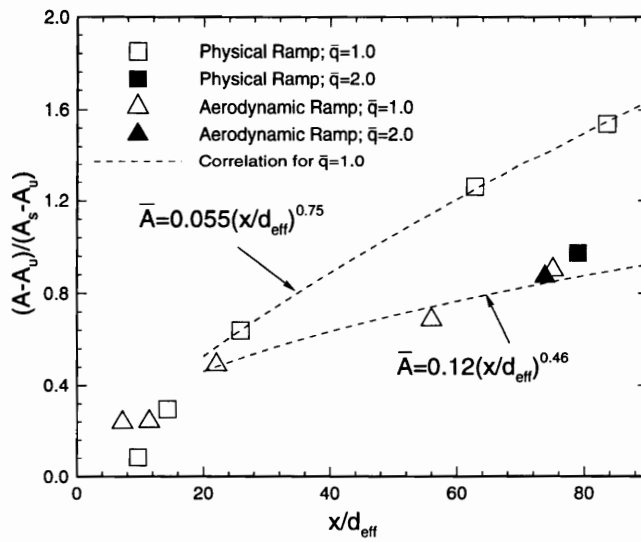
Figure 6.17   Relative plume area.
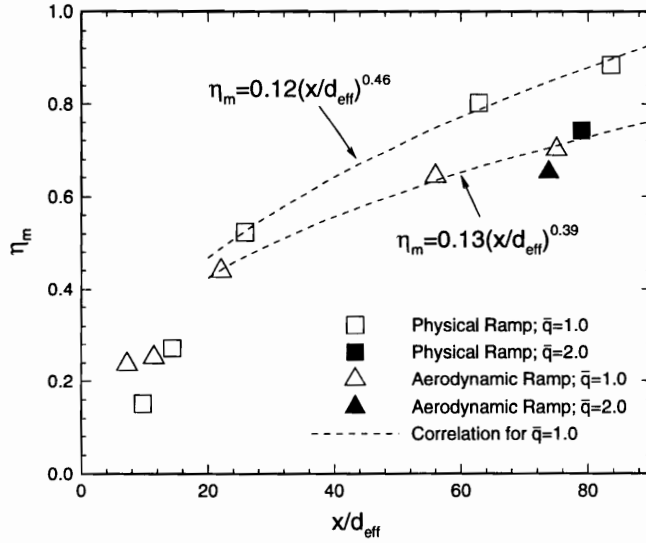
Figure 6.18   Integrated mixing efficiency.
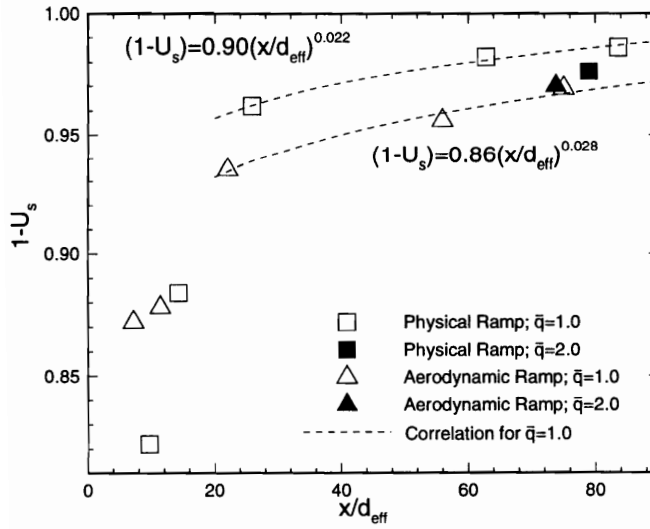
Figure 6.19   Spatial mixedness.
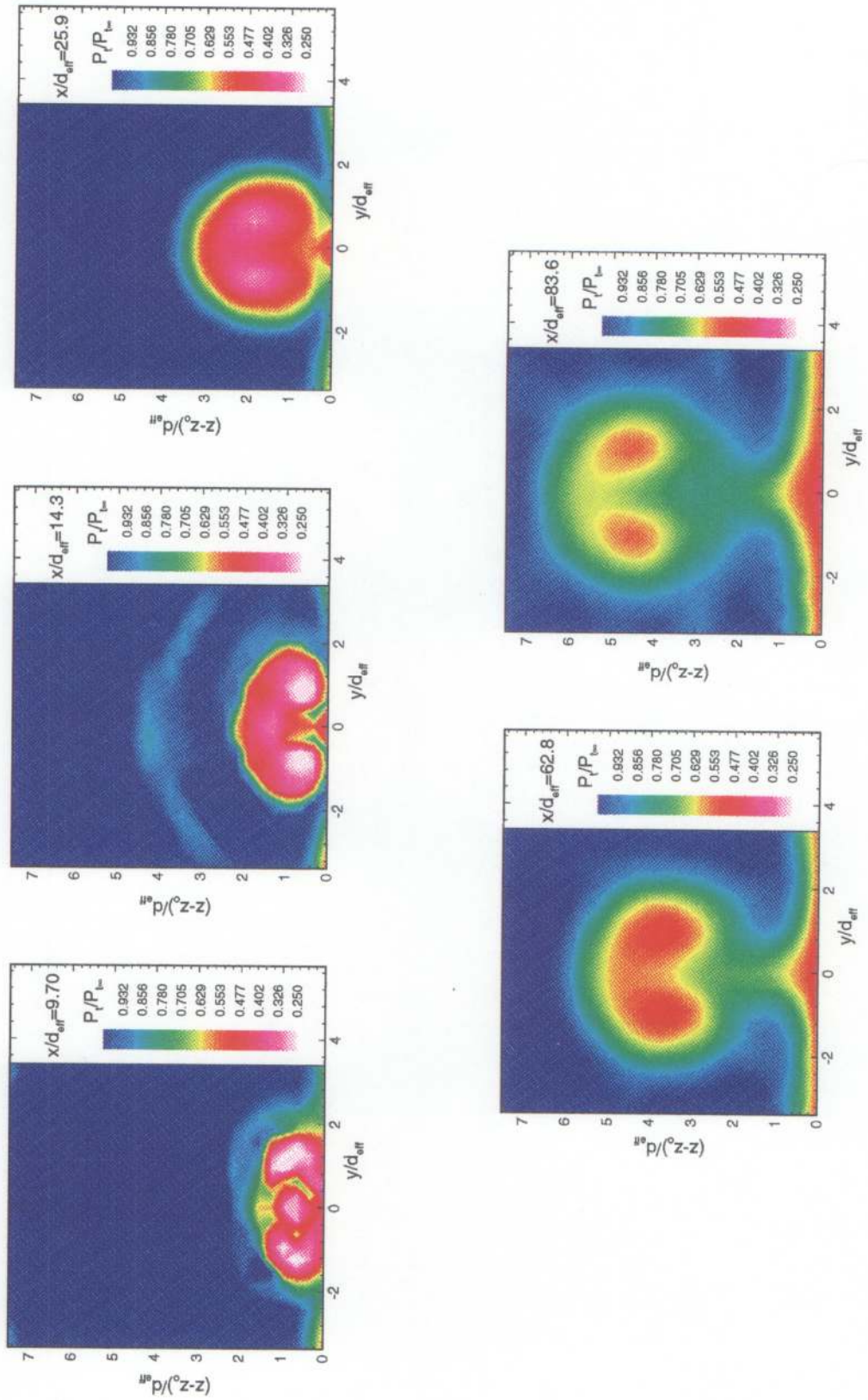
Figure 6.20 Total pressure contours; physical ramp, $\bar{q} = 1.0$.
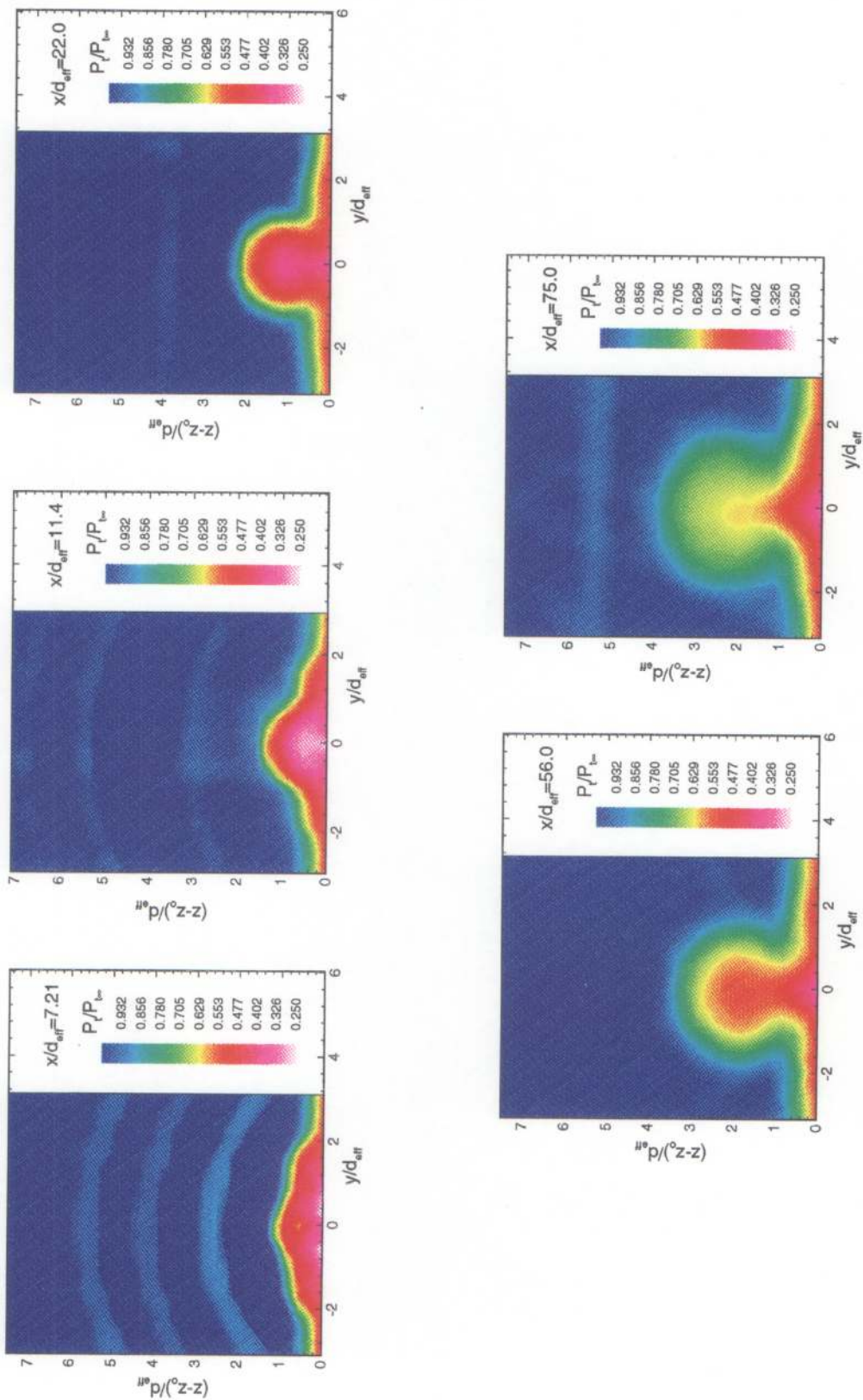
Figure 6.21 Total pressure contours; aero-ramp, $\bar{q} = 1.0$.
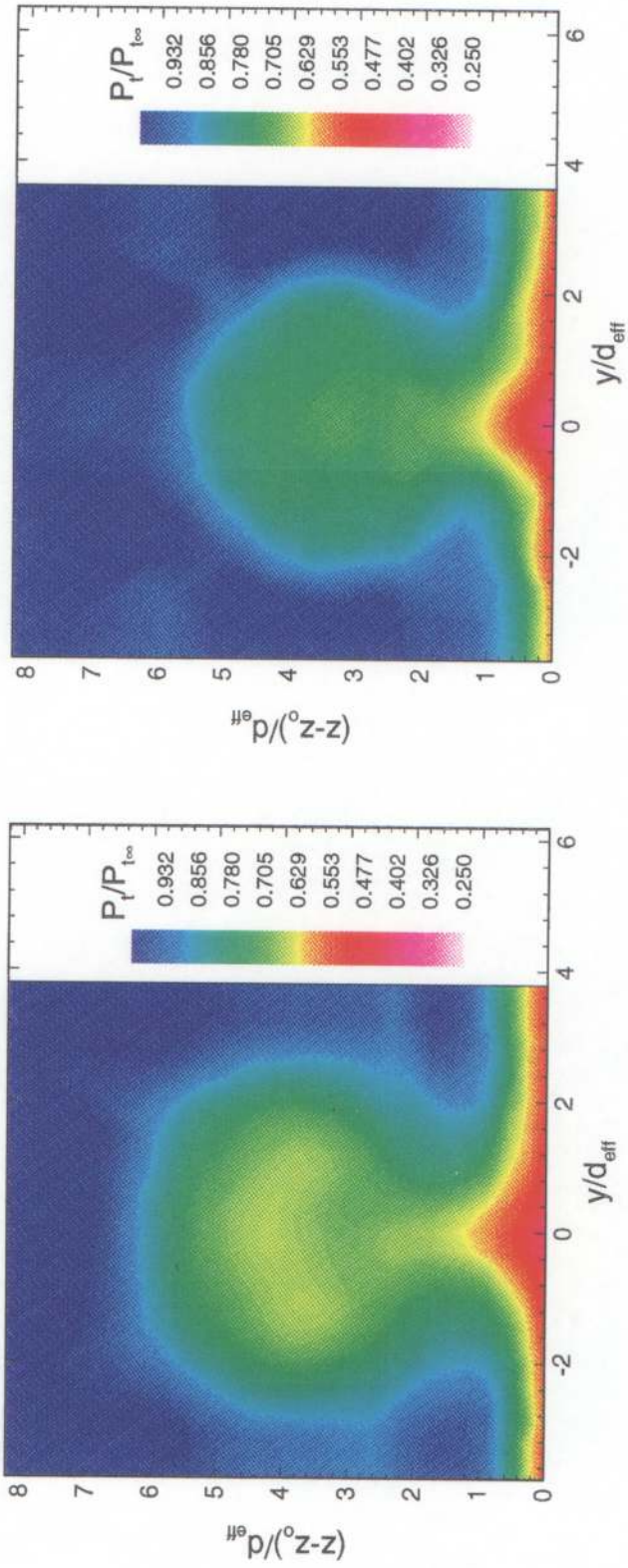
Figure 6.22   Total pressure contours; physical ramp and aero-ramp, $\bar{q} = 2.0$.
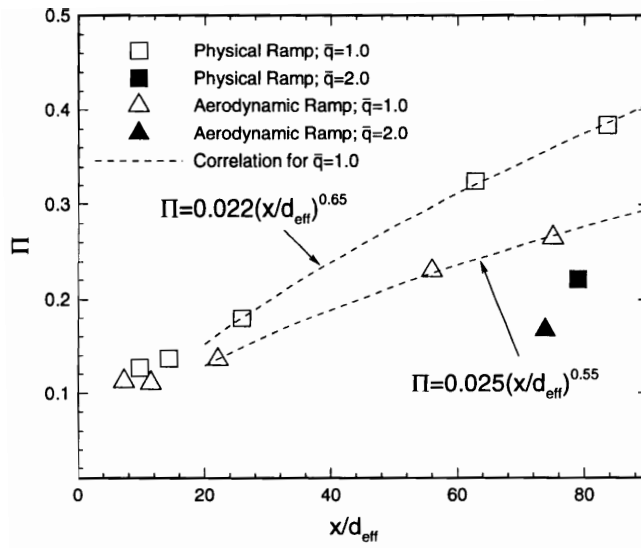
Figure 6.23 Total pressure loss parameter.
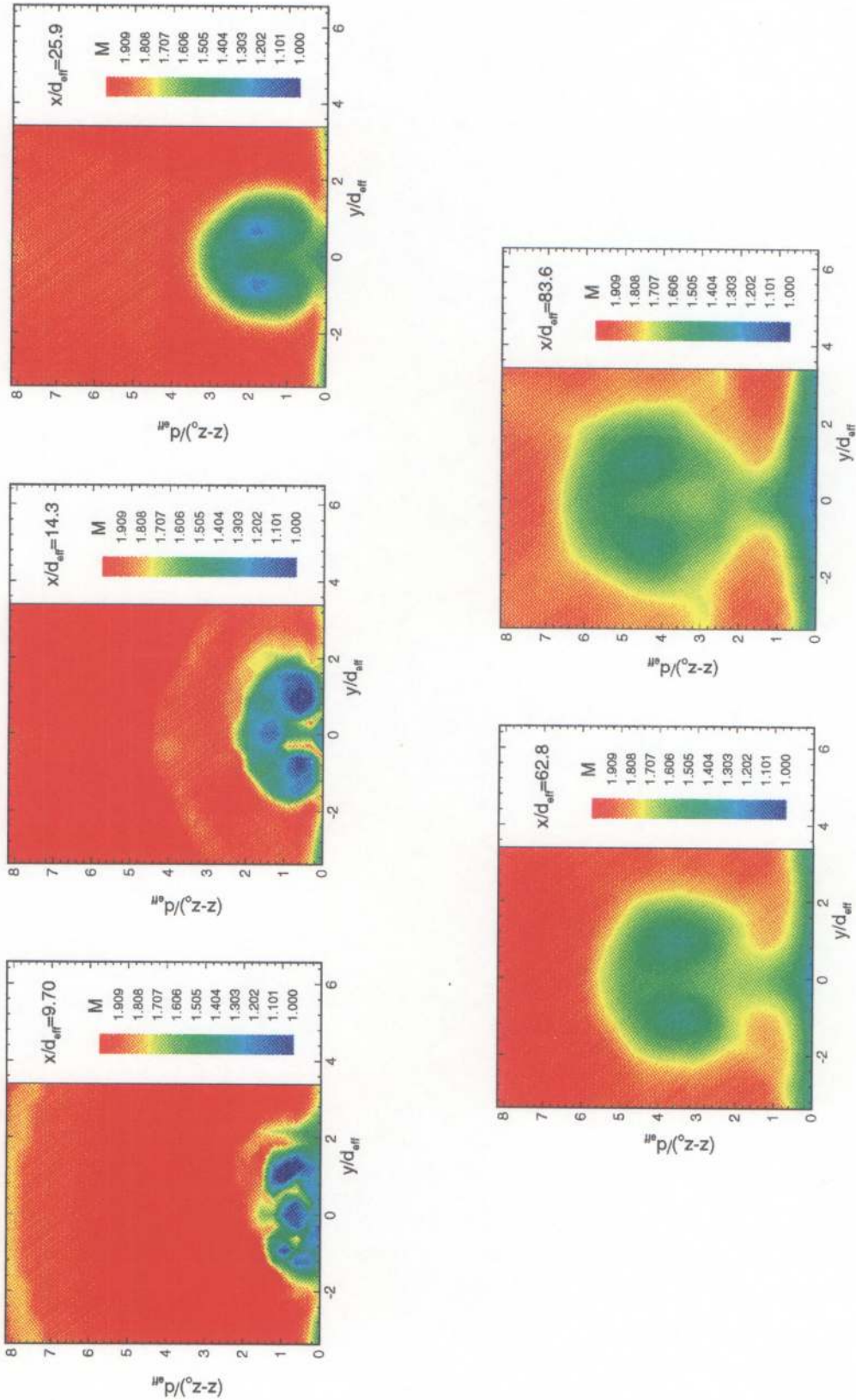
Figure 6.24 Mach number contours; physical ramp, $\bar{q} = 1.0$.
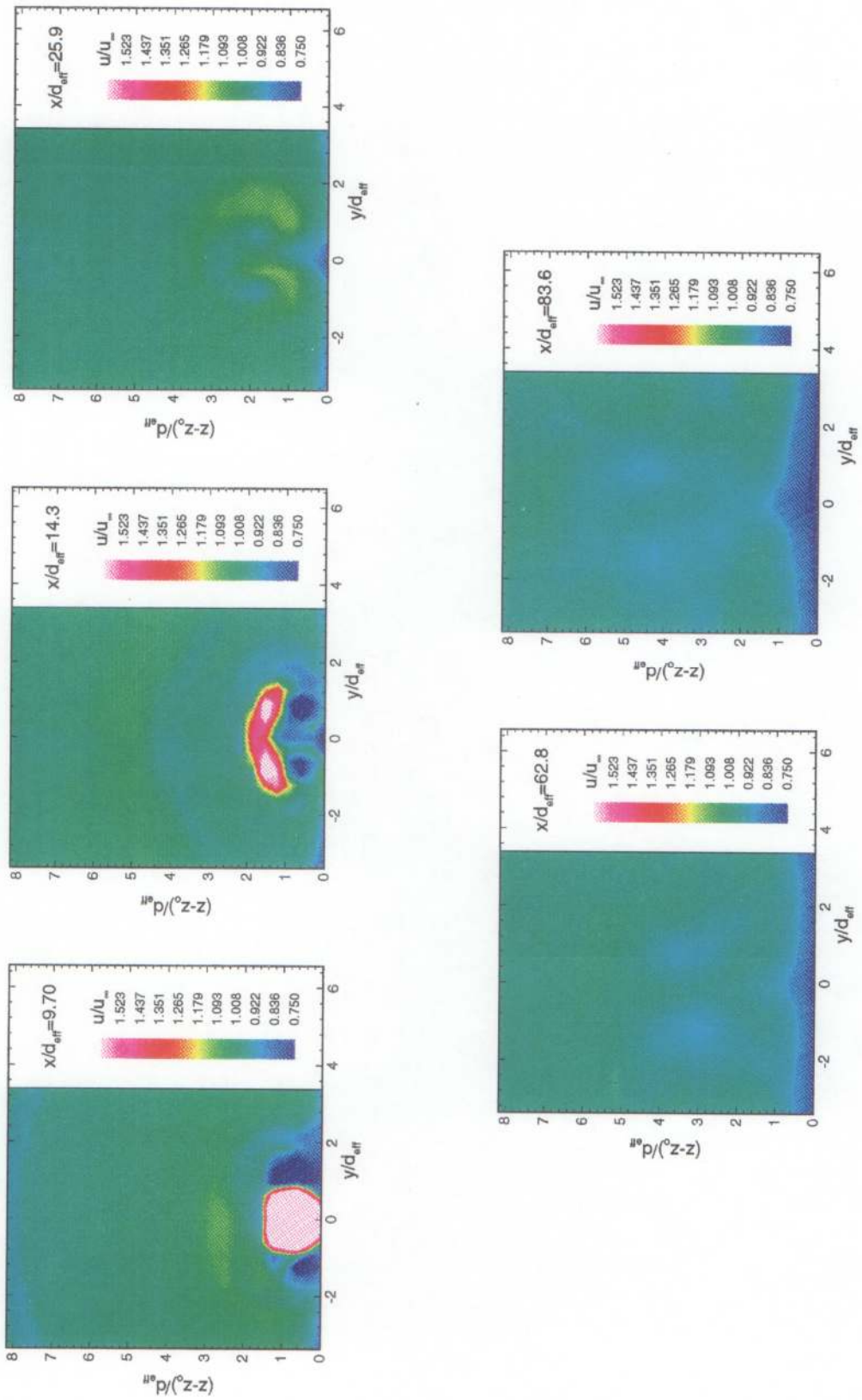
Figure 6.25 Velocity contours; physical ramp, $\bar{q} = 1.0$.
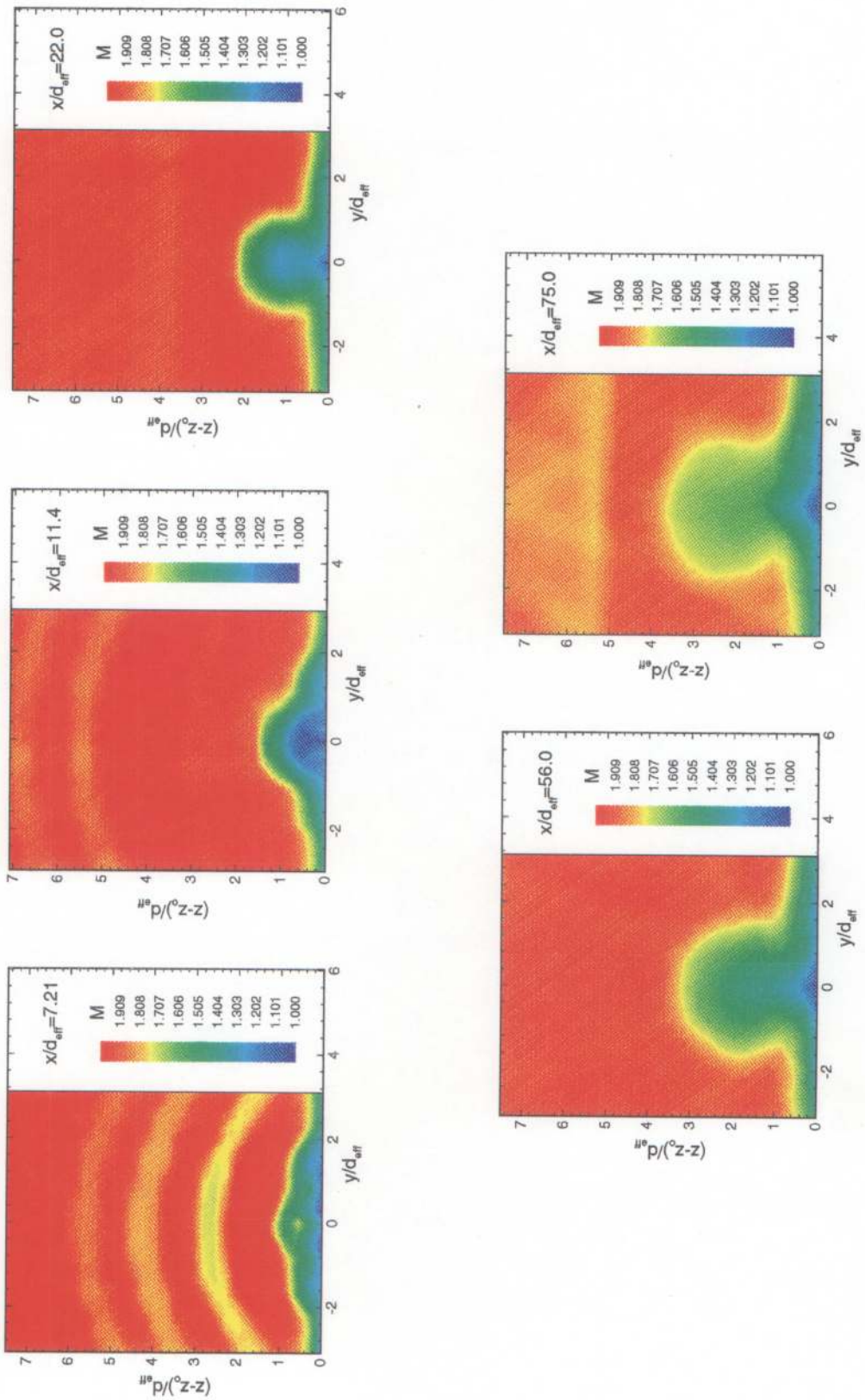
Figure 6.26 Mach number contours; aero-ramp, $\bar{q} = 1.0$.
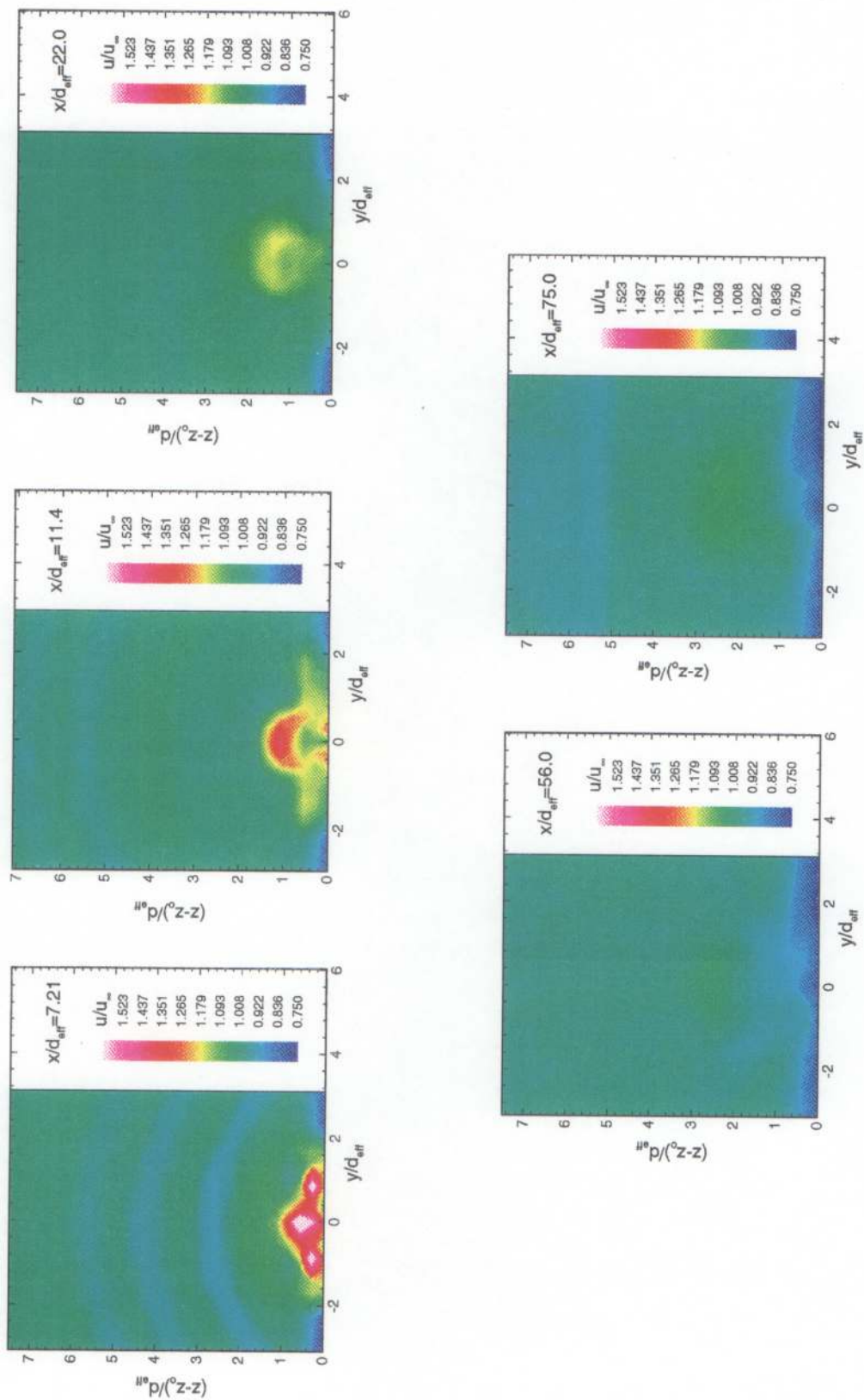
Figure 6.27 Velocity contours; aero-ramp, $\bar{q} = 1.0$.
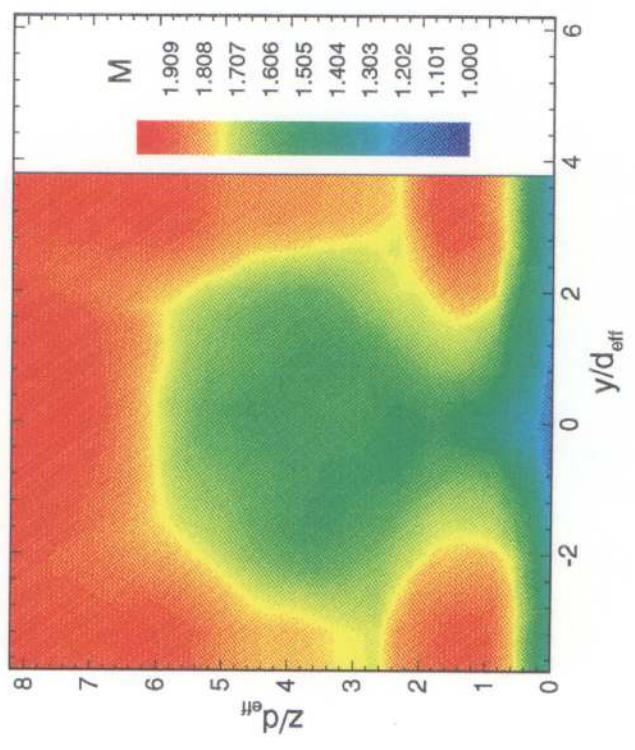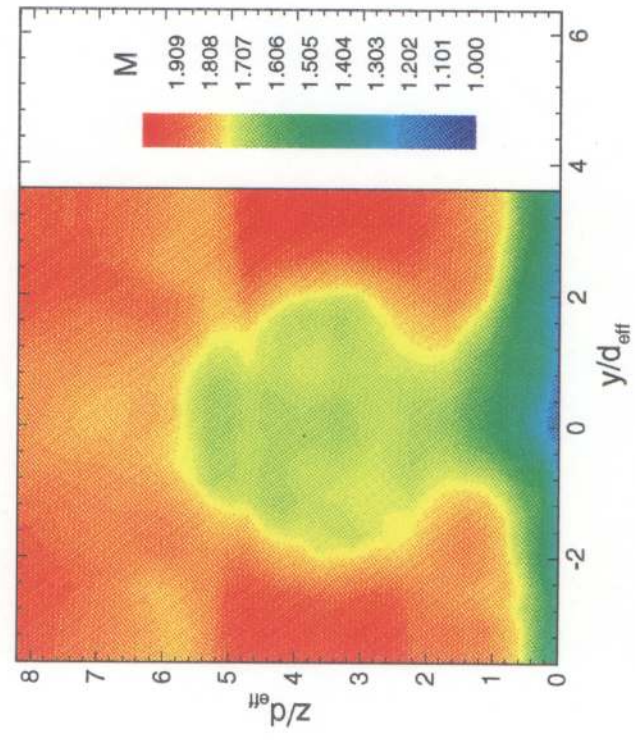
Figure 6.28 Mach number contours; physical ramp and aero-ramp, $\bar{q} = 2.0$.
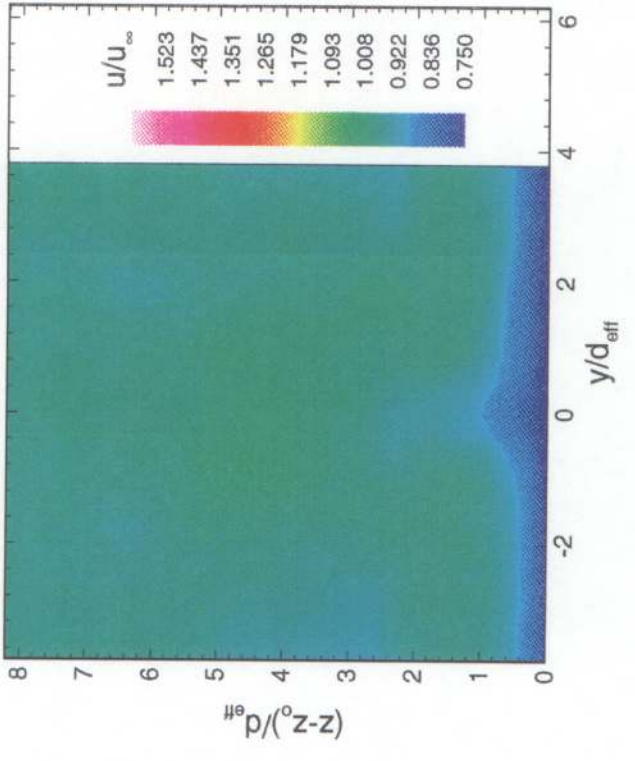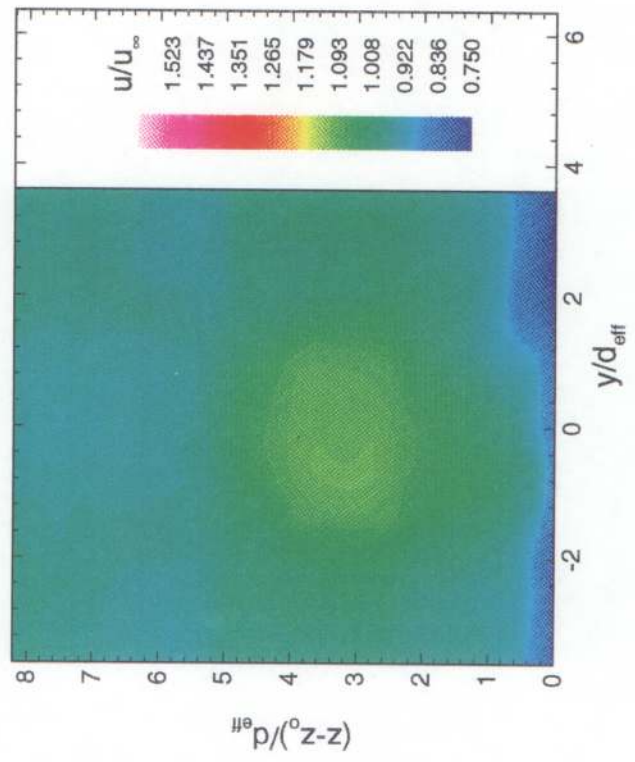
Figure 6.29 Velocity contours; physical ramp and aero-ramp, $\overline{q} = 2.0$.
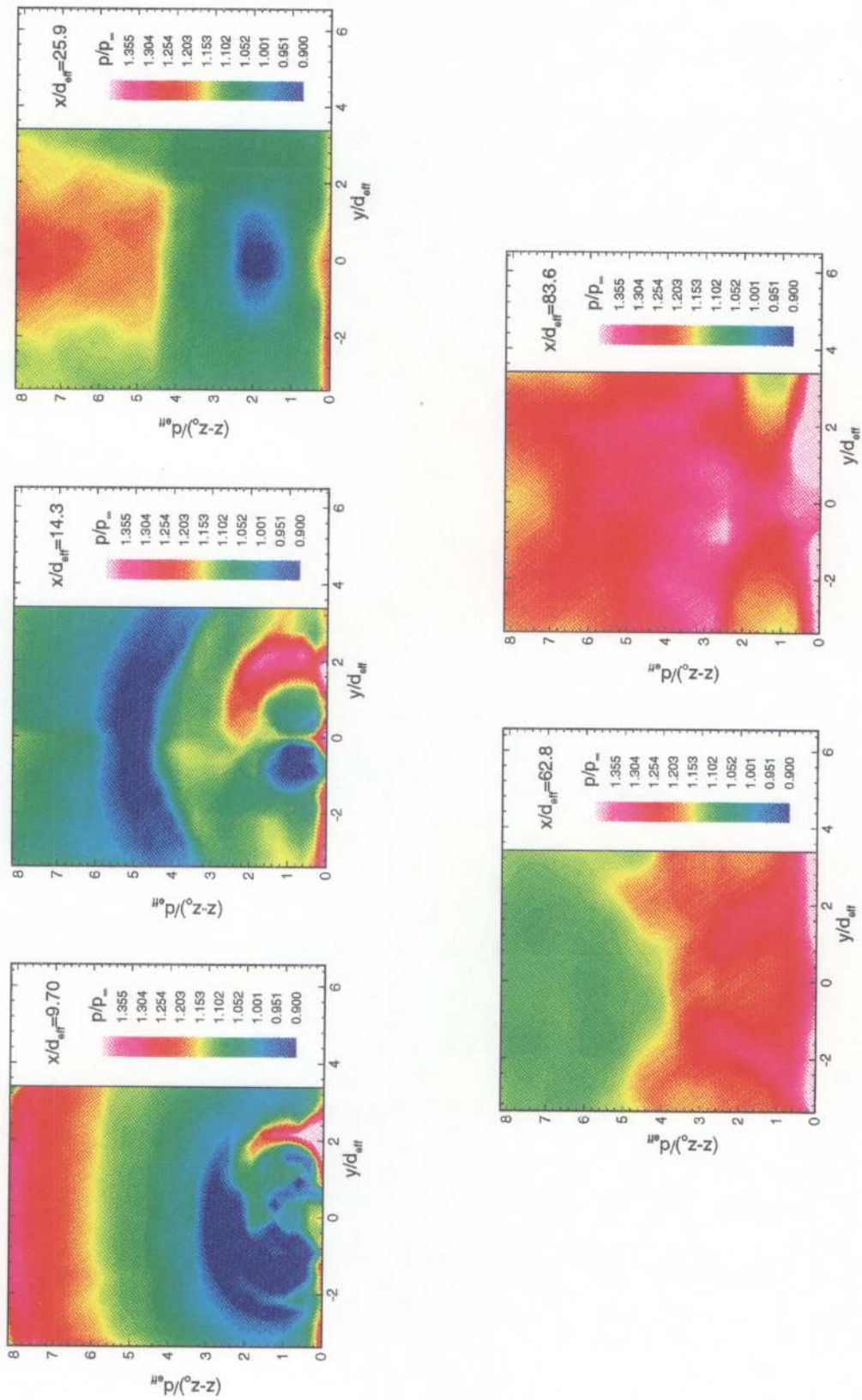
Figure 6.30 Static pressure contours; physical ramp, $\bar{q} = 1.0$.
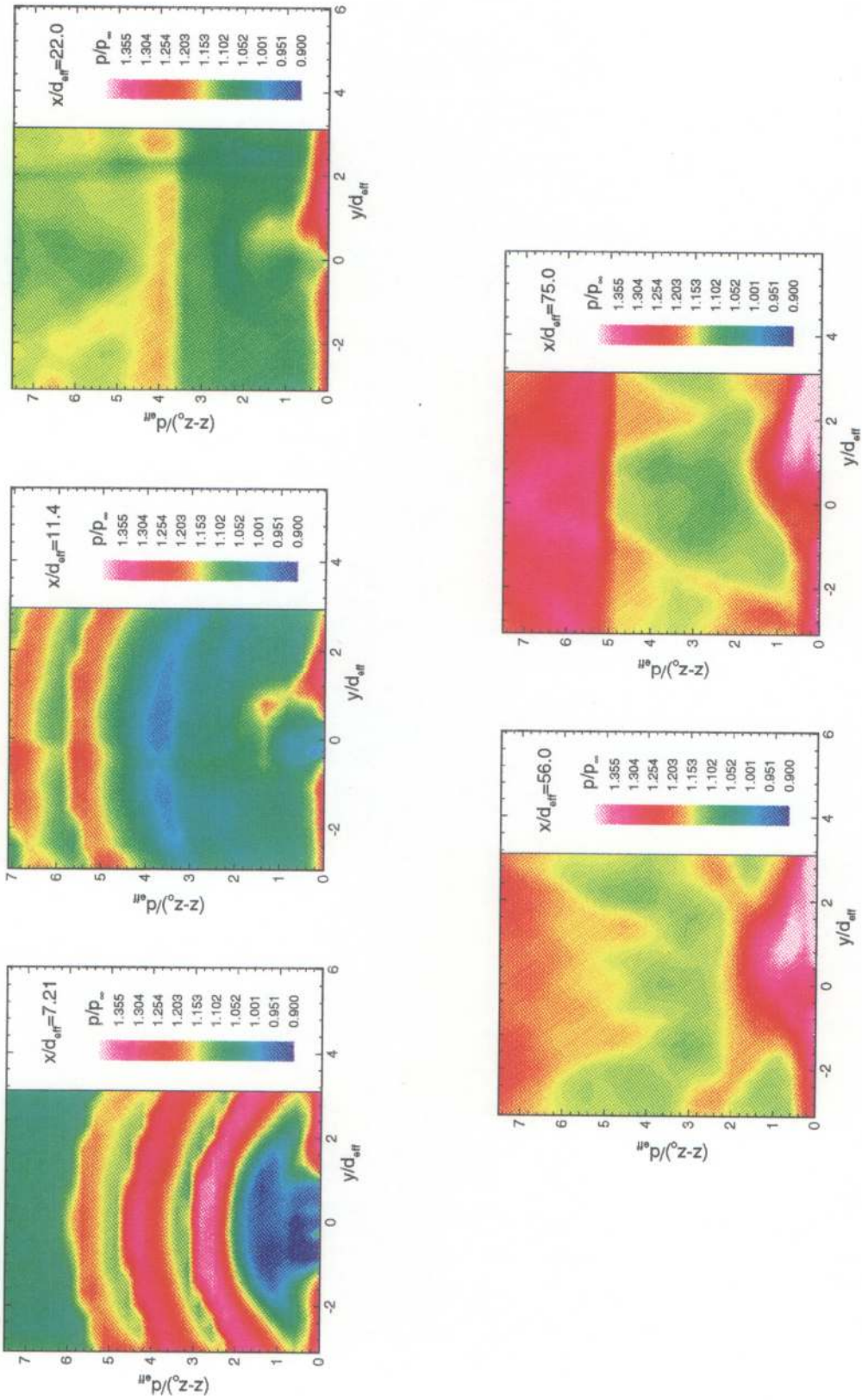
Figure 6.31 Static pressure contours; aero-ramp, $\bar{q} = 1.0$.
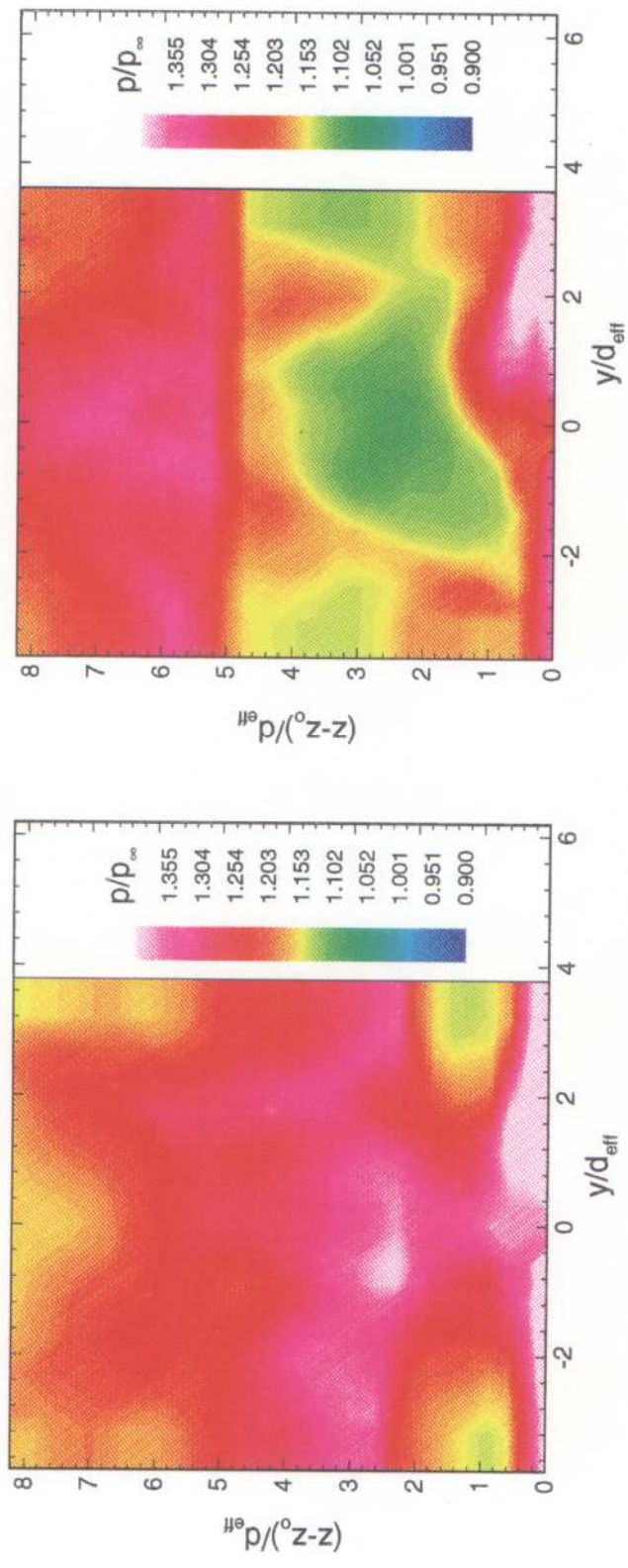
Figure 6.32 Static pressure contours; physical ramp and aero-ramp, $\bar{q} = 2.0$.
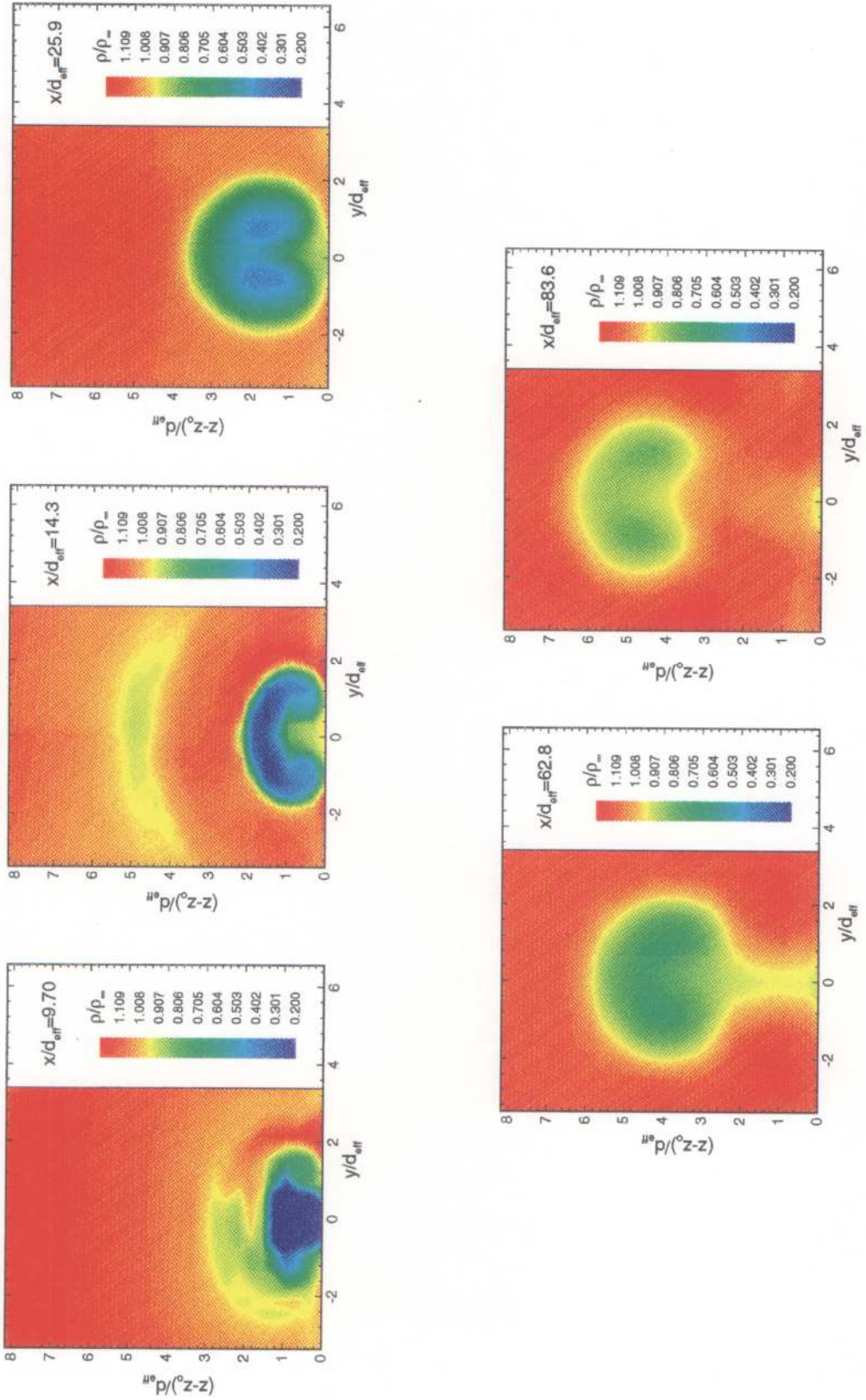
Figure 6.33 Density contours; physical ramp, $\overline{q} = 1.0$.
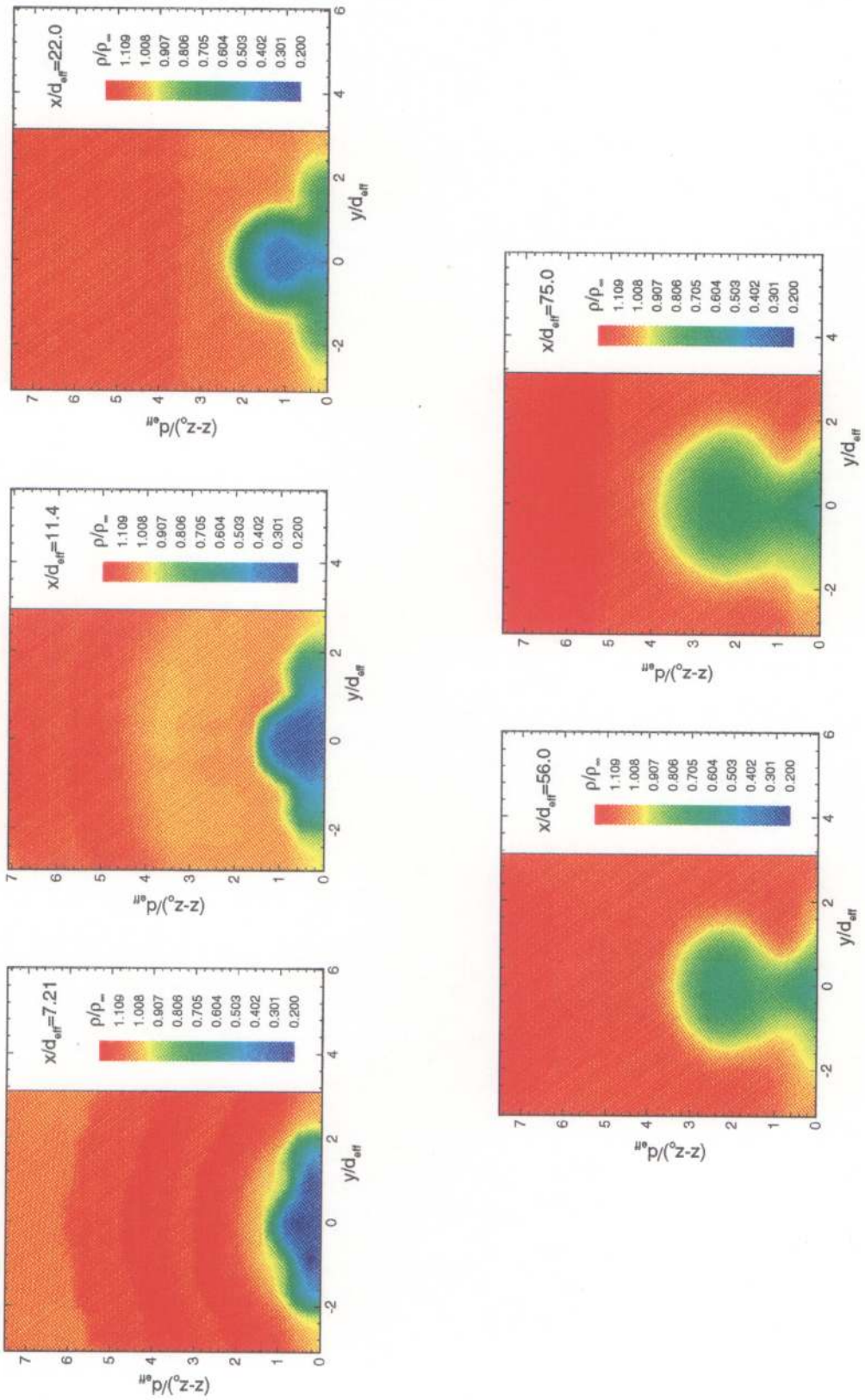
Figure 6.34 Density contours; aero-ramp, $\bar{q} = 1.0$.
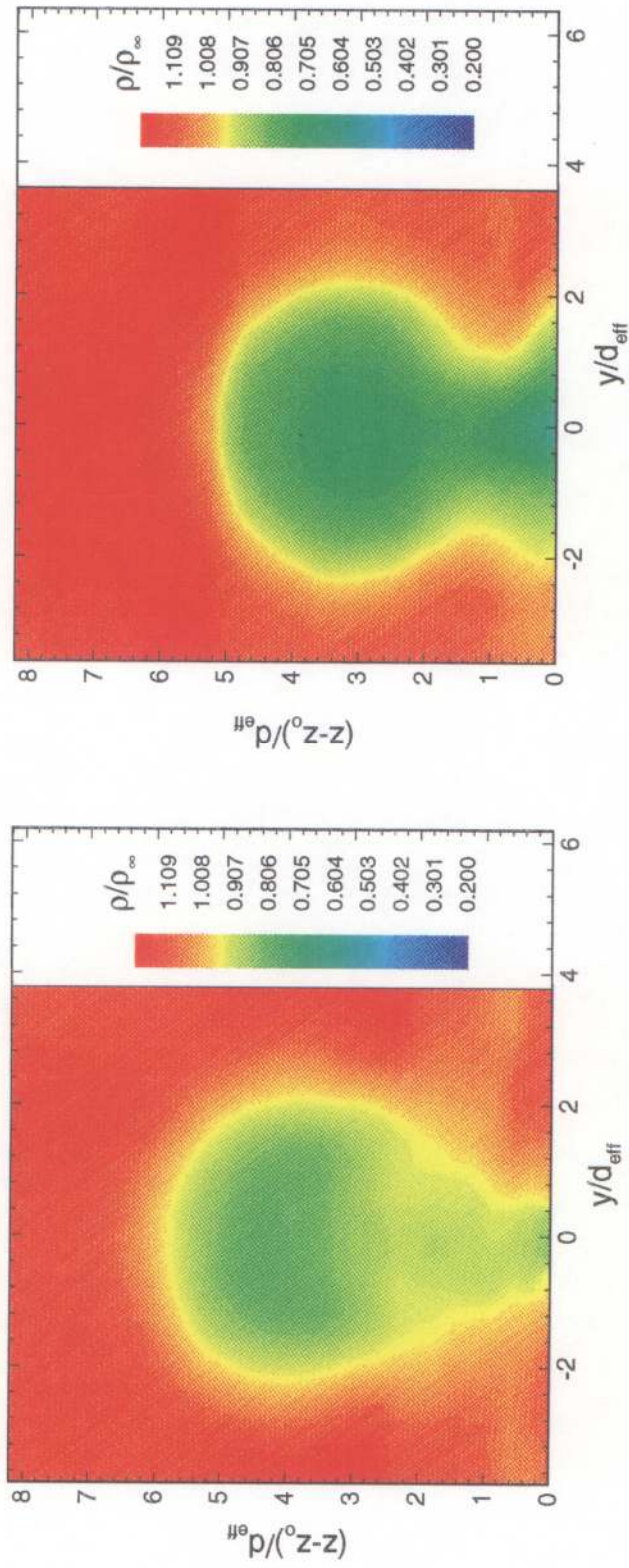
Figure 6.35 Density contours; physical ramp and aero-ramp, $\bar{q} = 2.0$.
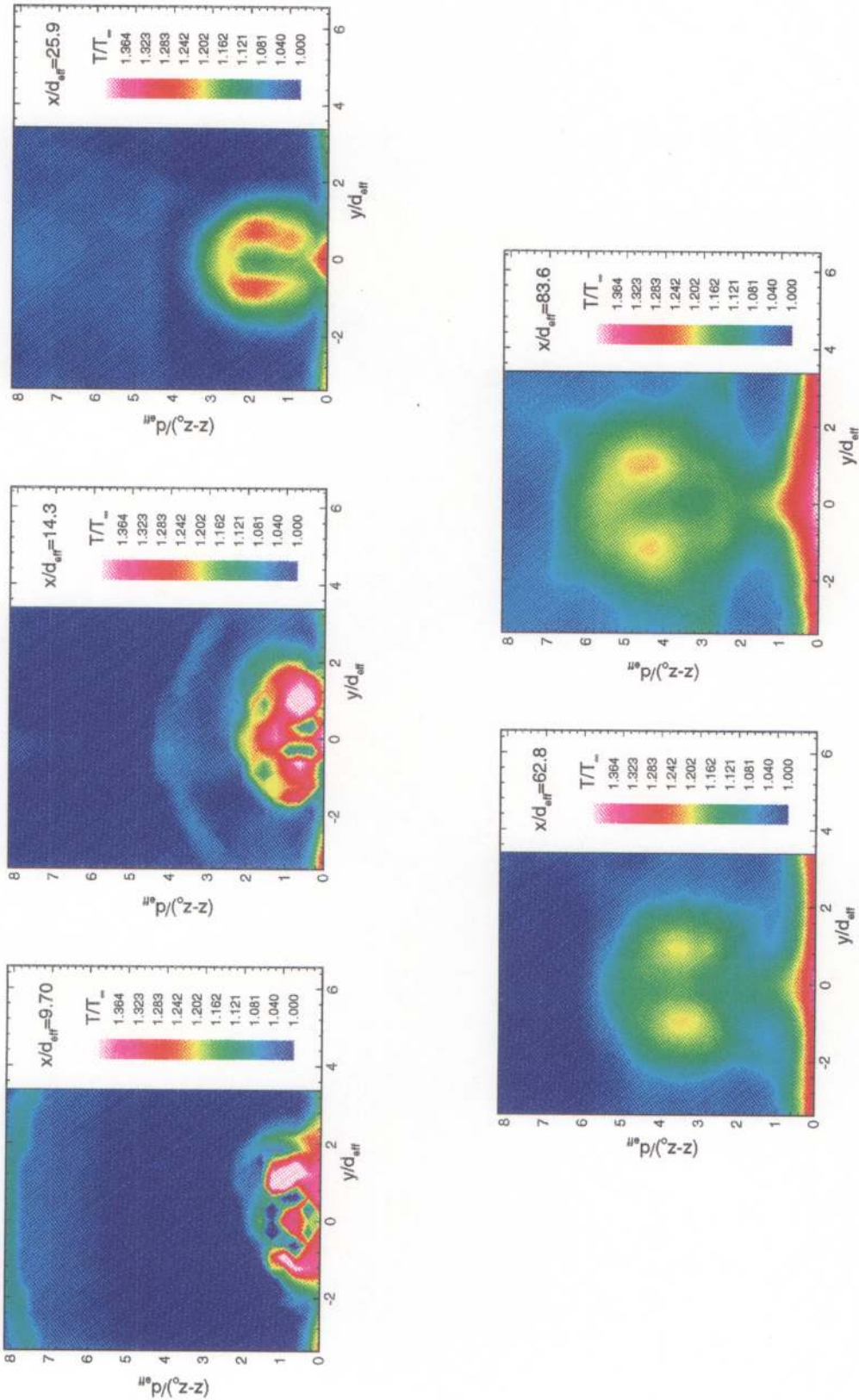
Figure 6.36 Static temperature; physical ramp, $\bar{q} = 1.0$.
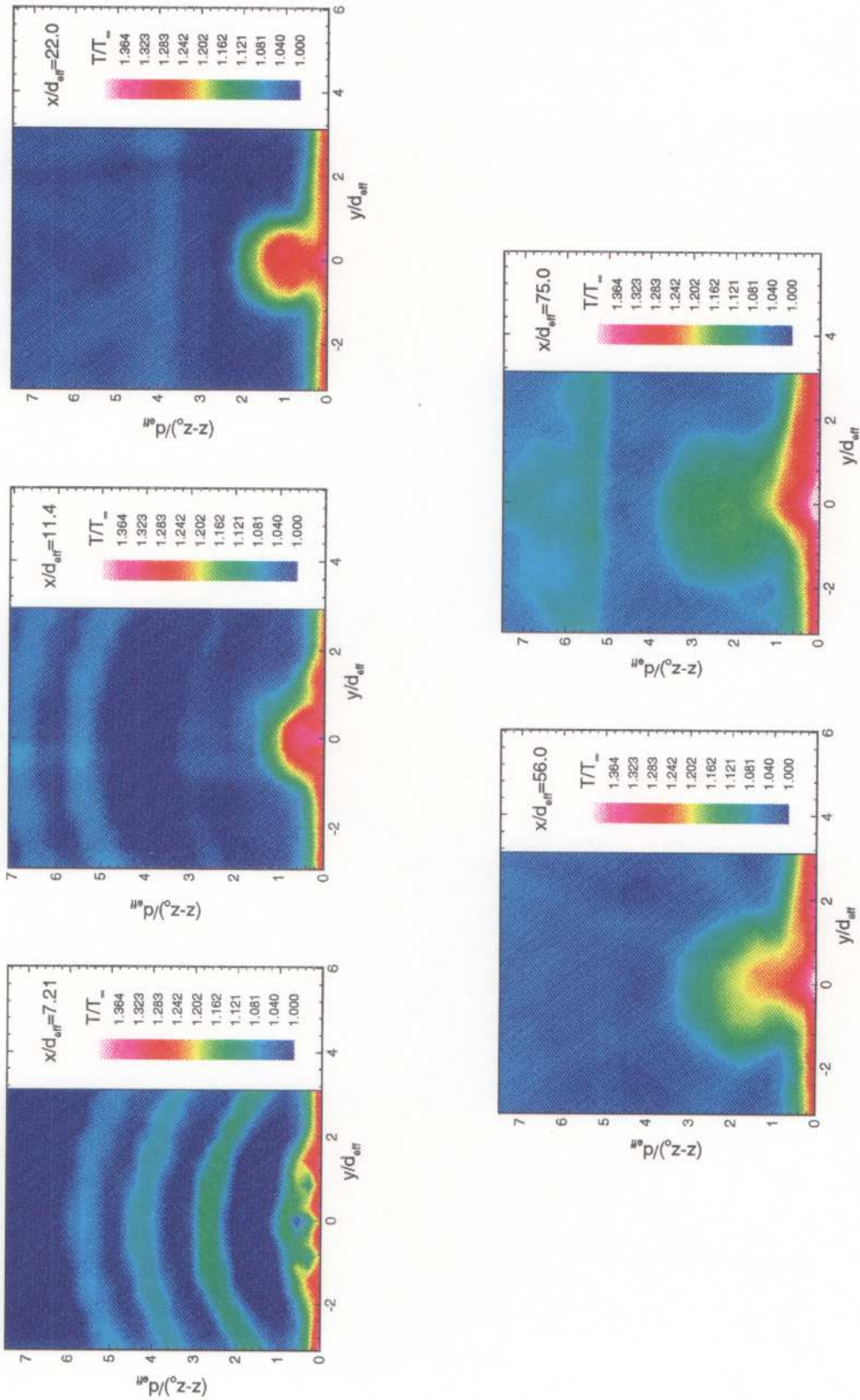
Figure 6.37 Static temperature; aero-ramp, $\bar{q} = 1.0$.
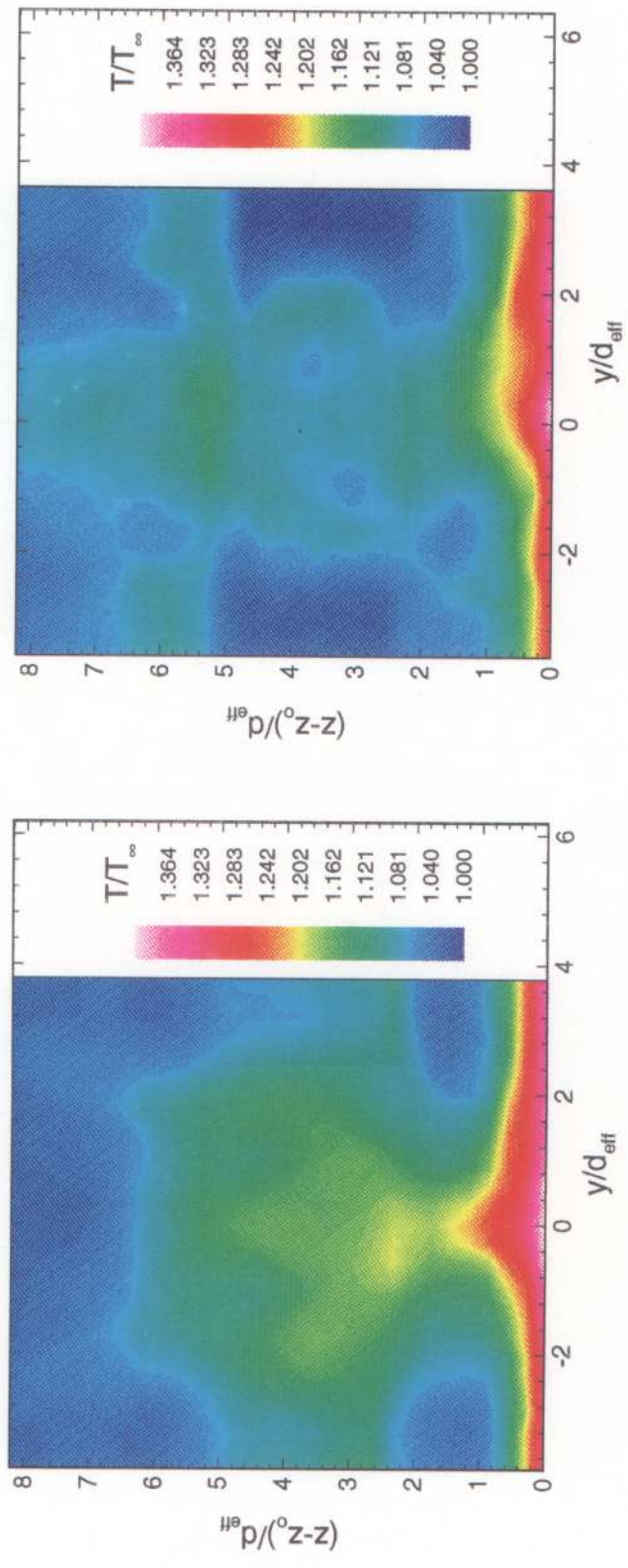
Figure 6.38 Static temperature; physical ramp and aero-ramp, $\bar{q} = 2.0$.
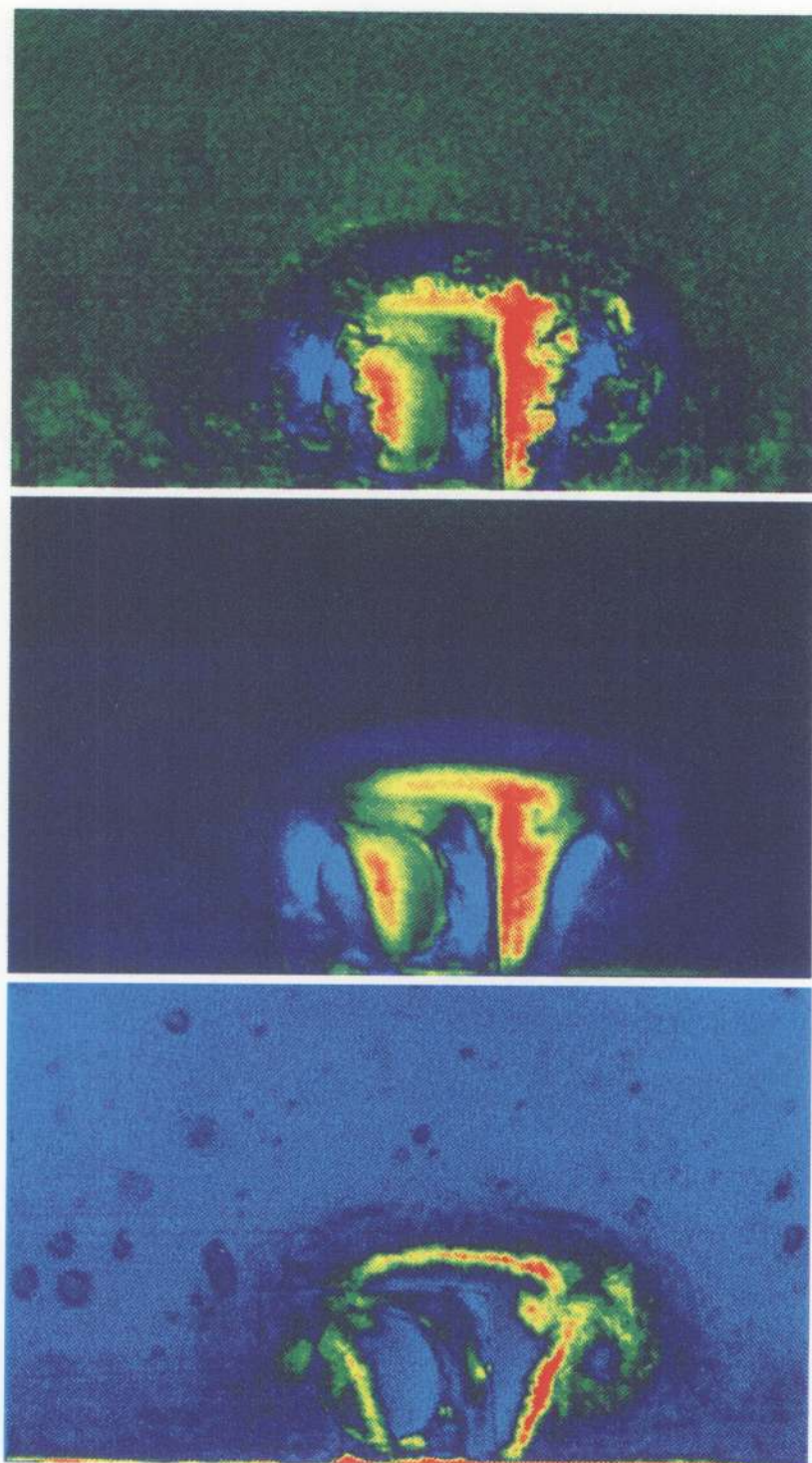
Figure 6.39 Rayleigh scattering; physical ramp, $x/d_{eff} = 9.70$.
Top-to-bottom: a) instantaneous, b) mean, c) std. dev.
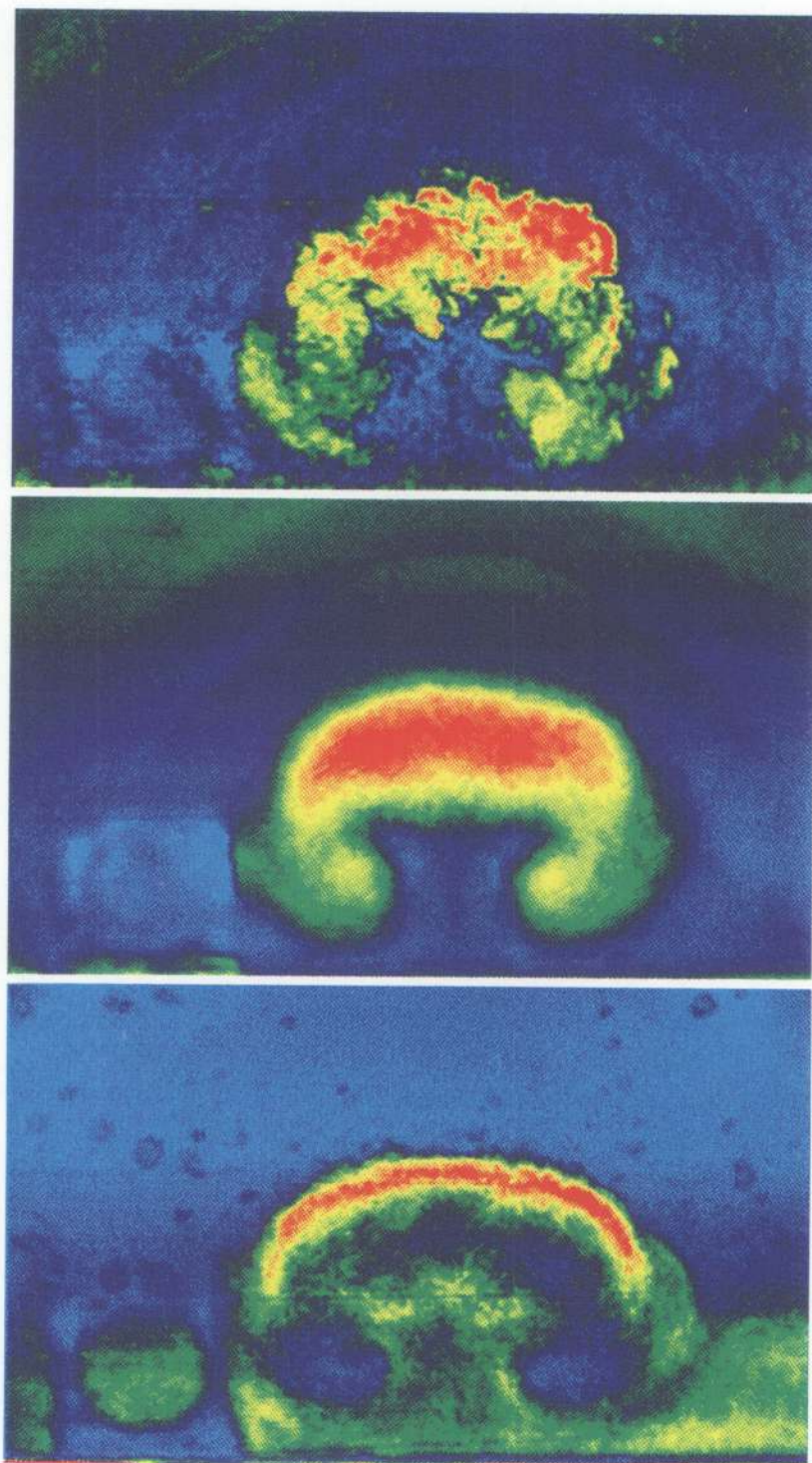
Figure 6.40 Rayleigh scattering; physical ramp, $x/d_{eff} = 14.3$. Top-to-bottom: a) instantaneous, b) mean, c) std. dev.
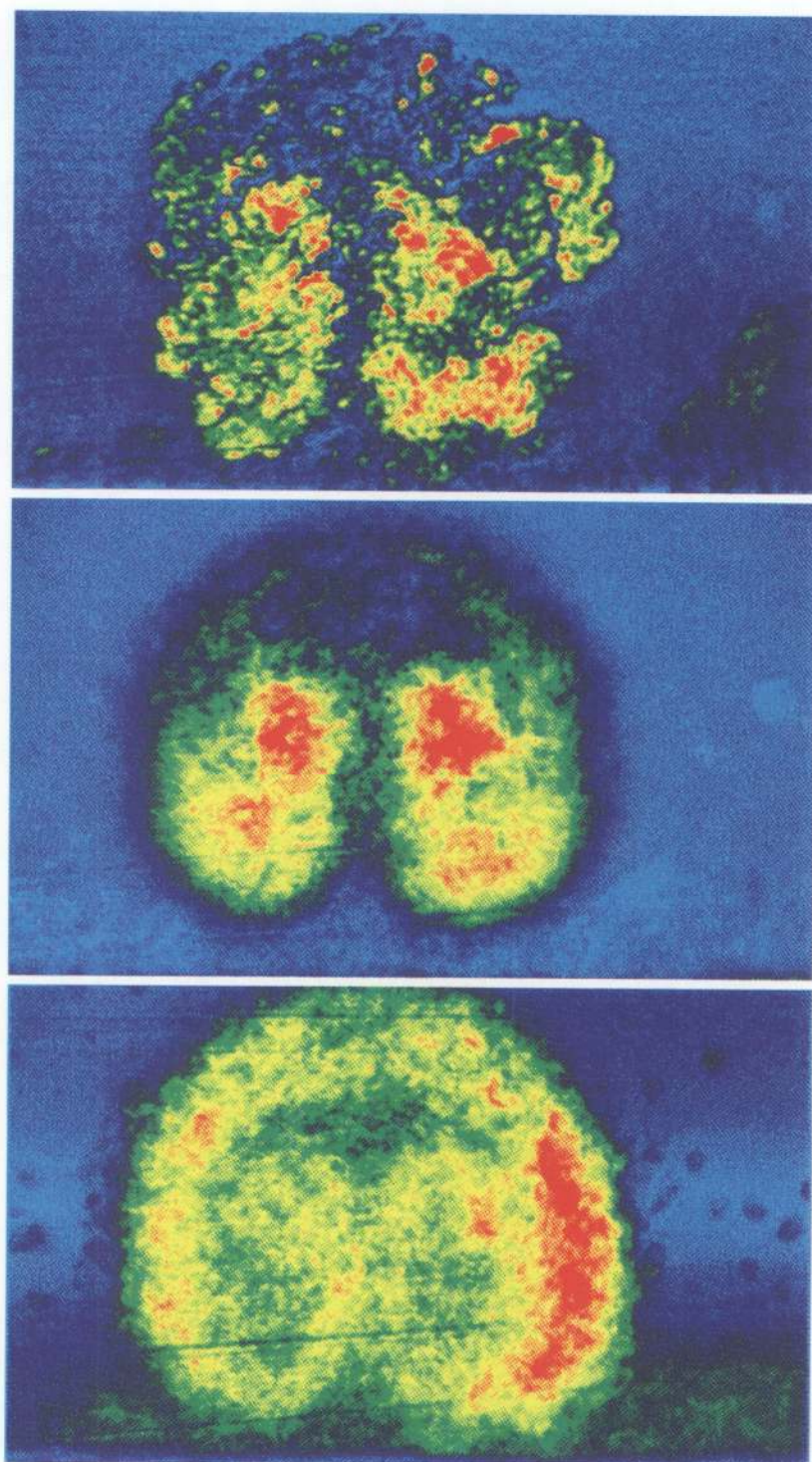
Figure 6.41 Rayleigh scattering; physical ramp, $x/d_{eff} = 25.9$.
Top-to-bottom: a) instantaneous, b) mean, c) std. dev.
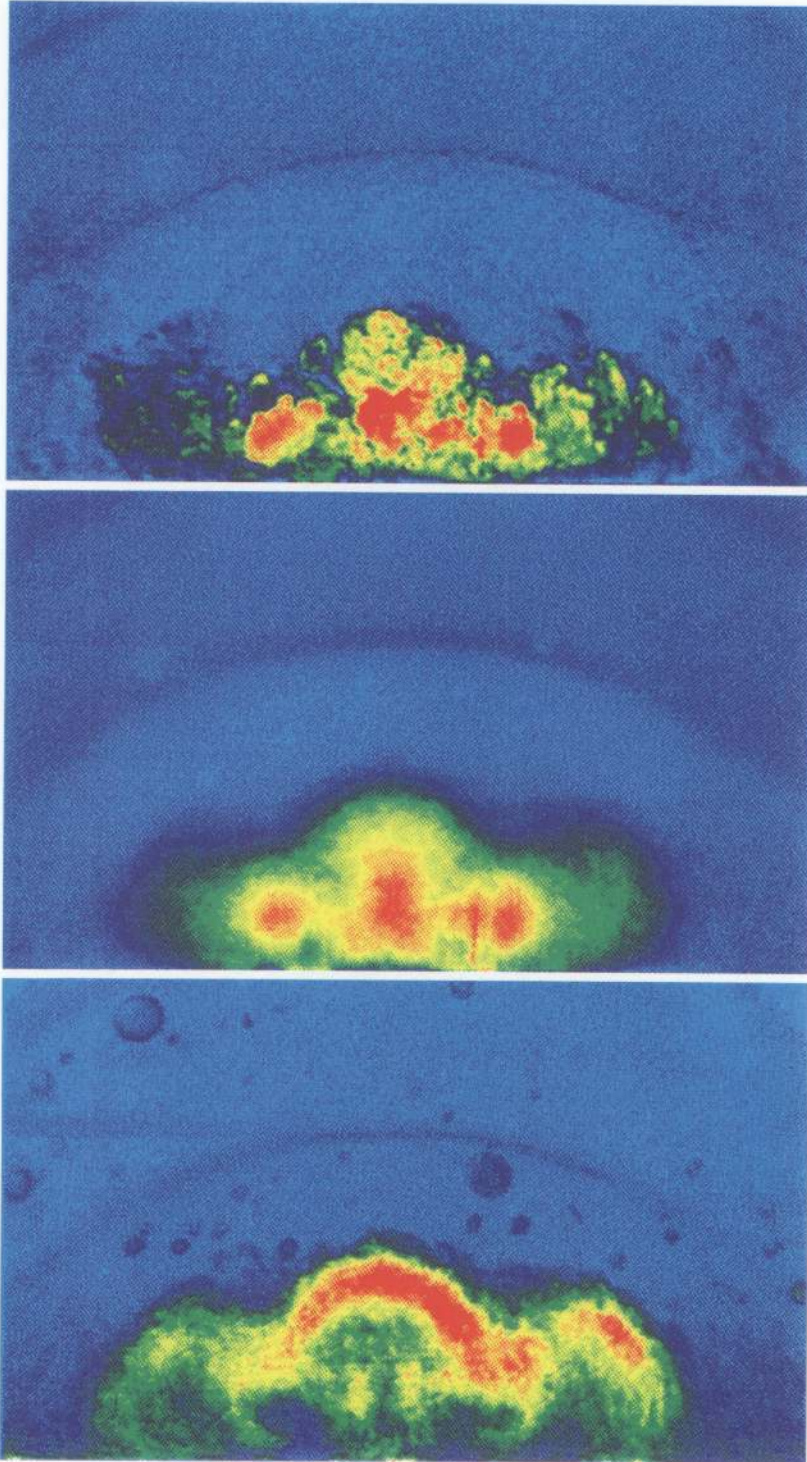
Figure 6.42 Rayleigh scattering; aero-ramp, $x/d_{eff} = 7.21$.
Top-to-bottom: a) instantaneous, b) mean, c) std. dev.
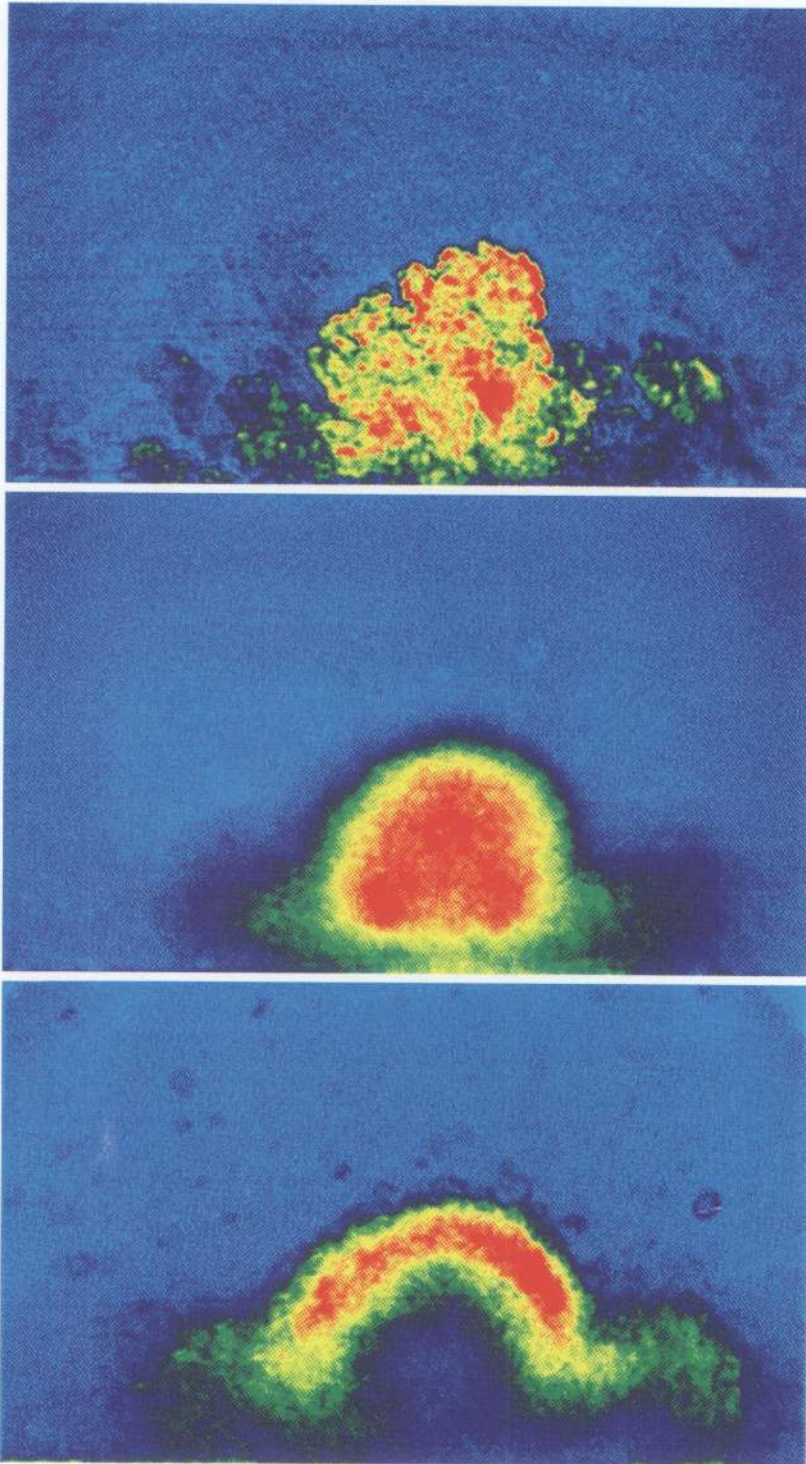
Figure 6.43 Rayleigh scattering; aero-ramp, $x/d_{eff} = 11.4$.
Top-to-bottom: a) instantaneous, b) mean, c) std. dev.
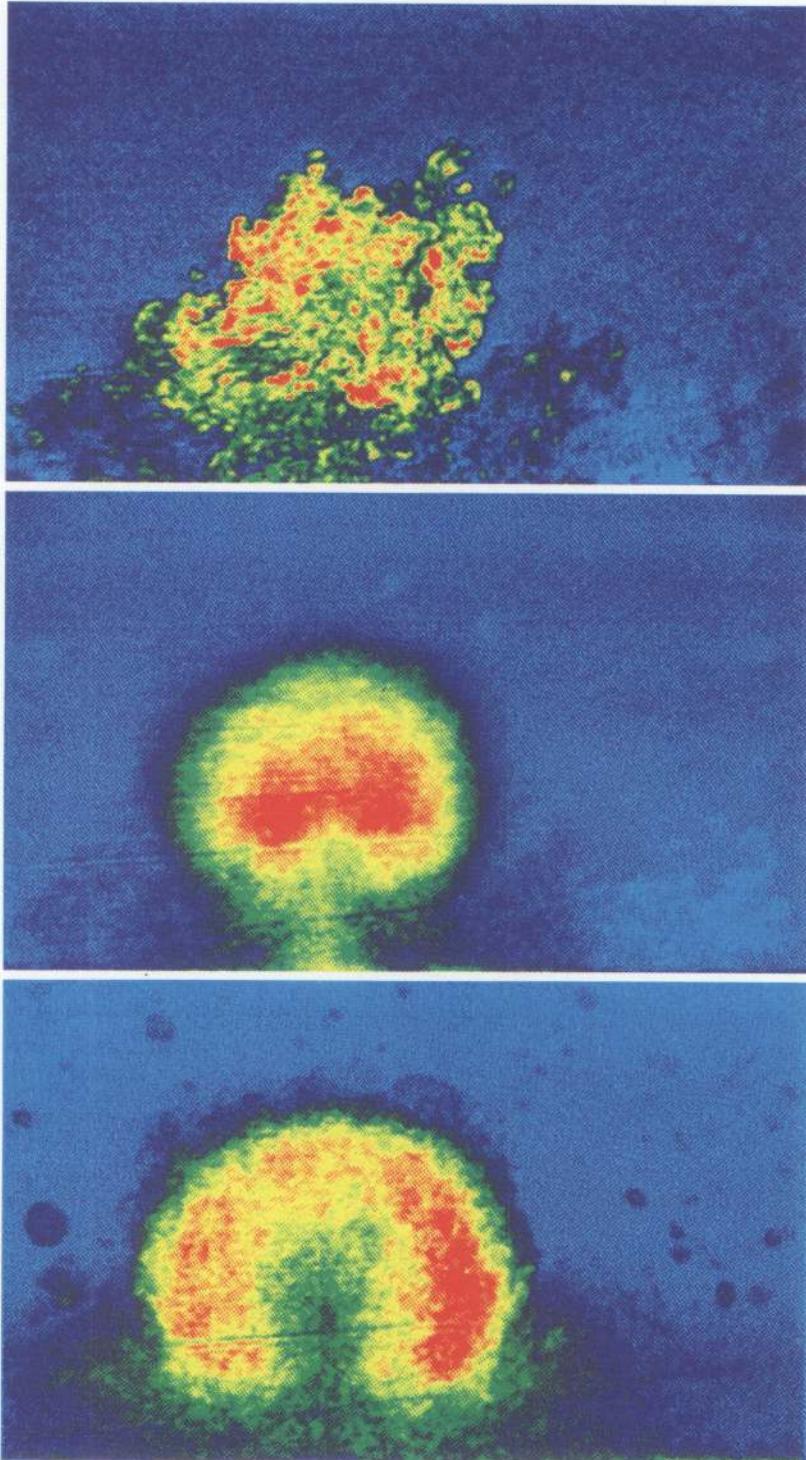
Figure 6.44 Rayleigh scattering; aero-ramp, $x/d_{eff} = 22.0$.
Top-to-bottom: a) instantaneous, b) mean, c) std. dev.
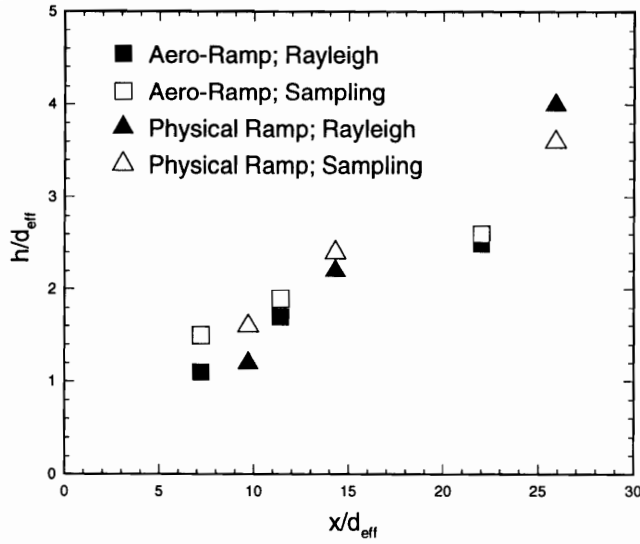
Figure 6.45   Rayleigh scattering: Injectant penetration trajectory.
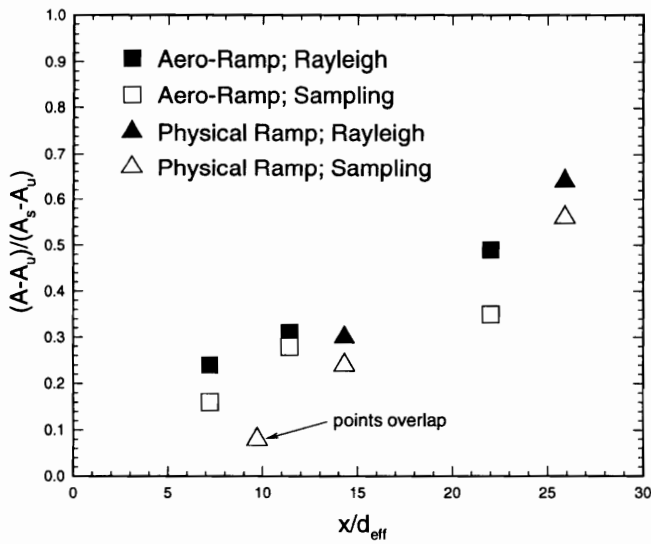
Figure 6.46   Rayleigh scattering: Decay of maximum concentration.
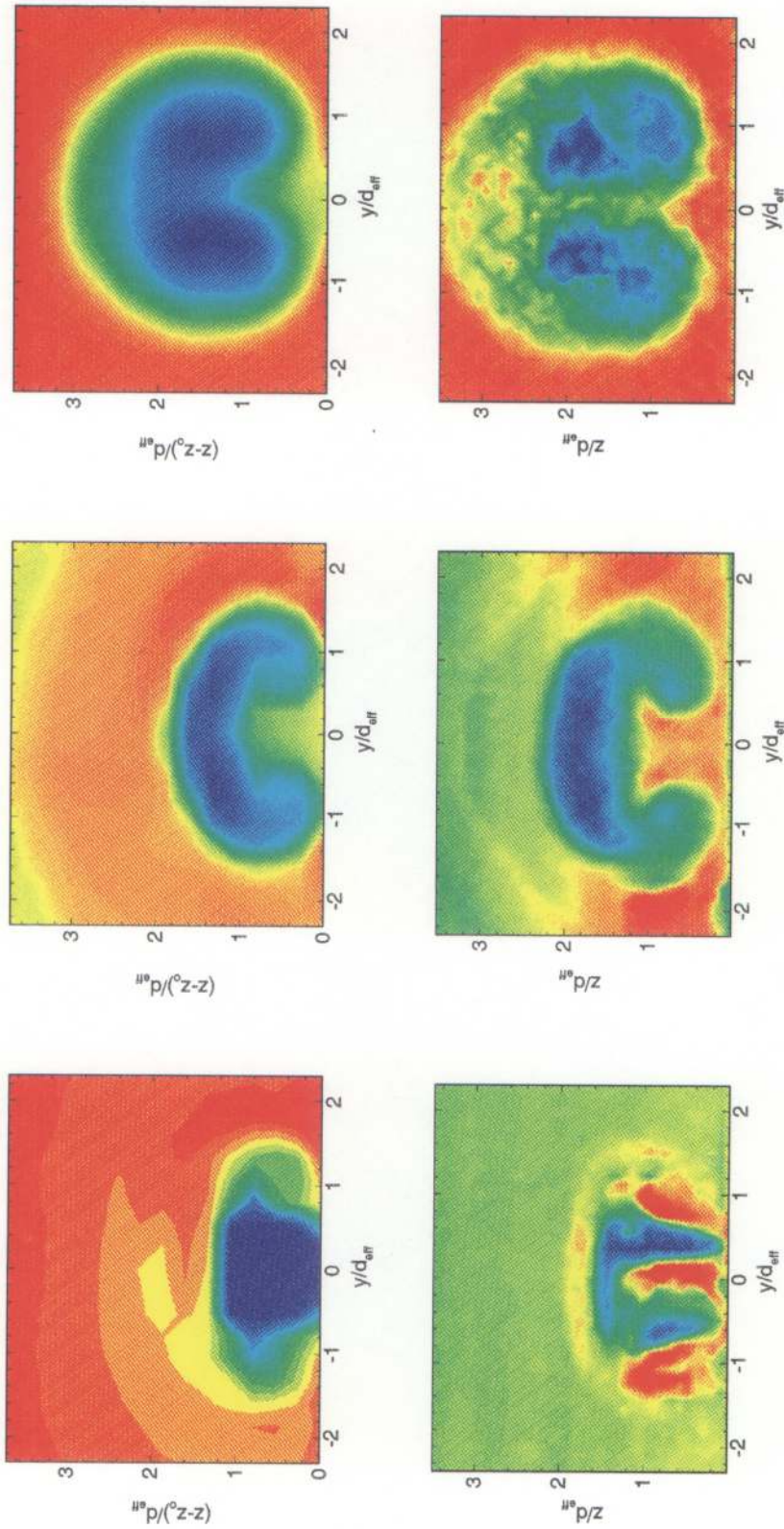
Figure 6.47 Predicted vs. actual scattering intensity; physical ramp, $\overline{q} = 1.0$
Top: Predicted; Left-to-right: $x/d_{eff} = 9.7,\ 14.3,\ 25.9$.
Bottom: Actual; Left-to-right: $x/d_{eff} = 9.7,\ 14.3,\ 25.9$.
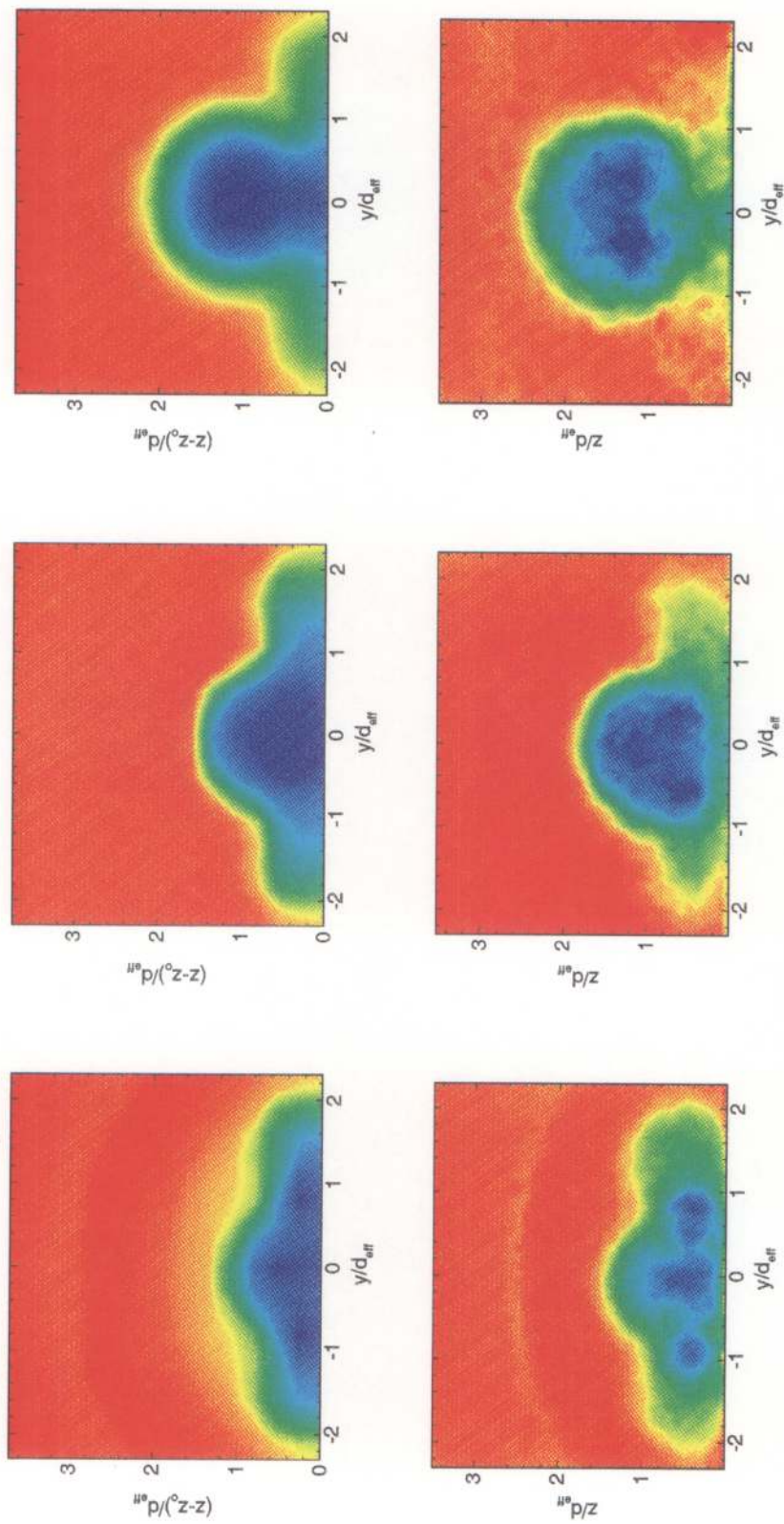
Figure 6.48 Predicted vs. actual scattering intensity; aero-ramp, $\bar{q} = 1.0$
Top: Predicted; Left-to-right: $x/d_{eff} = 7.21,\ 11.4,\ 22.0$.
Bottom: Actual; Left-to-right: $x/d_{eff} = 7.21,\ 11.4,\ 22.0$.

7

Discussion

Experiments were conducted to evaluate the performance of the *aero-ramp*, a novel injector designed to enhance mixing in supersonic flow without the use of intrusive geometry. Identical tests were conducted on a physical swept ramp, a proven *hypermixer*, for comparison. Initial tests, were conducted in a Mach 2.0 freestream with helium injection at a jet-to-freestream momentum flux ratio, $\bar{q}$, of 1.0. It was postulated that the mixing performance of the aero-ramp would improve with increasing $\bar{q}$, while the physcial ramp performance would degrade. Hence, a secondary set of tests were conducted with a $\bar{q}$ of 2.0. Testing included gas sampling, planar-laser Rayleigh scattering, conventional probing, and shadowgraph photography. An array of performance parameters were examined including injectant penetration, decay of maximum concentration, mixing efficiency, and spatial mixedness. Additionally, two new parameters were defined to quantify first, losses based on an integrated total pressure deficit and second, mixing based a relative plume area. Finally, the quantitative nature of the Rayleigh scattering measurements was examined through correlation with the gas sampling and probing measurements.

Results of the shadowgraph photography were the first to indicate a significant performance increase for the aero-ramp with increasing $\bar{q}$. The *time-averaged* shadowgraphs clearly show the mean penetration height of the helium jet in the Mach 2.0 main flow. When $\bar{q}$ was increased from 1.0 to 2.0, the aero-ramp exhibited a significant increase in penetration height while the physical ramp showed no discernible change. This should be expected since the 10.3° jet of the physical ramp is nearly parallel to the freestream, while the jets of the aero-ramp range from 15° to 45°. These results prompted the need to conduct a complementary set of tests at the higher jet-to-freestream momentum flux ratio of 2.0.

An adjunct but noteworthy result of the shadowgraph photography was that of the apparent *effective jet angle*. Close examination of the shadowgraphs taken of the aero-ramp with air injection and no main flow reveal jet angles which are higher than their respective injector port angle. This is to be expected since the degree to which the jet may expand is much more restricted near the wall. This will push the jet upwards away from the wall and effectively redirect the jet momentum. It is postulated here that, the *effective jet angle* should increase with jet-exit pressure for a constant back pressure. Furthermore, the amount of deflection should increase with decreasing injector port angle. Of course, the presence of a main flow will tend to cancel this effect to some extent. Hence, it is also postulated here that, the *effective jet angle*, θ_{eff}, in the presence of a main flow should correlate with the expansion ratio, P_j/P_{eb}, and injector port angle, θ. Finally, it should be noted that injector port length can affect the jet exit angle. Injector port l/d ratios must be sufficiently large to establish a jet momentum parallel to the port axis.

Results of the probing and sampling measurements reveal two distinctly different mixing distributions for the physical ramp and aero-ramp injectors. The physical ramp mixing is strongly dominated by the counter-rotating vortex pattern throughout the entire axial range tested. As the jet-to-freestream momentum flux ratio is increased, these vortices are weakened and the mixing is expected to degrade. The aero-ramp, on the other hand, shows no large-scale vortex domination, but does exhibit hypermixing in the very near field. This near-field hypermixing is attributed to the creation of multiple fuel-vortex interactions in the vicinity of the jets. Unlike with the physical ramp, these interactions should become stronger with increasing $\bar{q}$ and the mixing should improve.

In quantifying these mixing characteristics, several figures of merit were examined. These included the injectant penetration trajectory and plume area. These are important issues, since it is desirable to establish a uniform distribution of fuel throughout the combustor. A uniform distribution of fuel should provide uniform combustion and therefore a uniform temperature and velocity profile exiting the combustor. This is essential for proper and reliable nozzle performance. At the

lower jet-to-freestream momentum flux ratio of $\overline{q} = 1.0$, the aero-ramp exhibited less than comparable performance in these respects. However, when the jet-to-freestream momentum flux ratio was doubled to $\overline{q} = 2.0$, the aero-ramp exhibited a significant increase in penetration while the physical ramp showed no discernible change. Furthermore, the aero-ramp maintained its relative plume area while the physical ramp decreased significantly. At this condition, the performance of each injector was comparable. It is reasonable to assume, based on physical insight, that further increases in the jet momentum should exhibit the same trends. Thus, one can expect the aero-ramp to outperform the physical ramp at higher values of $\overline{q}$.

Other figures of merit included the decay of maximum concentration, mixing efficiency, and spatial mixedness. Each of these parameters were consistent in the information they provided. That is, for a jet-to-freestream momentum flux ratio of $\overline{q} = 1.0$, the aero-ramp exhibited superior performance in the near field with slightly less than comparable performance in the far field. When the jet-to-freestream momentum flux ratio was doubled to $\overline{q} = 2.0$, the aero-ramp exhibited comparable performance in the far field. Again, it is reasonable to assume, based on physical insight, that the same trends will be observed for further increases in jet momentum.

In the past, other researchers have used the fully-mixed distance to evaluate mixing performance. The fully-mixed distance is defined as the axial distance required for the fuel-air ratio to reach the value needed for complete combustion. This distance corresponds to a maximum concentration of $\alpha_{He} = 0.0292$, a mixing efficiency of $\eta_m = 1.0$, and a spatial mixedness of $1 - U_s = 1.0$. Using the far-field predictions developed for each figure of merit and each injector, the fully-mixed distances were extrapolated. Table 7.1 summarizes the fully-mixed distances for each injector based on maximum concentration, mixing efficiency, and spatial mixedness.

Table 7.1 Fully-mixed distance for $\bar{q} = 1.0$.

	Aero-Ramp $(\mathbf{x/d_{eff}})_{\mathbf{fm}}$	Physical Ramp $(\mathbf{x/d_{eff}})_{\mathbf{fm}}$
$\alpha_{\mathbf{max}} = 0.0292$	240	113
$\eta_{\mathbf{m}} = 1.0$	187	100
$1 - \mathbf{U_s} = 1.0$	218	120

In each case, the fully-mixed distance for the aero-ramp was roughly 1.9 times greater than the physical ramp. Of course, this is only for a $\bar{q}$ of 1.0. Since only the last station was sampled and probed for $\bar{q} = 2.0$, predictions of the fully-mixed distance were not possible. It is the opinion of the author that if combustion were present, the fully-mixed distance would be rendered meaningless. Combustion will almost certainly initiate upstream of the fully-mixed point. Ignition will be governed by the near-field mixing, temporal and spatial fluctuations, and inlet enthalpy. Once combustion begins, there will be heat release which will tend to relaminarize the flow, reduce the rate of growth of the mixing layer, and alter the transport properties. Furthermore, combustion will significantly change the mass density, molecular viscosity, and molecular diffusivity, all of which play an important role in the diffusive mixing mechanisms. Hence, the Schmidt number becomes a very important parameter when performing calculations. Since the far-field mixing is generally dominated by molecular diffusion, the fully-mixed distance for the cold-flow situation provides little information about what can be expected in the combusting case. On the other hand, the very near-field mixing behavior will play a crucial role in the combusting case.

To focus on the near-field mixing characteristics of each injector, planar-laser Rayleigh scattering measurements were performed. These measurements provided information which was consistent with the probing measurements. Furthermore, the images provided information on the statistical behavior of the plume, which was not obtainable with the probing measurements. This statistical nature was revealed in the standard deviation images which yielded a measure of the fluctuating behavior across the fuel-air mixing region. In the very near field, at the first measurement station, the aero-ramp exhibited large fluctuations across nearly the entire plume. The physical ramp, on

the other hand, exhibited large fluctuations only in a very narrow strip around the periphery of the plume. Since these fluctuations indicate where the bulk mixing is occurring, this clearly explains the superior mixing of the aero-ramp in the near field. Further downstream, the differences between the aero-ramp and physical ramp become less distinct. In fact, the appearance is quite similar at the third measurement station. However, at the third measurement station, the spatial extent of the fluctuations produced by the physical ramp is larger than that produced by the aero-ramp. This explains why the mixing of the physical ramp surpasses that of the aero-ramp beyond the second measurement station.

Analysis of the total pressure losses generated by each injector revealed the superior performance of the aero-ramp in all cases tested. For $\overline{q} = 1.0$, the spatial extent of the pressure losses incurred with the physical ramp was larger than that induced by the aero-ramp at all axial stations. Furthermore, the minimum total pressures at each station for the physical ramp were less than the those for the aero-ramp, so the magnitude of the losses was greater. When $\overline{q}$ was increased to 2.0, the spatial extent of the total pressure losses increased for the aero-ramp while it remained relatively constant for the physical ramp. In each case, the overall total pressure values were increased across the regions of influence. This decrease in total pressure loss was attributed to the added axial momentum provided by the jets.

To quantify the behavior of the total pressure losses observed in the previous paragraph in a single value, a total pressure loss parameter was devised. This parameter consistently indicated the same behavior visually observed in the total pressure contours. That is, the total pressure losses incurred with the aero-ramp was less than those produced by the physical ramp in all cases tested. Furthermore, when $\overline{q}$ was increased to 2.0, the losses were lessened for both injectors. Finally, it was noted that the reduction in losses with increasing $\overline{q}$ for the physical ramp was more significant than with the aero-ramp. This should be expected, since almost all of the jet momentum for the physical ramp is near parallel to the freestream. It is reasonable, therefore, to expect that the total pressure losses of the aero-ramp might exceed those of the physical ramp with large increases in $\overline{q}$.

While the pressure losses are extremely important to the thermodynamic efficiency of an air-breathing propulsion system, the total pressure loss parameter by itself has no meaning in the combusting case. With combustion present, the fuel heat release will tend to alleviate these losses. As the fuel burns and releases heat, the total pressure and the velocity will go up as thrust is produced. In the reacting case, one most often speaks of the *thrust potential*. This thrust potential will be decreased by total pressure losses and increased by heat release. Thus, in evaluating an injector design through cold flow studies, one must consider both the total pressure loss as well as the potential for heat release. This potential for heat release is indicated by the degree of mixing. That is, the penetration, area, fuel-air mixture ratio, and spatial uniformity of the fuel plume. In reviewing the results of these experiments, we can see that the aero-ramp outperforms the physical ramp in the near field. It produces better mixing, less losses and therefore, better thrust potential. While the results of the far-field measurements would suggest better thrust potential for the physical ramp, the aforementioned effects of combustion on the far-field mixing could dramatically alter this situation. Hence, an absolute performance comparison of these injectors (or any injector), must be conducted with the presence of combustion.

In any event, the performance of an aero-ramp has been shown to be superior in the near-field and comparable in the far-field to a physical ramp for certain operating conditions. Regardless of the effects of combustion on the far-field behavior, the viability of flush-wall injection has been established. In lieu of overcoming the practical problems associated with an intrusive geometry such as for the physical ramp, the need for better understanding the effects of multiple, low-angled impinging jets in a supersonic mainstream has come into focus.

An adjunct study within this investigation examined the correlation of the Rayleigh scattering intensity with the thermodynamic probing and gas sampling measurements. A relationship was derived to predict the Rayleigh scattering intensity based on local pressure, temperature, and helium mole fraction. This relationship involved a single constant of proportionality, β. Unfortunately, practical problems associated with unavoidable laser reflections prevented accurate determination

of this constant. Hence, the absolute quantitative nature of the Rayleigh scattering could not be accurately established for these experiments. However, the qualitative comparsion between the probing measurements and the Rayliegh scattering is quite good considering the complexity of the technique. With the normalization procedures applied to both techniques, the value of β is very near unity, $\beta \approx 1$, outside the influence of reflections. If the reflections could be eliminated, this technqiue show strong promise for quantitative measurements. Since the scattering intensity is a function of the ratio of pressure to temperature, knowledge of the density field only is required to determine helium mole fraction. Perhaps, a complementary technique such as holographic interferometric tomography could be employed to determine the density field.

8
Conclusions and Recommendations

An experimental investigation was conducted to compare the performance of the aero-ramp injector with a physical ramp injector previously shown to enhance mixing in supersonic flow. The scope of the investigation focused on jet penetration, mixing characteristics, and total pressure losses. Several analysis techniques were applied to evaluate the mixing characteristics and all provided consistent results. Furthermore, a parameter was defined to quantify the total pressure losses without complex analysis or facility dependence.

The aero-ramp exhibited a significant increase in jet penetration when the jet-to-freestream momentum flux ratio was increased from $\bar{q} = 1.0$ to 2.0, however, the physical ramp showed very little change. As a result, the jet penetration of the aero-ramp was comparable to that of the physical ramp at the higher momentum flux ratio.

The mixing characteristics of the physical ramp injection were dominated by the counter-rotating vortices generated by the ramp. The fuel-air mixing produced by the aero-ramp was dominated by the multiplicative fuel-vortex interactions confined to the injector vicinity. Mixing effectiveness was based on maximum fuel mass fraction, plume area, mixing efficiency, and spatial mixedness. With a jet-to-freestream momentum flux ratio of $\bar{q} = 1.0$, the aero-ramp produced superior mixing in the near field and slightly less than comparable mixing in the far field. With a momentum flux ratio of $\bar{q} = 2.0$, the aero-ramp mixing was comparable to that of the physical ramp in the far field. The enhanced mixing of the aero-ramp can be attributed to the multiplicative fuel-vortex interactions in the near field as well as the multiple jet design. That is, several small jets should mix better than one single jet. The enhanced mixing of the physical ramp can be attributed to the counter-rotating vortex pair. The increased jet momentum reduced the strength of the vortices produced by the

physical ramp while it increased the strength of the interactions produced by the aero-ramp. Thus, the mixing performance decreased with increasing jet momentum for the physical ramp while it increased for the aero-ramp.

For the physical ramp, the total pressure losses were concentrated around the centers of the two counter-rotating vortices. For the aero-ramp, the total pressure losses were concentrated around the core of the jet plume. The pressure losses induced by the physical ramp were more severe. With a jet-to-freestream momentum flux ratio of $\bar{q} = 1.0$, the physical ramp exhibited a larger loss parameter over the entire axial range of measurements. When the momentum flux ratio was increased to $\bar{q} = 2.0$, both injectors exhibited a reduction in losses with the physical ramp losses still being more severe.

The performance of an aero-ramp has been shown to be superior in the near-field and comparable in the far-field to a physical ramp for certain operating conditions. Regardless of the effects of combustion on the far-field behavior, the viability of flush-wall injection has been established. In lieu of overcoming the practical problems associated with an intrusive geometry such as the physical ramp, the need for better understanding the effects of multiple, low-angled impinging jets in a supersonic mainstream has come into focus. Realization of this understanding should be obtained through experimental investigation of the fundamental behavior. Optimization of performance should be obtained through parametric studies utilizing computational fluid dynamics.

The results of these studies have identified many areas for future work. It is recommended that further experiments be conducted at higher jet-to-freestream momentum flux ratios than tested here to confirm the superior performance of the aero-ramp in the far field. These experiments need not be as extensive as those conducted here. Rather, choose a single axial station such as $x/d_{eff} = 100$ and measure the mixing efficiency and total pressure loss parameter for a $\bar{q}$ of 2.0, 3.0, and 4.0. While this may not truly reflect the absolute behavior in the combusting case, it will at least verify the trends suggested here. That is, that the mixing and pressure losses of the aero-ramp will surpass the physical ramp with increasing $\bar{q}$.

It is also recommended that parametric studies utilizing CFD be conducted to optimize the geometrical configuration of the aero-ramp. The current configuration is an initial design of a novel concept. The arrangement of the jets was based on intuition with the objective of creating multiple fuel-vortex interactions. Parametrics should include a variation of jet spacing, jet angles, and jet orifice shape (i.e. elliptical, wedge-shaped, etc.). At the same time, experimental studies need to be conducted to fully understand the behavior of impinging jets in supersonic flow. This will facilitate the choices for parametric variation.

Further studies need to be conducted to establish the absolute quantitative nature of the Rayleigh scattering measurements. This technique should be combined with a complementary technique to measure the density field. This complementary technique could perhaps involve holographic inter-ferometric topography. Alternatively, the Rayleigh technique could be applied by first seeding the freestream without seeding the the jet and then *vice-versa*. This will provide a system of two in-dependent equations and two unknowns – density and helium mole fraction. It will be important to make sure that reflections off surfaces other than the intended scattering particle be eliminated. Conventional probing can be very tedious and time consuming. The ability to determine absolute mixing parameters with an imaging technique allows for quick screening and parametric optimiza-tion of candidate injectors. The imaging also provides instantaneous and statistical information unobtainable with conventional probing.

While the initial screening of candidate injector designs can be performed in a cold-flow situation, testing must eventually be conducted in the combusting case. Since the aero-ramp has been shown to be a true hypermixer, it is recommended that it be tested in a model scramjet combustor. These tests should include several versions of the aero-ramp produced by the recommended parametric optimization studies. This will allow for the study of ignition characteristics, flame stability, and combustion efficiency. Furthermore, it will provide information on how to best incorporate pilot flame systems, flame holding devices, and multiple injector configurations.

Bibliography

[1]Heiser, W.H., Pratt, D.T., Daley, D.H., and Mehta, U.B., "Hypersonic Airbreathing Propulsion," in AIAA Education Series, Przemieniecki, J. S. (Edit.) AIAA, Washington, D.C., 1994.

[2]Schetz, J.A., Thomas, R.H., and Billig, F., "Mixing of Transverse Jets and Wall Jets in Supersonic Flow," in Separated Flows and Jets, V. V. Kozlov and A. V. Dovgal (Edits.), Springer-Verlag, Berlin, 1991.

[3]Schetz, J.A. and Billig, F.S., "Penetration of Gaseous Jets Injected into a Supersonic Stream," *Journal of Spacecraft and Rockets*, Vol.3, No. 11, November 1966, pp. 1658-1665.

[4]Schetz, J.A., Hawkins, P.F., and Lehman, H., "Structure of Highly Underexpanded Transverse Jets in a Supersonic Stream," *AIAA Journal*, Vol. 5, No. 5, May 1967, pp. 882-884.

[5]Schetz, J.A., Weinraub, R.A., and Mahaffey, R.E.Jr., "Supersonic Transverse Injection into a Supersonic Stream," *AIAA Journal*, Vol. 6, No. 5, May 1968, pp. 933-934.

[6]Schetz, J.A., "Interaction Shock Shape for Transverse Injection," *Journal of Spacecraft and Rockets*, Vol. 7, No. 2, February 1970, pp. 143-149.

[7]Barber, M.J., Roe, L.A., and Schetz, J.A., "Simulated Fuel Injection Through a Wedge-Shaped Orifice Into Supersonic Flow," AIAA Paper 95-2559, July 1995.

[8]Mays, R.B., Thomas, R.H., and Schetz, J.A., "Low Angle Injection into a Supersonic Flow," AIAA Paper 89-2461, July, 1989.

[9]Fuller, E.J., Thomas, R.H., and Schetz, J.A., "Mixing Studies of Helium in Air at High Supersonic Speeds," *AIAA Journal*, Vol. 30, No. 9, September 1992.

[10]Swithenbank, J. and Chigier, N.A., "Vortex Mixing for Supersonic Combustion," *12th Symposium (International) on Combustion*, 1968, pp. 1153-1162.

[11]Povinelli, L.A., Povinelli, F.P., and Hersch, M., "A Study of Helium Penetration and Spreading in a Mach 2 Airstream Using a Delta Wing Injector," NASA TN D-5322, 1969.

[12]Hersch, M., and Povinelli, L.A., "Effect of Interacting Vortices on Jet Penetration into a Supersonic Stream," NASA TM-X-2134, November 1970.

[13]Povinelli, L.A. and Ehlers, R.C., "Swirling Base Injection for Supersonic Combustion Ramjets," *AIAA Journal*, Vol. 10, No. 9, September 1972, pp. 1243-1244.

[14]Schetz, J.A. and Swanson, R.C., "Turbulent Jet Mixing at High Supersonic Speeds," *Zeitschrift Für Flugwissenschaften*, Vol. 21, 1973, pp. 166-173

[15]Tillman, T.G., Patrick, W.P., and Paterson, R.W., "Enhanced Mixing of Supersonic Jets," *Journal of Propulsion and Power*, Vol. 7, No. 6, Novemeber–December 1991, pp. 1006-1014.

[16]Naughton, J.W., Cattafesta, L.N., and Settles, G.S., "An Experimental Study of the Effect of Streamwise Vorticity on Supersonic Mixing Enhancement," AIAA Paper 92-3549, July 1992.

[17]Marble, F.E., Hendricks, G. J., and Zukoski, E.E., "Progress Toward Shock Enhancement of Supersonic Combustion Processes," AIAA Paper 87-1880, June 1987.

[18]Waitz, I.A., Marble, F.E., and Zukoski, E.E., "Vorticity Generation by Contoured Wall Injectors," AIAA Paper 92-3550, July 1992.

[19]Yang, J., Kubota, T., and Zukoski, E.E., "A Model for Characterization of a Vortex Pair Formed by Shock Passage Over a Light-Gas Inhomogeneity," *Journal of Fluid Mechanics*, Vol. 258, January 1994, pp.217-244.

[20]Marble, F.E., Zukoski, E.E., Jacobs, J.W., Hendricks, G.J., and Waitz, I.A., "Shock Enhancement and Control of Hypersonic Mixing and Combustion," AIAA Paper 90-1981, July 1990.

[21]Metwally, O., and Settles, G., "An Experimental Study of Shock Wave/Vortex Interaction," AIAA Paper 89-0082, January 1989.

[22]Northam, G.B., Greenburg, I., Byington, C.S., and Capriotti D.P., "Evaluation of Parallel Injector Configurations for Mach 2 Combustion," *Journal of Propulsion and Power*, Vol. 8, No. 2, March–April 1992, pp. 491-499.

[23]Davis, D.O. and Hingst, W.R., "Progress Toward Synergistic Hypermixing Nozzles," AIAA Paper 91-2264, June 1991.

[24]Waitz, I.A., Marble, F.E., and Zukoski, E.E., "Investigation of a Contoured Wall Injector for Hypervelocity Mixing Augmentation," *AIAA Journal*, Vol. 31, No. 6, June 1993, pp. 1014-1021.

[25]Hartfield, R.J., Hollo, S.D., and McDaniel, J.C., "Experimental Investigation of a Supersonic Swept Ramp Injector Using Laser-Induced Iodine Fluorescence," *Journal of Propulsion and Power*, Vol. 10, No. 1, January–February 1994, pp. 129-135.

[26]Riggins, D.W., McClinton, C.R., Rogers, R.C., and Bittner, R.D., "Investigation of Scramjet Strategies for High Mach Number Flows," *Journal of Propulsion and Power*, Vol. 11, No. 3, May–June 1995, pp. 409-418.

[27]Riggins, D.W., and Vitt, P.H., "Investigation of Scramjet Strategies for High Mach Number Flows," *Journal of Propulsion and Power*, Vol. 11, No. 3, May–June 1995, pp. 419-425.

[28]Cox, S.K., Fuller, R.P., Schetz, J.A., and Walters, R.W., "Vortical Interactions Generated by an Injector Array to Enhance Mixing in Supersonic Flow," AIAA Paper 94-0708, January 1994.

[29]Gruber, M.R. and Nejad, A.S., "Development of a Large-Scale Supersonic Combustion Research Facility," AIAA Paper 94-0544, January 1994.

[30]Carrol, B.F., Dutton, J.C., and Addy, A.L., "NOZCS2: A Computer Program for the Design of Continuous Slope Supersonic Nozzles," University of Illinois at Urbana-Champaign, UILU ENG 86-4007, 1986.

[31]Burke, A.F., "Turbulent Boundary Layers on Highly Cooled Surfaces at High Mach Numbers," AFASD TR 61-645, 1961.

[32]Fiore, A.W., Moore, D.G., Murray, D.H., and West, J.E., "Design and Calibration of the ARL Mach 3 High Reynolds Number Facility," ARL TR 75-0012, 1975.

[33]Smith, R.E., Jr., and Matz, R.J., "A Theoretical Method of Determining Discharge Coefficients for Venturis Operating at Critical Flow Conditions," *Journal of Basic Engineering*, Trans. ASME, Series D, Vol. 84, No. 4, December 1962, pp. 434-446.

[34]Stratford, B.S., "The Calculation of the Discharge Coefficient of Profiled Choked Nozzles and the Optimum Profile for Absolute Airflow Measurement," *Journal of the Royal Aero. Soc.*, Vol. 68, April 1964, pp. 237-245.

[35]Arnberg, B.T., Britton, C.L., and Seidel, W.F., "Discharge Coefficient Correlations for Circular Arc Venturi Flowmeters at Critical (Sonic) Flow," *Journal of Fluids Engineering*, Trans. ASME, June 1974, pp. 111-123.

[36]Ninnemann, T.A. and Ng, W.F., "A Concentration Probe for the Study of Mixing in Supersonic Shear Flows," *Experiments in Fluids*, Vol. 13, 1992, pp. 98-104.

[37]Winkler, E.M., "Design and Calibration of Stagnation Temperature Probes for Use at High Supersonic Speeds and Elevated Temperatures," *Journal of Applied Physics*, Vol. 25, 1954, p. 231.

[38]Hulst, H.C. van de, *Light Scattering by Small Particles*, Dover Publications, Inc., New-York, 1981.

[39]Carter, C.D., "Laser-Based Rayleigh and Mie Scattering Methods," *Handbook of Fluid Dynamics and Fluid Machinery*, Schetz, J.A. and Fuhs, A.E., (Edits.) Wiley, New York, 1996.

[40]Samimy, M. and Lele, S.K., "Motion of Particles with Inertia in a Compressible Free Shear Layer," *Physics of Fluids A*, Vol. 3, No. 8, 1991, pp. 1915-1923.

[41]Melling, A., "Seeding Gas Flows for Laser Anemometry," *AGARD Advanced Instrumentation for Aero Engine Components*, Philadelphia, 1986, pp. 8.1-8.11.

[42]Hartman, J.R., Famil-Ghirha, J., Ring, M.A., and O'Neal, H.E., "Stoichiometry and Possible Mechanism of SiH_4-O_2 Explosions," *Combustion and Flame*, Vol. 68, 1987, pp. 43-56.

[43]Rogers, R.C., Weidner, E.H., and Bittner, R.D., "Quantification of Scramjet Mixing in the Hypervelocity Flow of a Pulse Facility," AIAA Paper 94-2518, June 1994.

[44]Taylor, G.I., and Maccoll, J.W., "The Air Pressure on a Cone Moving at High Speed," *Proc. Roy. Soc.*, (London) Ser. A, Vol. 139, 1933, pp. 278-311.

[45]Anderson, J.D., Jr., *Modern Compressible Flow with Historical Perspective*, 2nd Ed., McGraw-Hill, New York, 1990, pp. 301-303.

[46]Sims, J.L., "Tables for Supersonic Flow Around Right Circular Cones at Zero Angle of Attack," NASA SP-3004, 1964.

[47]Heijden, Ferdinand van der, *Image Based Measurement Systems: Object Recognition and Parameter Estimation*, John Wiley & Sons, New York, 1994, p. 52.

[48]Long, M.B., "Multidimensional Imaging in Combusting Flows by Lorentz-Mie, Rayleigh, and Raman Scattering," *Instrumentation for Flows with Combustion*, Taylor, A.M.K.P., (Edit.), Academic Press, San Diego, 1993, pp. 467-508.

[49]Mao, M., Riggins, D.W., and McClinton, C.R., "Numerical Simulation of Transverse Fuel Injection," NASP CR 1089, May 1990.

[50]Liscinsky, D.S., True, B., and Holdeman, J.D., "Effects of Initial Conditions on a Single Jet in Crossflow," AIAA Paper 95-2998, July 1995.

[51]Doeblin, E.O., *Measurement Systems: Application and Design*, 4th Ed., McGraw-Hill, 1990, pp. 58-60.

[52]Kwok, F.T., Andrew, P.L., Ng, W.F., and Schetz, J.A., "Experimental Investigation of a Supersonic Shear Layer with Slot Injection of Helium," AIAA Paper 90-0093, January 1990.

[53]Fuller, R.P., Wu, P.-K., Nejad, A.S., and Schetz, J.A., "Fuel-Vortex Interactions for Enhanced Mixing in Supersonic Flow," AIAA Paper 96-2661, July 1996.

Appendix A: Uncertainty Analysis

In any experimental investigation, measurements are made to determine a numerical value associated with some physical quantity. It is inevitable, that these measurements carry with them some degree of uncertainty. The "true" value is unknown, and the absolute error cannot be determined. However, statistical analysis and knowledge of the characteristics of the measurement process can often establish bounds on the error of a single measurement. These bounds determine the accuracy of the measurement technique.

The total error of a measurement is composed of two parts, the *bias* and the *imprecision*. The bias is also known as the *systematic error*. Since the systematic error is the same for each reading, it may be removed through calibration. Thus, only the error due to imprecision remains. The error due to imprecision is a random error. Since the error is, in general, different for each measurement, it cannot be removed. Therefore, we attempt to establish statistical bounds on the magnitude of the random error to determine the accuracy of the measurement.

Commercial instruments, such as pressure transducers, thermocouples, etc., come provided with a statement of the accuracy. However, specialized measurement systems are often composed of several components, each of which is subject to individual inaccuracy. The measurements obtained with each of the individual components are combined to compute other physical quantities. To establish error bounds on these computed quantities, each of the individual uncertainties of each components must be taken into account. This was the case with the current investigation. Each of the four probing measurements, P_{t2}, P_c, T_t, and X_{He} were combined to resolve α_{He}, P_t, M, u, P, T, and ρ. To predict the uncertainties in the resolved quantities for known uncertainties in the measured quantities, the following procedure, taken from Doeblin[51], was utilized.

Consider the resolved quantity, Q, where Q is a known function of the independent measurements of P_{t2}, P_c, T_t, and X_{He}.

$$Q = f(P_{t2}, P_c, T_t, X_{He})$$

Here, Q may represent either α_{He}, P_t, M, u, P, T, or ρ. Each of the measured quantities have uncertainties $\pm\Delta P_{t2}$, $\pm\Delta P_c$, $\pm\Delta T_t$, and $\pm\Delta X_{He}$, respectivley. It is assumed that these uncertainties represent the error bounds for 95% (19-to-1 odds) of the measurements. These errors will cause an error, ΔQ, in the computed result, Q.

$$Q \pm \Delta Q = f(P_{t2} \pm \Delta P_{t2}, P_c \pm \Delta P_c, T_t \pm \Delta T_t, X_{He} \pm \Delta X_{He})$$

By expanding the function f into a Taylor series and dropping the higher order terms, the uncertainty is estimated by the root-sum square formula:

$$E_{a,rss} = \sqrt{\left(\Delta P_{t2}\frac{\partial f}{\partial P_{t2}}\right)^2 + \left(\Delta P_c\frac{\partial f}{\partial P_c}\right)^2 + \left(\Delta T_t\frac{\partial f}{\partial T_t}\right)^2 + \left(\Delta X_{He}\frac{\partial f}{\partial X_{He}}\right)^2}$$

Since the data reduction involved a complex, iterative scheme, the partial derivatives in the above approximation could not be analytically evaluated. Instead, they were computed using a central difference approximation. The relative or percentage error, E_r is then given by

$$E_r = \frac{\Delta Q}{Q} \times 100 = \frac{100 E_{a,rss}}{Q}$$

The above procedure was utilized in a *jitter* program to compute the error bounds or uncertainties on each of the resolved quantities. The results are presented next.

As stated in Section 3.1.5, the facility control system can maintain the stagnation conditions, $P_{t,\infty}$ and $T_{t,\infty}$, within 1% of their nominal values. Furthermore, the helium supply system could maintain the injectant total pressure, $P_{t,j}$, within 2% of its nominal value.

The uncertainty of the helium concentration measurement was previously estimated by Kwok et al.[52] to be ±0.02 in mole fraction, and an estimated three percent uncertainty in the calibration curve fit and interpolation routine. Uncertainty realized in the static calibration technique was

subject to human error and could not be determined. However, these errors could be minimized with practice. A total uncertainty of ± 0.05 in the helium mole fraction, X_{He}, results in a total uncertainty of nearly 25% in the helium mass fraction, α_{He}. This makes the continuity check on the helium mass flow, $\int \alpha_{He} \rho u dA$, very difficult to establish accurately.

The uncertainty of the Pitot and cone-static pressure measurements were dominated by transducer accuracy, time response, and electrical drift and noise. The particular transducers used in these experiments were quoted as having an accuracy of 1%. Since each probe was allowed to rest at the measurement point for nearly a second before taking data, the error due to time response was assumed to be negligible.

The uncertainty of the total temperature measurement was estimated to be about 2% for flows with small total temperature gradients. The uncertainty was mainly due to insufficient venting of the gas through the probe, and heat losses through radiation and convection.

Each of these measurement uncertainties contributed to errors in the reduced values of Mach number, M, total pressure, P_t, static pressure, P, density, ρ, velocity, u, and static temperature, T. The propagation of the measurement uncertainties to these reduced values were estimated using the previously described procedure. The results are as follows.

	Uncertainty
P_t	$\pm 2.8\%$
M	$\pm 1.7\%$
u	$\pm 1.3\%$
P	$\pm 2.8\%$
ρ	$\pm 3.0\%$
T	$\pm 0.8\%$

Estimated uncertainties (19-to-1 odds) in the reduced quantities.

These estimated uncertainties represent the average values for all sets of probing measurements taken in the present study where the helium mass fraction was less than 1.0. Conditions not tested in this investigation may result in higher uncertainties. High concentrations of helium yields higher

uncertainties due to the dependence on the specific gas constant, R. These high uncertainties usually show up in the calculated density, ρ, and sound speed, c.

Another source of uncertainty results from inaccurate placement of the probes. The probe was traversed in the spanwise direction using a stepper motor. Therefore, the lateral placement of the probe was within 0.001 in/in of the true distance from the side wall. Vertical positioning of the probes was performed manually using a fixed scale attached to the tunnel test section. This scale had a spatial resolution of 0.1 in. The uncertainty in the vertical positioning of the probe was estimated to be within ± 0.025 in of the true distance from the wall surface at any given location. The effect of this misplacement on the uncertainty of the reduced quantities was prohibitively difficult to predict. However, this uncertainty in the probe position will, of course, increase the uncertainty in the computed quantities.

Appendix B: Data Reduction Codes

The basic codes used for data reduction in the gas sampling and probing techniques are presented here. They are written in C and were designed for compilation and execution on either a UNIX or MS-DOS based system. For the many FORTRAN users out there, I have avoided the use of memory address pointers, dynamic memory allocation, and "tricky" C conventions as much as was possible. Hence, they are simple number crunchers. These codes are first-run, "bare-bones" versions and are by no means elegant. More elegant and robust codes are currently being developed under Windows 95 which make full use of the power of C. These codes will include a user interface with error checking and analysis and will allow for multiple gas mixtures. These codes will be made available upon request at a later date.

The three codes presented here are *xcalibr8.c*, *xreduce.c*, and *meanflow.c*. The code *xcalibr8.c* is used to construct the calibration curve fits for the gas sampling probe and analyzer. The code *xreduce.c* is used to reduce the data obtained with the sampling probe and analyzer. Finally, the code *meanflow.c* is used to reduce the aerothermodynamic properties using the Pitot pressure, cone-static pressure, total temperature, and helium concentration measurements. Each code is preceded by a brief introduction and directions for proper usage. Detailed documentation within the code was not provided, since the codes are well-structured, highly readable, and self-explanatory.

PROGRAM	XCALIBR8.C
PROGRAMMER	Raymond Fuller
LANGUAGE	ANSI C
SYSTEM	MS-DOS or UNIX
DATE	August, 1996

This program is used to construct the least-squares curve fits for calibration of the gas analyzer. This particular code was designed for air-helium mixtures only. The code can handle any number of points per calibration mixture, number of calibrations mixtures, and calibration temperatures. Since, dynamic memory allocation was not used, recompilation is required any time one of these numbers are changed. These are globally defined constants at the top of the program. The program requires two input files containing the analyzer physical specifications and the empirical calibration data. The program will output two files, one containing the calibration constants and a another containing generated curve data with a Tecplot header.

To use the program, the user must first edit the constant definitions at the top of the program. The constant L is the number of data points taken per concentration level. This requires the same number for all concentration levels. This number is typically between 10 and 20. The constant M is the number of concentration levels sampled. For example, you might want to calibrate over the entire range of $X_{He} = 0.0$ to $X_{He} = 1.0$ in increments of 0.1 yielding 11 concentration levels. Finally, the constant N is the number of calibration temperatures. This number is typically one, unless you expect large temperature fluctuations in the actual measurements. If so, generally, only three calibration temperatures encompassing the entire range of expected measurement are required. After setting the constants to the desired values, simply recompile and you are ready to go.

The program will require a probe data file given the name *xprobe.dat*. This file should contain the probe physical specifications beginning at the first line with the following format:

R_series	5.000E+01	[ohms]
R_sensor	9.060E+00	[ohms]
l_film	1.016E-03	[m]
d_film	5.080E-05	[m]
A_orifice	2.919E-07	[m$\hat{2}$]
A_sample	1.171E-05	[m$\hat{2}$]
R_zero	4.980E+00	[ohms]
R_diff	1.300E+00	[ohms]
R_cable	0.010E+00	[ohms]

Be sure to include the labels and units. Although the program does not use them, it will attempt to read them. The values are defined as follows:

R_series	= anemometer bridge series resistance
R_sensor	= hot-film sensor operating resistance
l_film	= length of hot-film sensor
d_film	= diameter of hot-film sensor
A_orifice	= area of choked orifice
A_sample	= area of gas analyzer sampling channel at sensor plane
R_zero	= resistance of sensor at 0 degrees Celsius
R_diff	= change in resistance between 0 and 100 degrees Celsius
R_cable	= anemometer-to-sensor cable resistance

Of course, the program will require the calibration data. For N calibration temperatures, M calibration levels, and L data points per calibration level, the file format is as follows. Each line should contain the sampling pressure in psia, the sampling temperature in K, the hot-film potential in volts, and the helium mole fraction separated by spaces only. Here is an example, for $L = 3$, $N = 3$, and $M = 2$, the data file will look something like this:

50.0	300.0	4.5	0.0
25.0	300.0	3.5	0.0
15.0	300.0	2.5	0.0
50.0	300.0	5.5	0.3
25.0	300.0	4.5	0.3
15.0	300.0	3.5	0.3
50.0	300.0	6.5	0.9
25.0	300.0	5.5	0.9
15.0	300.0	4.5	0.9
50.0	350.0	5.5	0.0
25.0	350.0	4.5	0.0
15.0	350.0	3.5	0.0
50.0	350.0	6.5	0.3

25.0	350.0	5.5	0.3
15.0	350.0	4.5	0.3
50.0	350.0	7.5	0.9
25.0	350.0	6.5	0.9
15.0	350.0	5.5	0.9

The numbers are hypothetical, but the ordering is correct. By examining this table and the subroutine, *input_data*, scheme should be quite clear. If not, take a look at this:

P_1	T_1	V	X_1
P_2	T_1	V	X_1
P_3	T_1	V	X_1
P_1	T_1	V	X_2
P_2	T_1	V	X_2
P_3	T_1	V	X_2
P_1	T_1	V	X_3
P_2	T_1	V	X_3
P_3	T_1	V	X_3
P_1	T_2	V	X_1
P_2	T_2	V	X_1
P_3	T_2	V	X_1
P_1	T_2	V	X_2
P_2	T_2	V	X_2
P_3	T_2	V	X_2
P_1	T_2	V	X_3
P_2	T_2	V	X_3
P_3	T_2	V	X_3

where P (pressure), T (temperature), and X (helium mole fraction) are ideally the controlled variables and V (hot-film voltage) is the measured variable. It is not necessary that all the P_is, for constant i, be exactly the same, as it will not affect the calibration. The T_is for constant i should be as uniform as possible, as a large variation will cause calibration inaccuracies. The X_is for constant i should be exactly the same.

After creating the necessary files, just run the executable. The program will create the file *xcalibr8.out* which will contain the calibration constants for use with the data reduction program *xreduce.c*. Just leave this file alone. It is already formatted for proper use. There will also be a file called *xcalibr8.tec*. This is a file containing a list of data for plotting the calibration data and curve fits. If you are a Tecplot user, then you are all set. Simply *preplot* the data file and your on your way. Otherwise, you are on your own.

```c
#include <stdlib.h>
#include <stdio.h>
#include <math.h>

#define L 24   /*  L = Num. of data points per concentration   */
#define M 9    /*  M = Num. of concentration levels             */
#define N 1    /*  N = Num. of temperature levels               */
#define PI 3.141592654

/****************************************
DECLARATION OF SUBROUTINES AND FUNCTIONS
****************************************/

void   probe_data     (float[]);
void   input_data      (float[][M][N],float[][M][N],
    float[][M][N],float[][M][N]);
float average_temp   (float[][M][N], int);
float gas_constant   (float);
float heat_ratio      (float, float, float);
float conductivity   (float, float);
float viscosity       (float, float, float);
void   governing_eq   (float, float, float, float[], float[]);
void   curve_fit       (float[][M][N],float[][M][N],
    float[][M][N],float[][M][N],float[]);
void   plot_data       (float[]);

/******************
MAIN CALLING ROUTINE
******************/

int main ()
{
    float  V[L][M][N], Pt[L][M][N];
    FLOAT  Tt[L][M][N], X[L][M][N], D[9];

    probe_data(D);

    input_data(Pt, Tt, V, X);

    curve_fit(Pt, Tt, V, X, D);

    plot_data(D);

    return 0;
}

/***************************************************
SUBROUTINE TO READ IN PROBE PHYSICAL SPECIFICATIONS
***************************************************/

void probe_data(float D[])
```

```
{
    FILE *fp;
    char string1[10], string2[10];
    int i;

    if ((fp = fopen("xprobe.dat", "r")) == NULL) {
        printf ("\nMISSING FILE:  XPROBE.DAT\n");
        exit (1);
    }

    for (i = 0; i < 9; i++)
        fscanf (fp, "%s%f%s%*c",
            &string1, &D[i], &string2);

    fclose (fp);

}

/*****************************************
SUBROUTINE TO READ IN THE CALIBRATION DATA
*****************************************/

void input_data(float Pt[][M][N], float Tt[][M][N],
    float V[][M][N], float X[][M][N])
{
    FILE *fp;
    int i, j, k;

    if ((fp = fopen("xcalibr8.exp", "r")) == NULL) {
        printf ("\nMISSING FILE:  XCALIBR8.EXP\n");
        exit (1);
    }

    for (k = 0; k < N; k++) {
        for (j=0; j < M; j++) {
            for (i=0; i < L; i++) {
                fscanf(fp, "%f %f %f %f%*c",
                    &Pt[i][j][k], &Tt[i][j][k],
                        &V[i][j][k], &X[i][j][k]);
            }
        }
    }
    fclose(fp);
}

/*******************************************************
FUNCTION TO COMPUTE AVERAGE CALIBRATION TEMPERATURE
*******************************************************/

float average_temp(float Tt[][M][N], int k)
{
```

```
    int i, j;
    float sum=0.0, T_avg;

    for (i=0; i < L; i++) {
        for (j=0; j < M; j++)
        sum += Tt[i][j][k];
    }
    T_avg = sum / (L * M);

    return(T_avg);
}


/*****************************************
FUNCTION TO COMPUTE SPECIFIC GAS CONSTANT
*****************************************/

float gas_constant(float X)
{
    float MW;

    MW = X * 4.0026 + (1.0 − X) * 28.97;

    return (8314.0 / MW);
}


/*****************************************
FUNCTION TO COMPUTE RATIO OF SPECIFIC HEATS
*****************************************/

float heat_ratio(float X, float R, float T)
{
    float gamma, Cp, Cp_air, Cp_He, MW;
    float MW_air, MW_He, f1, f2, f3, f4;

    MW_air  = 28.97;
    MW_He   = 4.0026;
    Cp_He   = 5192.6;

    f1   =   0.2811E+02;
    f2   =   0.1967E−02 * T;
    f3   =   0.4802E−05 * T * T;
    f4   = −0.1966E−09 * T * T * T;
    Cp_air  = (f1 + f2 + f3 + f4) * 1000.0 / MW_air;

    MW       = X * MW_He + (1.0 − X) * MW_air;

    Cp  = (MW_He * X * Cp_He + MW_air * (1.0 − X) * Cp_air) / MW;

    gamma = Cp / (Cp − R);

    return (gamma);
```

```
}

/*************************************
FUNCTION TO COMPUTE THERMAL CONDUCTIVITY
*************************************/

float conductivity(float X, float T)
{
    float f0, f1, f2, f3, f4, f5;
    float k, k_air, k_He;

    f0 =    1.61344E−04;
    f1 =    8.89970E−05 * T;
    f2 =    3.85599E−08 * T * T;
    f3 = −2.39332E−10 * T * T * T;
    f4 =    3.48891E−13 * T * T * T * T;
    f5 = −1.84858E−16 * T * T * T * T * T;

    k_air = f0 + f1 + f2 + f3 + f4 + f5;

    f0 =    4.33185E−02;
    f1 =    1.23854E−04 * T;
    f2 =    2.77149E−06 * T * T;
    f3 = −1.11774E−08 * T * T * T;
    f4 =    1.81601E−11 * T * T * T * T;
    f5 = −1.03892E−14 * T * T * T * T * T;

    k_He = f0 + f1 + f2 + f3 + f4 + f5;

    f1 = k_air * (1.0 − X) + k_He * X;
    f2 = k_air * k_He;
    f3 = (1.0 − X) * sqrt(k_He) + X * sqrt(k_air);

    k = 0.5 * (f1 + f2 / (f3 * f3));

    return (k);
}

/**************************
FUNCTION TO COMPUTE VISCOSITY
**************************/

float viscosity(float X, float T, float P)
{
    float f0, f1, f2, f3, f4, f5, f6, f7;
    float mu, mu_air, mu_He, D12;

    f0 = −1.31554E−06;
    f1 =    9.53265E−08 * T;
    f2 = −1.50660E−10 * T * T;
    f3 =    2.41737E−13 * T * T * T;
```

```
    f4 =  -2.58576E-16 * T * T * T * T;
    f5 =   1.26849E-19 * T * T * T * T * T;

    mu_air = f0 + f1 + f2 + f3 + f4 + f5;

    f0 =  -4.56080E-06;
    f1 =   2.05152E-07 * T;
    f2 =  -8.89707E-10 * T * T;
    f3 =   2.41714E-12 * T * T * T;
    f4 =  -3.20720E-15 * T * T * T * T;
    f5 =   1.63060E-18 * T * T * T * T * T;

    mu_He = f0 + f1 + f2 + f3 + f4 + f5;

    f1  = 7.1E-05;
    f2  = pow((T / 293.15), 1.69);
    f3  = P / 14.696;
    D12 = f1 * f2 / f3;
    if (X == 0.0)
        mu = mu_air;
    else {
        f1 = X * X;
        f2 = (1.0 - X) * (1.0 - X);
        f3 = f1 / mu_He;
        f4 = f2 / mu_air;
        f5 = 1.385 * X * (1.0 - X) * 8314.0 * T;
        f6 = f5 / (P * 4.0026 * D12 / 1.4505E-04);
        f7 = f5 / (P * 28.97 * D12 / 1.4504E-04);
        mu = (f1 / (f3 + f6)) + (f2 / (f4 + f7));
    }
    return (mu);
}


/***********************************
FUNCTION TO COMPUTE HOT-FILM VOLTAGE
***********************************/

void governing_eq(float Pt, float Tt, float X,
    float D[], float solution[])
{
    float k, mu, R, gamma, V, alpha, beta;
    float T_film, l_film, d_film, A_orifice, A_sample;
    float R_series, R_sensor, R_zero, R_diff, R_cable;
    float a, a1, a2, a3, b, b1, b2, b3, b4, b5;

    R_series  = D[0];    /*  anemometer bridge resistance  [ohms]   */
    R_sensor  = D[1];    /*  sensor operating resistance    [ohms]   */
    l_film    = D[2];    /*  active length of hot-film      [m]      */
    d_film    = D[3];    /*  diameter of hot-film           [m]      */
    A_orifice = D[4];    /*  area of choked orifice         [m^2]    */
    A_sample  = D[5];    /*  area of sampling plane          [m^2]    */
```

```
    R_zero     = D[6];     /*  sensor resistance at 0 deg. C  [ohms]  */
    R_diff     = D[7];     /*  res. @ 100 deg − res. @ 0 deg  [ohms]  */
    R_cable    = D[8];     /*  added cable resistance         [ohms]  */

    alpha = solution[3];
    beta  = solution[4];

    T_film     = ((R_sensor − R_zero) * 100.0 / R_diff) + 273.15;

    R           = gas_constant(X);
    gamma       = heat_ratio(X, R, Tt);
    k           = conductivity(X, Tt);
    mu          = viscosity(X, Tt, Pt);

    Pt          = Pt / 1.4504E−4;

    a1          = R_series + R_sensor + R_cable;
    a3          = a1 * a1 / R_sensor;
    a2          = PI * l_film * k * (T_film − Tt);
    a           = a3 * a2;

    b1          = d_film / mu;
    b2          = Pt / sqrt(Tt);
    b3          = (A_orifice / A_sample) * sqrt(gamma / R);
    b4          = 2.0 / (gamma + 1.0);
    b5          = (gamma + 1.0) / (2.0 * (gamma − 1.0));
    b           = b1 * b2 * b3 * pow(b4, b5);

    V           = sqrt(alpha * a * pow(b, beta));

    solution[0] = V;
    solution[1] = a;
    solution[2] = b;
}

/*********************************************
SUBROUTINE TO PERFORM LEAST SQUARES CURVE FIT
*********************************************/

void curve_fit(float Pt[][M][N], float Tt[][M][N],
    float V[][M][N], float X[][M][N], float D[])
{
    FILE *fp;
    int i, j, k;
    float P1, T1, V1, X1, a, b, alpha, beta, solution[5];
    float x, y, xx, xy;

    fp = fopen("xcalibr8.out", "w");

    solution[3] = 0.0;
    solution[4] = 0.0;
```

```c
    for (k = 0; k < N; k++) {
        T1 = average_temp(Tt, k);
        for (j = 0; j < M; j++) {
            X1 = X[1][j][k];
            xx = 0.0;
            xy = 0.0;
            x  = 0.0;
            y  = 0.0;
            for (i = 0; i < L; i++) {
                V1 = V[i][j][k];
                P1 = Pt[i][j][k];
                governing_eq(P1, T1, X1, D, solution);
                a = solution[1];
                b = solution[2];
                x  += log(b);
                y  += log(V1 * V1 / a);
                xx += log(b) * log(b);
                xy += log(b) * log(V1 * V1 / a);
            }
            alpha = exp((xx * y - xy * x) / (L * xx - x * x));
            beta  = (L * xy - x * y) / (L * xx - x * x);

            fprintf (fp, "%6.1f%9.2f%12.5f%11.5f\n",
                T1, X1, alpha, beta);
        }
    }
    fclose (fp);
}


/*********************************************
SUBROUTINE TO GENERATE DATA FOR TECPLOT FILE
*********************************************/

void plot_data(float D[])
{
    FILE   *infp, *outfp;
    float  V, P, Pe, Pmin, Pmax, dP;
    float  T[M][N], X[M][N], alpha[M][N], beta[M][N], solution[5];
    char   inbuff[80];
    int    j, k;

    printf ("\n\nEnter min. pressure to plot (psia).");
    printf ("\n\n--> ");
    scanf  ("%f", &Pmin);

    printf ("\n\nEnter max. pressure to plot (psia).");
    printf ("\n\n--> ");
    scanf  ("%f", &Pmax);

    dP = (Pmax - Pmin) / 1000.0;
```

```c
        infp  = fopen("xcalibr8.out", "r");
        outfp = fopen("xcalibr8.tec", "w");

        for (k = 0; k < N; k++) {
            for (j = 0; j < M; j++) {
                fscanf(infp, "%f%f%f%f%*c",
                    &T[j][k], &X[j][k], &alpha[j][k], &beta[j][k]);
            }
        }

        for (k = 0; k < N; k++) {
            for (P = Pmin; P <= Pmax; P += dP) {
                fprintf (outfp, "\n%4.2f", P);
                for (j = 0; j < M; j++) {
                    solution[3] = alpha[j][k];
                    solution[4] = beta[j][k];
                    governing_eq(P,T[j][k],X[j][k],D,solution);
                    V = solution[0];
                    fprintf (outfp, "%8.3f", V);
                }
            }
        }
        fclose (infp);
        fclose (outfp);
}
```

PROGRAM	XREDUCE.C
PROGRAMMER	Raymond Fuller
LANGUAGE	ANSI C
SYSTEM	MS-DOS or UNIX
DATE	August, 1996

This program is used to reduce the data obtained with the gas sampling probe and analyzer. This code will take the input values of hot-film voltage, V, total pressure, P_t, and total temperature, T_t, and determine the corrsponding helium mole and mass fractions. The code must be supplied with three data files; 1) the gas anayzer physical data, *xprobe.dat*, 2) the calibration file, *xcalibr8.out*, and 3) the experimental data to be reduced, *xreduce.exp*. The gas analyzer physical data file *xprobe.dat* should be the same as that used to generate the calibration file *xcalibr8.out*. The experimental data can be of any length, since the data reduction is point-by-point. The format of the experimental data file, *xreduce.exp*, should be as follows:

z_1	y_1	V_1	P_1	T_1
z_2	y_2	V_2	P_2	T_2
z_3	y_3	V_3	P_3	T_3
...	...	...	...	...

where z and y are the spatial coordinates of the measurement.

To run the program, simply run the executable of *xreduce* with the three necessary files described above. The program will generate an ouput file containing the helium concentration in the following format:

z_1	y_1	$X_{He,1}$	$\alpha_{He,1}$
z_2	y_2	$X_{He,2}$	$\alpha_{He,2}$
z_3	y_3	$X_{He,3}$	$\alpha_{He,3}$
...	...	...	...

where X_{He} is the helium mole fraction, and α_{He} is the helium mass fraction.

```c
#include <stdlib.h>
#include <stdio.h>
#include <math.h>

#define PI  3.141592654

/*****************************************
 DECLARATION OF SUBROUTINES AND FUNCTIONS
 *****************************************/

void   probe_data      (float[]);
float  gas_constant    (float);
float  heat_ratio      (float, float, float);
float  conductivity    (float, float);
float  viscosity       (float, float, float);
float  film_voltage    (float, float, float, float, float, float[]);
void   bracket         (float[], float[], float[], float, float,
       float, float[]);
float  b_interpolate   (float[], float[], float[], float, float);
float  l_interpolate   (float[], float[], float);
float  mass_fraction   (float);

/*******************
 MAIN CALLING ROUTINE
 *******************/

int main ()
{
    FILE     *infp, *outfp;
    float    z, y, V, Pt, Tt, X, C;
    float    XXX[4], TTT[4], VVV[4], D[9];
    int      i;
    char     inbuff[80];

    probe_data(D);

    if ((infp = fopen("xreduce.exp", "r")) == NULL) {
        printf ("\nMissing input file!\n");
        exit (1);
    }

    outfp = fopen("xreduce.out", "w");

    while ((fgets(inbuff, 80, infp)) != NULL) {
        sscanf(inbuff, "%f%f%f%f%f%*c", &z, &y, &V, &Pt, &Tt);
        bracket(XXX, TTT, VVV, V, Pt, Tt, D);
        if ((TTT[0] == TTT[2]) && (TTT[1] == TTT[3]))
            X = l_interpolate(XXX, VVV, V);
        else
            X = b_interpolate(XXX, TTT, VVV, V, Tt);
        C = mass_fraction(X);
```

```c
        fprintf (outfp, "\n%5.3f%9.3f%9.3f%10.4f", z, y, X, C);
        printf ("\n%5.3f%9.3f%9.3f%10.4f", z, y, X, C);
    }

    fclose(infp);
    fclose(outfp);

    return 0;
}

/*************************************************
SUBROUTINE TO READ IN PROBE PHYSICAL SPECIFICATIONS
*************************************************/

void probe_data(float D[])
{
    FILE *fp;
    char string1[10], string2[10];
    int i;

    if ((fp = fopen("xprobe.dat", "r")) == NULL) {
        printf ("\nMISSING FILE:  XPROBE.DAT\n");
        exit (1);
    }
    for (i = 0; i < 9; i++)
        fscanf (fp, "%s%f%s%*c", &string1, &D[i], &string2);

    fclose (fp);
}

/***************************************
FUNCTION TO COMPUTE SPECIFIC GAS CONSTANT
***************************************/

float gas_constant(float X)
{
    float MW;

    MW = X * 4.0026 + (1.0 - X) * 28.97;

    return (8314.0 / MW);
}

/*****************************************
FUNCTION TO COMPUTE RATIO OF SPECIFIC HEATS
*****************************************/

float heat_ratio(float X, float R, float T)
{
    float gamma, Cp, Cp_air, Cp_He, MW;
    float MW_air, MW_He, f1, f2, f3, f4;
```

```
    MW_air  =  28.97;
    MW_He   =  4.0026;
    Cp_He   =  5192.6;

    f1   =   0.2811E+02;
    f2   =   0.1967E−02 * T;
    f3   =   0.4802E−05 * T * T;
    f4   =  −0.1966E−09 * T * T * T;
    Cp_air  =  (f1 + f2 + f3 + f4) * 1000.0 / MW_air;

    MW  =  X * MW_He + (1.0 − X) * MW_air;

    Cp   =  (MW_He * X * Cp_He + MW_air * (1.0 − X) * Cp_air) / MW;

    gamma =  Cp / (Cp − R);

    return (gamma);
}


/*****************************************
FUNCTION TO COMPUTE THERMAL CONDUCTIVITY
*****************************************/

float conductivity(float X, float T)
{
    float f0, f1, f2, f3, f4, f5;
    float k, k_air, k_He;

    f0  =   1.61344E−04;
    f1  =   8.89970E−05 * T;
    f2  =   3.85599E−08 * T * T;
    f3  =  −2.39332E−10 * T * T * T;
    f4  =   3.48891E−13 * T * T * T * T;
    f5  =  −1.84858E−16 * T * T * T * T * T;

    k_air =  f0 + f1 + f2 + f3 + f4 + f5;

    f0  =   4.33185E−02;
    f1  =   1.23854E−04 * T;
    f2  =   2.77149E−06 * T * T;
    f3  =  −1.11774E−08 * T * T * T;
    f4  =   1.81601E−11 * T * T * T * T;
    f5  =  −1.03892E−14 * T * T * T * T * T;

    k_He =  f0 + f1 + f2 + f3 + f4 + f5;

    f1 = k_air * (1.0 − X) + k_He * X;
    f2 = k_air * k_He;
    f3 = (1.0 − X) * sqrt(k_He) + X * sqrt(k_air);
```

```
    k = 0.5 * (f1 + f2 / (f3 * f3));

    return (k);
}


/***************************
FUNCTION TO COMPUTE VISCOSITY
***************************/

float viscosity(float X, float T, float P)
{
    float f0, f1, f2, f3, f4, f5, f6, f7;
    float mu, mu_air, mu_He, D12;

    f0 = -1.31554E-06;
    f1 =  9.53265E-08 * T;
    f2 = -1.50660E-10 * T * T;
    f3 =  2.41737E-13 * T * T * T;
    f4 = -2.58576E-16 * T * T * T * T;
    f5 =  1.26849E-19 * T * T * T * T * T;

    mu_air = f0 + f1 + f2 + f3 + f4 + f5;

    f0 = -4.56080E-06;
    f1 =  2.05152E-07 * T;
    f2 = -8.89707E-10 * T * T;
    f3 =  2.41714E-12 * T * T * T;
    f4 = -3.20720E-15 * T * T * T * T;
    f5 =  1.63060E-18 * T * T * T * T * T;

    mu_He = f0 + f1 + f2 + f3 + f4 + f5;

    f1  = 7.1E-05;
    f2  = pow((T / 293.15), 1.69);
    f3  = P / 14.696;
    D12 = f1 * f2 / f3;
    if (X == 0.0)
        mu = mu_air;
    else {
        f1 = X * X;
        f2 = (1.0 - X) * (1.0 - X);
        f3 = f1 / mu_He;
        f4 = f2 / mu_air;
        f5 = 1.385 * X * (1.0 - X) * 8314.0 * T;
        f6 = f5 / (P * 4.0026 * D12 / 1.4505E-04);
        f7 = f5 / (P * 28.97 * D12 / 1.4504E-04);
        mu = (f1 / (f3 + f6)) + (f2 / (f4 + f7));
    }
    return (mu);
}
```

```
/*********************************
FUNCTION TO COMPUTE HOT-FILM VOLTAGE
*********************************/

float film_voltage(float X, float Tt, float Pt,
    float alpha, float beta,float D[]) {

    float k, mu, R, gamma, V;
    float T_film, l_film, d_film, A_orifice, A_sample;
    float R_series, R_sensor, R_zero, R_diff, R_cable;
    float a, a1, a2, a3, b, b1, b2, b3, b4, b5;

    R_series  = D[0];    /*  anemometer bridge resistance   [ohms]  */
    R_sensor  = D[1];    /*  sensor operating resistance    [ohms]  */
    l_film    = D[2];    /*  active length of hot-film      [m]     */
    d_film    = D[3];    /*  diameter of hot-film           [m]     */
    A_orifice = D[4];    /*  area of choked orifice         [m^2]   */
    A_sample  = D[5];    /*  area of sampling plane         [m^2]   */
    R_zero    = D[6];    /*  sensor resistance at 0 deg. C  [ohms]  */
    R_diff    = D[7];    /*  res. @ 100 deg - res. @ 0 deg  [ohms]  */
    R_cable   = D[8];    /*  added cable resistance         [ohms]  */

    T_film    = ((R_sensor - R_zero) * 100.0 / R_diff) + 273.15;

    R         = gas_constant(X);
    gamma     = heat_ratio(X, R, Tt);
    k         = conductivity(X, Tt);
    mu        = viscosity(X, Tt, Pt);

    Pt        = Pt / 1.4504E-4;

    a1        = R_series + R_sensor + R_cable;
    a3        = a1 * a1 / R_sensor;
    a2        = PI * l_film * k * (T_film - Tt);
    a         = a3 * a2;

    b1        = d_film / mu;
    b2        = Pt / sqrt(Tt);
    b3        = (A_orifice / A_sample) * sqrt(gamma / R);
    b4        = 2.0 / (gamma + 1.0);
    b5        = (gamma + 1.0) / (2.0 * (gamma - 1.0));
    b         = b1 * b2 * b3 * pow(b4, b5);

    V         = sqrt(alpha * a * pow(b, beta));

    return (V);
}


/*********************************
SUBROUTINE TO BRACKET CONCENTRATION
*********************************/
```

```c
void bracket(float XXX[], float TTT[], float VVV[],
    float V, float Pt, float Tt, float D[])
{
    FILE      *fp;
    float     CTt, CX, alpha, beta, test_V;
    char      inbuff[80];
    int       i, hiflag = 0, lowflag = 0;
    int lowflag01, lowflag23, hiflag01, hiflag23;

    if ((fp = fopen("xcalibr8.out", "r")) == NULL) {
        printf ("\nMISSING FILE:  XCALIBR8.OUT\n");
        exit (1);
    }

    while (fgets(inbuff, 80, fp) != NULL) {
        sscanf(inbuff, "%f%f%f%f%*c",
            &CTt, &CX, &alpha, &beta);
        if (CTt <= Tt) {
            TTT[0]  = CTt;
            TTT[1]  = CTt;
            lowflag = 1;
        }
        if ((hiflag == 0) && (CTt >= Tt)) {
            TTT[2]  = CTt;
            TTT[3]  = CTt;
            hiflag  = 1;
        }
    }
    if (lowflag == 0) {
        TTT[0] = TTT[2];
        TTT[1] = TTT[3];
    }
    if (hiflag == 0) {
        TTT[2] = TTT[0];
        TTT[3] = TTT[1];
    }
    fseek (fp, 0L, SEEK_SET);

    lowflag01 = 0;
    lowflag23 = 0;
    hiflag01  = 0;
    hiflag23  = 0;

    while (fgets(inbuff, 80, fp) != NULL) {
        sscanf(inbuff, "%f%f%f%f%*c",
            &CTt, &CX, &alpha, &beta);
        if (CTt == TTT[0]) {
            test_V = film_voltage (CX, CTt, Pt, alpha, beta, D);
            if ((lowflag01 == 0) && (test_V <= V)) {
                VVV[0] = test_V;
```

```
                    XXX[0] = CX;
                }
            if ((hiflag01 == 0) && (test_V >= V)) {
                    VVV[1]     = test_V;
                    XXX[1]     = CX;
                    hiflag01  = 1;
                    lowflag01 = 1;
                }
        }

        if (CTt == TTT[2]) {
                test_V = film_voltage (CX, CTt, Pt, alpha, beta, D);
                if ((lowflag23 == 0) && (test_V <= V)) {
                    VVV[2] = test_V;
                    XXX[2] = CX;
                }
                if ((hiflag23 == 0) && (test_V >= V)) {
                    VVV[3]     = test_V;
                    XXX[3]     = CX;
                    hiflag23  = 1;
                    lowflag23 = 1;
                }
            }
        }
    }
    fclose(fp);
}

/ **************************************************************
FUNCTION TO INTERPOLATE CONCENTRATION BETWEEN BRACKETED VALUES
THIS IS THE BI-LINERAR INTERPOLATION ROUTINE FOR MULTIPLE
CALIBRATION TEMPERATURES
************************************************************** /

float b_interpolate(float XXX[], float TTT[], float VVV[],
    float V, float T)
{
    int    i, j, k, p ,n;
    float m, temp, a[5][6], y[5], X;

    n = 4;

    for (i = 1; i <= 4; i++) {
        a[i][1] = TTT[i-1];
        a[i][2] = VVV[i-1];
        a[i][3] = VVV[i-1] * TTT[i-1];
        a[i][4] = 1.0;
        a[i][5] = XXX[i-1];
    }
    for (i = 1; i <= (n-1); i++) {
        p = i;
        while (a[p][i] == 0)
```

```
            p++;
        if (p > n) {
            /* POINT IS BELOW CALIBRATION CURVES */
        }
        if (p != i) {
            for (k = 1; k <= (n+1); k++) {
                temp = a[p][k];
                a[p][k] = a[i][k];
                a[i][k] = temp;
            }
        }
        for (j = (i+1); j <= n; j++) {
            m = a[j][i] / a[i][i];
            for (k = 1; k <= (n+1); k++)
                a[j][k] = a[j][k] - m * a[i][k];
        }
    }
    if (a[n][n] == 0) {
        printf ("\nNo unique solution exists");
        exit (1);
    }
    if (p > n)
        X = 0.0;
    else {
        y[n] = a[n][n+1] / a[n][n];
        temp = 0.0;
        i = n-1;
        do {
            for (j = (i+1); j <=n; j++)
                temp = temp + a[i][j] * y[j];
            y[i] = (a[i][n+1] - temp) / a[i][i];
            i = i-1;
            temp = 0.0;
        }
        while (i > 0);

        X = y[1] * T + y[2] * V + y[3] * V * T + y[4];
    }
    return (X);
}

/************************************************************
FUNCTION TO INTERPOLATE CONCENTRATION BETWEEN BRACKETED VALUES
THIS IS THE LINERAR INTERPOLATION ROUTINE FOR A SINGLE
CALIBRATION TEMPERATURE
************************************************************/

float l_interpolate(float XXX[], float VVV[], float V)
{
    float x, y, m, b;
```

```
    if (VVV[2] != VVV[1]) {
        m = (XXX[2] - XXX[1]) / (VVV[2] - VVV[1]);
        x = V - VVV[1];
        b = XXX[1];
        y = m * x + b;
    }
    else
        y = 0.0;

    if (y < 0.0)
        y = 0.0;

    return(y);
}


/**************************************************
FUNCTION TO CONVERT MOLE FRACTION TO MASS FRACTION
**************************************************/

float mass_fraction(float X)
{
    float MW, MW_He, MW_air, C;

    MW_He  = 4.0026;
    MW_air = 28.97;

    MW = X * MW_He + (1.0 - X) * MW_air;

    C = X * MW_He  / MW;

    return (C);
}
```

PROGRAM	MEANFLOW.C
PROGRAMMER	Raymond Fuller
LANGUAGE	ANSI C
SYSTEM	MS-DOS or UNIX
DATE	August, 1996

This program is used to compute the aerothermodynamic data for the measured values of Pitot pressure, $P_{t,2}$, cone-static pressure, P_c, total temperature, T_t, and helium mole fraction, X_{He}. Furthermore, the output data will be nondimensionalized using the instantaneous stagnation conditions in the tunnel plenum chamber. The data reduction algorithm was explained in detail in Chapter 5. This program requires two data files; 1) the cone-flow data file, *coneflow.dat*, and 2) the experimental data file with a name specified by the user at run time. The program will compute those values listed in Chapter 5, and generate two output files; 1) the dimensional data in *mean.out*, and 2) the nondimensional data in a data file with a name specified by the user at run time. The experimental input data file must have the following format:

z	y	$P_{t,2}$	P_c	T_t	X_{He}
$P_{t,\infty,1}$	$P_{t,\infty,2}$	$P_{t,\infty,3}$	$T_{t,\infty,1}$	$T_{t,\infty,2}$	$T_{t,\infty,3}$

where $P_{t,\infty,1}$ and $T_{t,\infty,1}$ are plenum chamber stagnation conditions when the $P_{t,2}$ measurement was taken, where $P_{t,\infty,2}$ and $T_{t,\infty,2}$ are plenum chamber stagnation conditions when the P_c measurement was taken, where $P_{t,\infty,3}$ and $T_{t,\infty,3}$ are plenum chamber stagnation conditions when the T_t measurement was taken. Thus, every point in the measurement grid with the coordinates (x, y) will require two lines of data, as shown above. The data file can have any length since the reduction is point-by-point. To use the code simply run the executable by typing the following at the command prompt:

meanflow <input file> <output file>

where <input file> is the name of the experimental data file with the above format, and <output file> is the name of the output file where the nondimensional data will be stored.

```c
#include <stdlib.h>
#include <stdio.h>
#include <math.h>

#define PI 3.141592654
#define h  1.200

/*****************************************
DECLARATION OF SUBROUTINES AND FUNCTIONS
*****************************************/

void   coneflow_data  (float[], float[], float[]);
float  gas_constant    (float);
float  heat_ratio      (float, float, float);
float  pressure_ratio (float, float);
float  temp_ratio      (float, float);
void   bracket          (float[], float[], float[], float, float,
    float[], float[], float[]);
float  interpolate     (float[], float[], float[], float, float);
float  mach_number      (float, float, float[], float[], float[]);
void   nondimension    (float[], float, float[], float[]);
float  alt_mach_number();
float  Rayleigh        (float, float);
int    verify_shock    (float, float, float[], float[]);
void   reduce_data     (float, float, float, float, float[],
    float[], float[], float[]);

/******************
MAIN CALLING ROUTINE
******************/

void main (int argc, char *argv[])
{
    FILE   *infp, *outfp1, *outfp2;
    float  z, y, Pt2, Pc, Tt, X, M0, D, solution[8], ratios[8];
    float  CM[4000], Cg[4000], CPP[4000];
    float  M1, Pt1, P1, T1, U1, rho1, a1, gamma1;
    float  Pt0[3], Tt0[3], Ptj[3];
    float  AvgPtj, AvgPt0;
    float  M1M0, Pt1Pt0, P1P0, T1T0, U1U0, rho1rho0, a1a0;
    float  Tt1Tt0, PtjPt0, zD, yD;
    float  MW, MW_He, MW_air, C;
    char   inbuff[80];
    int    i;

    clrscr();
    if (argc < 2) {
        printf("\n\nMust specify input file and output file!");
        printf("\n\n     meanflow <input file> <output file>");
        printf("\n\n\n");
        exit(1);
```

```
}
if ((infp = fopen(argv[1], "r")) == NULL) {
    printf ("\nInput file not found!\n");
    exit (1);
}
outfp1 = fopen("mean.out", "w");
outfp2 = fopen(argv[2], "w");

coneflow_data(CM, Cg, CPP);

fgets(inbuff, 80, infp);
sscanf(inbuff, "%f%*c", &M0);

fgets(inbuff, 80, infp);
sscanf(inbuff, "%f%*c", &D);

while (fgets(inbuff, 80, infp) != NULL) {
    sscanf(inbuff, "%f%f%f%f%f%f%*c",
        &z, &y, &Pt2, &Pc, &Tt, &X);
    fgets(inbuff, 80, infp);
    sscanf(inbuff, "%f%f%f%f%f%f%f%f%f%*c",
        &Pt0[0], &Pt0[1], &Pt0[2],
        &Tt0[0], &Tt0[1], &Tt0[2],
        &Ptj[0], &Ptj[1], &Ptj[2]);

    /****   INPUT CONVERSIONS   ****/

    Tt = (Tt − 32.0) * (5.0 / 9.0) + 273.15;
    for (i = 0; i <= 2; i++)
        Tt0[i] = (Tt0[i]−32.0)*(5.0/9.0)+273.15;

    AvgPtj = (Ptj[0] + Ptj[1] +Ptj[2]) / 3.0;
    AvgPt0 = (Pt0[0] + Pt0[1] +Pt0[2]) / 3.0;

    MW_He  = 4.0026;
    MW_air = 28.97;

    MW = X * MW_He + (1.0 − X) * MW_air;

    C = X * MW_He  / MW;

    /***************************/


    reduce_data(Pt2, Pc, Tt, X, solution, CM, Cg, CPP);

    M1 = solution[0];
    Pt1 = solution[1];
    P1 = solution[2];
    T1 = solution[3];
    U1 = solution[4];
```

```c
        rho1  = solution[5];
        a1  = solution[6];
        gamma1  = solution[7];

        nondimension(solution, M0, Pt0, Tt0);

        Pt1Pt0   = solution[1];
        P1P0     = solution[2];
        T1T0     = solution[3];
        U1U0     = solution[4];
        rho1rho0 = solution[5];
        a1a0     = solution[6];
        gamma1   = solution[7];
        Tt1Tt0   = Tt / Tt0[1];
        PtjPt0   = AvgPtj / AvgPt0;
        zD       = z / D;
        yD       = y / D;

        fprintf (outfp1,"%6.3f%6.3f", zD, yD);
        fprintf (outfp1,"%6.3f%6.3f%6.3f%6.3f%7.4f\n",
            Pt1Pt0, U1U0, rho1rho0, PtjPt0, C);

        printf ("\n%6.3f%6.3f", zD, yD);
        printf ("%6.3f%6.3f%6.3f%6.3f%6.3f%6.3f",
            M1, Pt1Pt0, P1P0, T1T0, U1U0,rho1rho0);
        printf ("%6.3f%6.3f%6.3f%6.3f%7.4f",
            a1a0, gamma1, Tt1Tt0, PtjPt0, C);

        fprintf (outfp2,"%6.3f%6.3f", zD, yD);
        fprintf (outfp2,"%6.3f%6.3f%6.3f%6.3f%6.3f%6.3f",
            M1, Pt1Pt0, P1P0, T1T0, U1U0, rho1rho0);
        fprintf (outfp2,"%6.3f%6.3f%6.3f%6.3f%7.4f\n",
            a1a0, gamma1, Tt1Tt0, PtjPt0, C);
    }

    printf("\n\n");

    fclose(infp);
    fclose(outfp1);
    fclose(outfp2);
}


/**********************************
SUBROUTINE TO READ IN CONE-FLOW DATA
**********************************/

void coneflow_data (float CM[], float Cg[], float CPP[])
{
    FILE *fp;
    int i=0;
    char inbuff[80];
```

```
    if ((fp = fopen("coneflow.dat", "r")) == NULL) {
        printf ("\nFile, coneflow.dat, not found!\n");
        exit (1);
    }

    fgets(inbuff, 80, fp);

    while (fgets(inbuff, 80, fp) != NULL) {
        sscanf(inbuff, "%f %f %f%*c",
            &CM[i], &Cg[i], &CPP[i]);
        i++;
    }

}

/*****************************************
FUNCTION TO COMPUTE SPECIFIC GAS CONSTANT
*****************************************/

float gas_constant(float X)
{
    float MW;

    MW = X * 4.0026 + (1.0 - X) * 28.97;

    return (8314.0 / MW);
}

/*****************************************
FUNCTION TO COMPUTE RATIO OF SPECIFIC HEATS
*****************************************/

float heat_ratio(float X, float R, float T)
{
    float gamma, Cp, Cp_air, Cp_He, MW, MW_air,
        MW_He, f1, f2, f3, f4;

    MW_air  = 28.97;
    MW_He   = 4.0026;
    Cp_He   = 5192.6;

    f1      =  0.2811E+02;
    f2      =  0.1967E-02 * T;
    f3      =  0.4802E-05 * T * T;
    f4      = -0.1966E-09 * T * T * T;
    Cp_air  = (f1 + f2 + f3 + f4) * 1000.0 / MW_air;

    MW = X * MW_He + (1.0 - X) * MW_air;

    Cp = (MW_He * X * Cp_He + MW_air *
```

```
            (1.0 − X) * Cp_air) / MW;

    gamma = Cp / (Cp − R);

    return (gamma);
}


/ *****************************************************
FUNCTION TO COMPUTE THE TOTAL−TO−STATIC PRESSURE RATIO
*****************************************************/

float pressure_ratio (float M, float gamma)
{
    float f1, f2, PtP;

    f1 = 1.0 + (gamma − 1.0) * M * M / 2.0;
    f2 = gamma / (gamma − 1.0);
    PtP = pow (f1, f2);

    return (PtP);
}


/ *******************************************************
FUNCTION TO COMPUTE THE TOTAL−TO−STATIC TEMPERATURE RATIO
*******************************************************/

float temp_ratio (float M, float gamma)
{
    float TtT;

    TtT = 1.0 + (gamma −1.0) * M * M / 2.0;

    return (TtT);
}


/ ***********************
SUBROUTINE TO BRACKET "M1"
***********************/

void bracket(float MACH[], float GAMMA[], float PP[], float PcPt2,
    float gamma, float CM[], float Cg[], float CPP[])
{

    int     i = 0, hiflag = 0;
    int     lowflag01, lowflag23, hiflag01, hiflag23;

    while (hiflag == 0) {
        if (Cg[i] <= gamma) {
            GAMMA[0]  = Cg[i];
            GAMMA[1]  = Cg[i];
        }
```

```
        if ((hiflag == 0) && (Cg[i] >= gamma)) {
            GAMMA[2]  = Cg[i];
            GAMMA[3]  = Cg[i];
            hiflag  = 1;
        }
        i++;
    }

    i = 0;

    lowflag01 = 0;
    lowflag23 = 0;
    hiflag01  = 0;
    hiflag23  = 0;

    while ((hiflag01 == 0) || (hiflag23 == 0)) {
        if (Cg[i] == GAMMA[0]) {
            if ((lowflag01 == 0) && (CPP[i] >= PcPt2)) {
                PP[0]   = CPP[i];
                MACH[0] = CM[i];
            }
            if ((hiflag01 == 0) && (CPP[i] <= PcPt2)) {
                PP[1]   = CPP[i];
                MACH[1] = CM[i];
                hiflag01  = 1;
                lowflag01 = 1;
            }
        }

        if (Cg[i] == GAMMA[2]) {
            if ((lowflag23 == 0) && (CPP[i] >= PcPt2)) {
                PP[2]   = CPP[i];
                MACH[2] = CM[i];
            }
            if ((hiflag23 == 0) && (CPP[i] <= PcPt2)) {
                PP[3]   = CPP[i];
                MACH[3] = CM[i];
                hiflag23  = 1;
                lowflag23 = 1;
            }
        }
        i++;
    }
}

/**********************************
FUNCTION TO INTERPOLATE MACH NUMBER
**********************************/

float interpolate(float MACH[], float GAMMA[], float PP[],
    float PcPt2, float gamma)
```

```
{
    int    i, j, k, p ,n;
    float m, temp, a[5][6], y[5], M1;

    n = 4;

    for (i = 1; i <= 4; i++) {
        a[i][1] = PP[i-1];
        a[i][2] = GAMMA[i-1];
        a[i][3] = PP[i-1] * GAMMA[i-1];
        a[i][4] = 1.0;
        a[i][5] = MACH[i-1];
    }
    for (i = 1; i <= (n-1); i++) {
        p = i;
        while (a[p][i] == 0)
            p++;
        if (p > n) {
            /* POINT IS BELOW CALIBRATION CURVES */
        }
        if (p != i) {
            for (k = 1; k <= (n+1); k++) {
                temp = a[p][k];
                a[p][k] = a[i][k];
                a[i][k] = temp;
            }
        }
        for (j = (i+1); j <= n; j++) {
            m = a[j][i] / a[i][i];
            for (k = 1; k <= (n+1); k++)
                a[j][k] = a[j][k] - m * a[i][k];
        }
    }
    if (a[n][n] == 0) {
        printf ("\nNo unique solution exists");
        exit (1);
    }
    if (p > n)
        M1 = 1.0;
    else {
        y[n] = a[n][n+1] / a[n][n];
        temp = 0.0;
        i = n-1;
        do {
            for (j = (i+1); j <=n; j++)
                temp = temp + a[i][j] * y[j];
            y[i] = (a[i][n+1] - temp) / a[i][i];
            i = i-1;
            temp = 0.0;
        }
        while (i > 0);
```

```
        M1 = y[1] * PcPt2 + y[2] * gamma + y[3] * PcPt2
             * gamma + y[4];
    }
    return (M1);
}

/***************************************************
FUNCTION TO COMPUTE STATIC-TO-PITOT PRESSURE RATIO
***************************************************/

float Rayleigh (float M1, float gamma)
{
    float f1, f2, f3, f4, f5, f6, f7, f8, f9, P1Pt2;

    f1 = gamma - 1.0;
    f2 = gamma + 1.0;
    f3 = 1.0 / (gamma - 1.0);
    f4 = gamma / (gamma - 1.0);
    f5 = 2.0 * gamma;
    f6 = (f5 / f2) * M1 * M1 - (f1 / f2);
    f7 = 0.5 * f2 * M1 * M1;
    f8 = pow(f6, f3);
    f9 = pow(f7, f4);
    P1Pt2 = f8 / f9;

    return (P1Pt2);

}

/*****************************
FUNCTION TO COMPUTE MACH NUMBER
*****************************/

float mach_number (float PcPt2, float gamma, float CM[],
    float Cg[], float CPP[])
{
    float MACH[4], GAMMA[4], PP[4], M1;
    int i;

    bracket(MACH, GAMMA, PP, PcPt2, gamma, CM, Cg, CPP);

    M1 = interpolate(MACH, GAMMA, PP, PcPt2, gamma);

    return (M1);
}

/***************************************************
ALTERNATE MACH NUMBER ROUTINE FOR SUB-CRITICAL POINTS
***************************************************/
```

```c
float alt_mach_number ()
{

    return(1.0);
}


/****************************************
FUNCTION TO VERIFY CONE SHOCK ATTACHMENT
****************************************/

int verify_shock(float PcPt2, float gamma,
    float Cg[], float CPP[])
{

    float GAMMALO, GAMMAHI, PPLO, PPHI, PPcrit;
    int i=0, hiflag = 0, flag;

    while (hiflag == 0) {
        if (Cg[i] <= gamma) {
            GAMMALO  = Cg[i];
            PPLO     = CPP[i];
        }
        if ((hiflag == 0) && (Cg[i] >= gamma)) {
            GAMMAHI  = Cg[i];
            PPHI     = CPP[i];
            hiflag   = 1;
        }
        i++;
    }

    PPcrit = ((PPHI - PPLO) / (GAMMAHI - GAMMALO))
        * (gamma - GAMMALO) + PPLO;

    if (PcPt2 > PPcrit)
        flag = 1;
    else
        flag = 0;

    return (flag);
}

/*******************************************************
SUBROUTINE TO HANDLE ITERATIVE DATA REDUCTION PROCEDURE
*******************************************************/

void reduce_data (float Pt2, float Pc, float Tt, float X,
    float solution[], float CM[], float Cg[], float CPP[])
{
    float a, b, tol, limit, diff;
    float gamma, T, TtT, R, PcPt2, M1;
    float P1Pt2, T1, P1, U1, rho1, c1;
```

```
float Pt1P1, Pt1, Plast;
int flag;

PcPt2 = Pc / Pt2;

tol = 1.0;

a = 50.0;
b = 1000.0;

R = gas_constant (X);
gamma = heat_ratio (X, R, a);

flag = verify_shock(PcPt2, gamma, Cg, CPP);

if (flag == 0)
    M1 = mach_number (PcPt2, gamma, CM, Cg, CPP);
else if (flag == 1)
    M1 = alt_mach_number();

TtT = temp_ratio(M1, gamma);
limit = TtT * a;

do {
    T = a + (b - a) / 2.0;
    gamma = heat_ratio (X, R, T);

    flag = verify_shock(PcPt2, gamma, Cg, CPP);

    if (flag == 0)
        M1 = mach_number (PcPt2, gamma, CM, Cg, CPP);
    else if (flag == 1)
        M1 = alt_mach_number();

    TtT = temp_ratio(M1, gamma);
    diff = TtT * T - Tt;
    if ((diff*limit) < 0)
        a = T;
    else
        b = T;
}
while (fabs(diff) > tol);

T1 = T;

c1 = sqrt(gamma * R * T1);

U1 = M1 * sqrt(gamma * R * T1);

Pt1P1 = pressure_ratio(M1, gamma);
```

```
        P1Pt2  =  Rayleigh(M1, gamma);

        P1  =  P1Pt2 * Pt2;

        Pt1  =  Pt1P1 * P1;

        rho1  =  P1 / (0.00014504 * R * T1);

        solution[0]  =  M1;
        solution[1]  =  Pt1;
        solution[2]  =  P1;
        solution[3]  =  T1;
        solution[4]  =  U1;
        solution[5]  =  rho1;
        solution[6]  =  c1;
        solution[7]  =  gamma;

}

/*******************************************
SUBROUITNE  TO  NONDIMENSIONALIZE  REDUCED  DATA
*******************************************/

void nondimension (float solution[], float M0,
    float Pt0[], float Tt0[])
{
    float M1, Pt1, P1, T1, U1, rho1, c1;
    float P0, T0, U0, rho0, c0, gamma0, R0;
    float Pt0P0, Tt0T0, X;
    float a, b, tol, limit, diff;

    M0  =  1.96;
    X   =  0.0;
    R0  =  gas_constant(X);

    a  =  50.0;
    b  =  1000.0;
    tol  =  1.0;

    gamma0  =  heat_ratio(X, R0, a);
    Tt0T0  =  temp_ratio(M0, gamma0);
    limit  =   Tt0T0 * a;

    do {
        T0  =  a + (b − a) / 2.0;
        gamma0  =  heat_ratio(X, R0, T0);
        Tt0T0  =  temp_ratio(M0, gamma0);
        diff  =  Tt0T0 * T0 − Tt0[2];
        if ((diff*limit) < 0)
            a  =  T0;
        else
```

```
            b  =  T0;
      }
      while (fabs(diff) > tol);

      Pt0P0  =  pressure_ratio(M0, gamma0);
      P0  =  Pt0[1] / Pt0P0;
      rho0  =  P0 / (0.00014504 * R0 * T0);
      c0  =  sqrt(gamma0 * R0 * T0);
      U0  =  M0 * c0;

      solution[1]  =  solution[1]  /  Pt0[0];
      solution[2]  =  solution[2]  /  P0;
      solution[3]  =  solution[3]  /  T0;
      solution[4]  =  solution[4]  /  U0;
      solution[5]  =  solution[5]  /  rho0;
      solution[6]  =  solution[6]  /  c0;
}
```

Raymond Preston Fuller, Jr. was born October 16, 1969, son of Raymond Preston Fuller, Sr. and Mary Louise Fuller. He attended Hazel Park High School in the Detroit Metropolitan Area and graduated in 1987. Raymond went on to attend the University of Michigan, Ann Arbor and received his Bachelors of Science degree in Aerospace Engineering in 1992. Raymond then began his graduate education at Virginia Polytechnic Institute and State University studying Aerospace Engineering and conducting research under the direction of Dr. Joseph Schetz. Raymond received his Master of Science degree in Aerospace Engineering in 1994. In cooperation with Virginia Tech, Raymond continued conducting research at Wright-Patterson Air Force Base while employed by Taitech, Inc. Upon completion of this dissertation in August, 1996, Raymond received his Doctor of Philosophy degree in Aerospace Engineering, thus completing his formal education.